

**UCLA**

**UCLA Electronic Theses and Dissertations**

**Title**

High Throughput Passive Inertial Separation of Viscoelastic Droplets in Microchannels

**Permalink**

<https://escholarship.org/uc/item/0b39v9rs>

**Author**

Karimi, Armin

**Publication Date**

2018

Peer reviewed|Thesis/dissertation

UNIVERSITY OF CALIFORNIA

Los Angeles

High Throughput Passive Inertial Separation of  
Viscoelastic Droplets in Microchannels

A dissertation submitted in partial satisfaction of the  
requirements for the degree Doctor of Philosophy  
in Mechanical Engineering

by

Armin Karimi

2018

© Copyright by

Armin Karimi

2018

## ABSTRACT OF THE DISSERTATION

### High Throughput Passive Inertial Separation of Viscoelastic Droplets in Microchannels

by

Armin Karimi

Doctor of Philosophy in Mechanical Engineering

University of California, Los Angeles, 2018

Professor Dino Di Carlo, Co-Chair

Professor Pei-Yu Chiou, Co-Chair

Droplet microfluidics offers a unique liquid-handling capability for various applications, such as single cell analysis and sorting, chemical synthesis and development of biochemical assays, diagnostics, drug screening, DNA sequencing and directed evolution. Producing highly monodisperse pico-liter to nano-liter droplets enables quantitative control of solute concentration, while compartmentalizing samples into droplets provides a precise chemical and bio-chemical environment. Small volume and high concentration of encapsulated samples allows for rapid processing and analysis of the thousands to millions of cells that must be screened to find a heterogenous population of interest. Being able to effectively sort droplets is in high demand.

A limiting factor for active sorting of droplets is the real time sensing and control mechanism that they require. The control components of active systems lead to a complex and expensive sorting device. On the other hand, passive methods of droplet sorting which operate

based on intrinsic properties of droplets, are especially important to reduce the complexity and cost. Many biological reactions that occur inside droplets can alter droplet properties, such as viscosity, interfacial tension and viscoelasticity. In this study we focus on non-Newtonian fluids which exhibit viscoelastic properties. A need to passively sort droplets based on intrinsic properties, in an inertial flow regime, is of an immense importance.

Viscoelastic solutions possess unique properties such as shear rate dependence viscosity, and relaxation time. We developed an integrated microfluidics platform to generate, incubate, and sort droplet based on viscoelastic properties on-chip.

One approach to achieve this is by tuning the timescale of flow compare to relaxation time of viscoelastic droplets, where we engineered our platform to pre-deformed droplet, and the droplet retains its deformed shape within the relaxation time. This results in a significant enhancement in viscoelastic-based droplet sorting.

The dissertation of Armin Karimi is approved.

Jeffrey D. Eldredge

Chang-Jin Kim

Pei-Yu Chiou, Committee Co-Chair

Dino Di Carlo, Committee Co-Chair

University of California, Los Angeles

2018

## DEDICATION

I would like to dedicate this work to my loving mother, who has been my motivation, strength, my best friend, and most importantly, my mentor in life. I would also like to thank my family members for their unconditional love and support, my great advisor, my labmates, and kind friends, who without their help, I would not have had my wish come true!

## TABLE OF CONTENTS

<b>Chapter 1: Droplet Sorting</b> .....	<b>1</b>
1. Introduction.....	1
2. Droplet sorting techniques .....	2
2.1. Passive droplet sorting .....	3
3. Lateral migration of particles and droplets in microchannels .....	3
3.1. Solid Particles .....	3
3.1.1. Inertial lift force .....	3
3.2. Elastic particles.....	5
3.3. Liquid Droplets.....	5
3.3.1. Deformability-induced lift force.....	6
3.3.2. Inertial lift force .....	6
3.3.3. Other lift forces .....	7
4.1. Scaling analysis.....	7
4.4.1. Reynolds number .....	9
4.4.2. Capillary number .....	10
4.4.3. Weber number .....	11
4.4.4. Weissenberg number:.....	11
4.4.5. Viscosity ratio.....	12
4.4.6. Flow rate ratio .....	12
4.4.7. Channel aspect ratio.....	12
4.4.8. Droplet aspect ratio.....	12
5. Conclusions.....	12
6. References .....	13
<b>Chapter 2: Rheology</b> .....	<b>15</b>
1. Material .....	15
2. Methods: .....	16
3. Results & Discussion:.....	17
4. Summary: .....	25
5. References:.....	26
<b>Chapter 3: Microfluidics platform</b> .....	<b>28</b>



1. Device fabrication.....	28
2. Device design .....	28
2.1. Integrated device .....	30
2.2. Incubation device .....	33
3. Device iterations .....	34
4. References:.....	36
<b>Chapter 4 - Droplet generation .....</b>	<b>37</b>
1. Introduction.....	37
2. Droplet generation methods .....	37
2.1. Flow Focusing Device.....	39
3. Scaling Analysis (droplet generation).....	41
4. Droplet break-up.....	42
5. Flow map .....	44
6. Droplet Size.....	45
6.1. Capillary number .....	46
7. Conclusions.....	48
8. References .....	49
<b>Chapter 5 – Migration rate of droplets in microchannels.....</b>	<b>51</b>
1. Introduction:.....	51
1.1. Systematic study procedure: .....	52
2. Material .....	53
2.1. Effect of interfacial tension variation.....	53
2.2. Effect of density variation .....	54
3. Experimental set up .....	55
3.1. System performance:.....	57
3.2. Starting position .....	58
3.3. Flow rate ratio .....	59
3.4. Flow simulation .....	59
4. Migration rate .....	60
4.1. Slip velocity .....	62
4.2. Effect of droplet size .....	62
4.3. Effect of viscosity ratio.....	63
5. Scaling analysis .....	63

5.1. Deformability-induced lift force.....	63
5.2. Inertial effect on migration.....	68
6. Conclusions.....	70
7. References.....	70
1. Viscoelasticity-based separation.....	72
2. Material .....	73
$\eta_{\infty}$ (Pa s).....	74
3. Viscoelastic scaling.....	75
3.1. Weissenberg number.....	75
3.2. Deborah number.....	75
4. Viscoelasticity .....	76
4.1. Shear rate dependence of viscosity .....	76
5. Results:.....	82
5.1. Experiment condition .....	82
6. Discussion .....	83
7. References.....	88
<b>Chapter 7 – Enhanced Separation based on Viscoelasticity in Confined Geometries.....</b>	<b>90</b>
1. Introduction.....	90
2. Theoretical background.....	92
3. Droplet deformability .....	97
4. Migration mechanism in low aspect ratio channel ( $\phi = 0.1$ ).....	99
4.1. Flow time scale - short.....	100
4.2. Flow time scale – long.....	108
4.2.1. Study the effect of flow rate ratio .....	108
4.2.1.1. Droplet shape.....	108
4.2.1.2. Droplet migration .....	113
5. Conclusions.....	118
6. Applications.....	119
7. References.....	125

## LIST OF FIGURES

Fig. 1: High throughput screening of a broad range of samples using droplet microfluidics [8] ....	1
Fig. 2: Active and passive droplet sorting techniques [9]–[12].....	2
Fig. 3: two opposing lift forces action on particles in rectangular cross-section channels [17].....	4
Fig. 4: deformable particles .....	4
Fig. 5: Forces on droplets- $F_d$ : Drag forces, $F_b$ : Buoyancy, $F_{wr}$ : Wall repulsion, $F_{v^+}$ : Positive viscoelastic force, $F_{v^-}$ : Negative viscoelastic force, $F_i$ : Inertial forces (same direction as $F_{v^-}$ ), $F_D$ : Dean Forces (in case of curved channel) [13].....	7
Fig. 6: independent parameters for scaling analysis .....	9
Fig. 7: Viscosity measurements for Newtonian solutions.....	18
Fig. 8: Viscosity measurement compared with empirical correlations .....	19
Fig. 9: Power law calculation for all solutions .....	20
Fig. 10: Interfacial tension calculations [9] .....	23
Fig. 11: Power Law analysis for viscosities of solutions.....	26
Fig. 12: schematic of an integrated device with a 2-inlet droplet generation device .....	29
Fig. 13: Schematic of alternative device for applications requiring incubation with a 3-inlet droplet generation device.....	30
Fig. 14: various combination of integrated device.....	32
Fig. 15: schematic of a simple 2-inlet droplet generator device, A) Integrated device B) Incubation device .....	33
Fig. 16: Various attempts for design improvements .....	35
Fig. 17: Reservoir design iterations.....	36
Fig. 18: Schematic of passive and active droplet generation [2] .....	38
Fig. 19: Typical microfluidic droplet generation devices [2] .....	39
Fig. 20: schematic of planar flow focusing device [3].....	40
Fig. 21: example of a flow map for different droplet generation modes [3] .....	45
Fig. 22: droplet size as a function of flow rates for different aqueous phase fluids .....	46
Fig. 23: Critical Capillary number as a function of droplet diameter.....	47
Fig. 24: Capillary number changing with $Q_c$ .....	47
Fig. 25: Property changes of droplets in during common biological processes .....	51
Fig. 26: Systematic study.....	53
Fig. 27: Comparison of interfacial tension and density changes with viscosity ratio variations .....	55
Fig. 28: schematic of our integrated platform .....	56
Fig. 29: schematic of an integrated device for sorting – and trajectory and equilibrium position of droplets .....	57
Fig. 30: COMSOL simulation of flow in different sections of the channel – Sec I: developing flow and droplets are located close to the wall, Sec II: Fully developed flow and lateral migration of droplets, Sec III: Sudden decrease in velocity in the expansion region where droplets separation occurs.....	60
Fig. 31: Migration rate for the entire main channel. Each color represents one section, e.g., Section A is the beginning of the main channel and Section E is the last section of the channel before the expansion region .....	61

Fig. 32: Slip velocity of droplets .....	62
Fig. 33: viscosity ratio dependence of Alpha [Hatch et al. 2013] .....	64
Fig. 34: contribution of inertia on migration rate .....	68
Fig. 35: $C_0$ dependence on viscosity ratio .....	69
Fig. 36: Shear-rate dependence of viscosity of PEO (non-Newtonian) solutions compared with the selected Newtonian solutions of glycerol/ water mixtures from Table 8 .....	74
Fig. 37: shear rate along channel .....	78
Fig. 38: Localized shear rate of droplets – a) first 500 $\mu\text{m}$ region, b) 50 $\mu\text{m}$ upstream of the expansion region and the expansion region .....	79
Fig. 39: Viscosity chart for PEO and GW solutions in the main channel (green) and the expansion region (blue) – shear thinning behavior of PEO solutions. The legends indicating different solutions. ....	80
Fig. 40: Localized viscosity for the first 500 $\mu\text{m}$ region, and 50 $\mu\text{m}$ upstream of the expansion region and the expansion region, a,b) Newtonian Droplets, c,d) non-Newtonian droplets .....	81
Fig. 41: Device schematic identifying the AOI in this section .....	83
Fig. 42: A) Trajectories of Newtonian droplets in the expansion region ( $\zeta = 0.51 - 0.58$ , $\phi = 0.3$ ), B) Axial and Transverse velocity along the expansion region, C) Trajectories of Newtonian & non-Newtonian droplets in the expansion region ( $\zeta = 0.58$ , $\phi = 0.3$ ) .....	84
Fig. 43: COMSOL simulation of flow field and fluid streamlines in the expansion region with more outlets.....	85
Fig. 44: competition between viscosity and viscoelasticity .....	87
Fig. 45: Schematic of our separation platform - distinct trajectories between viscous and viscoelastic droplets.....	91
Fig. 46: Applied force on viscoelastic material .....	93
Fig. 47: Time lapse of deformation and recovery of viscoelastic droplets.....	95
Fig. 48: A) Irregular shapes of viscoelastic droplets after deformation and B) stiff glycerol droplets .....	96
Fig. 49: deformation of droplet in high aspect ratio ( $\Phi = 0.3$ ) channel, A) viscous, and B) viscoelastic droplets.....	96
Fig. 50: Device schematic, A) close-up of the constriction B) size-dependence of droplet deformability .....	98
Fig. 51: migration of droplets in the separation channel, A) axial velocity of PEO and glycerol droplets, B) time lapse of high speed video of droplet migration C) droplet's distance from the wall for the entire length of the channel – the Initial migration region is highlighted.....	101
Fig. 52: A) trajectories for glycerol droplets vs. PEO in the expansion region, B) enhancement of lateral migration separation in the expansion region .....	102
Fig. 53: circularity of PEO and glycerol droplets as a function of time.....	103
Fig. 54: circularity and orientation of PEO and glycerol droplets at the same position along the channel, A) circularity, B) orientation with respect to the flow direction – the numbers in red corresponding to the actual droplet shape in Fig. 55. ....	104
Fig. 55: time elapse of rotation of viscoelastic droplets in the main channel - the numbers in red corresponding to the calculated circularity and orientation of droplet shape in Fig. 54. ....	104
Fig. 56: minimal sheath flow impact on deformation of PEO droplets due to a very short time scale of sheath flow .....	107
Fig. 57: high efficiency separation of viscoelastic droplets.....	108

Fig. 58: size dependence circularity of PEO, $Q_s = 0.5$ , $Q_{sh} = 65 \mu\text{L}/\text{min}$ , filled symbols represent where the droplet makes contact with the pillar, solid line represent where the droplet enters the main channel.....	110
Fig. 59: change in droplet orientation due to the deformation from pillar and the sheath flow ..	111
Fig. 60: circularity of PEO, with increasing sheath flow from $Q_{sh} = 45 - 65 \mu\text{L}/\text{min}$ , filled symbols represent where the droplet makes contact with the pillar, solid lines represent where the droplet enters the main channel.....	113
Fig. 61: flow rate dependent position-map of droplet sizes ranging from 150-180 $\mu\text{m}$ , A) increasing sheath flow ( $Q_s = 0.5 \mu\text{L}/\text{min}$ ), B) increasing sheath flow ( $Q_s = 2 \mu\text{L}/\text{min}$ ), C) increasing spacer flow ( $Q_{sh} = 55 \mu\text{L}/\text{min}$ ), D) PEO, increasing sheath flow ( $Q_s = 0.5 \mu\text{L}/\text{min}$ ) - highlighted area represents the initial migration region.....	114
Fig. 62: trajectory of glycerol (viscous) droplets, A) flow rate dependent position-map, B) trajectory in the expansion region.....	115
Fig. 63: distinguishable separation between viscous and viscoelastic droplets in “final separation” region .....	117
Fig. 64: the presence of pillar enhances initial droplet migration .....	118
Fig. 65: schematic of droplet migration for different timescales relative to relaxation time, A) shorter flow time scale, B) longer flow timescale .....	119
Fig. 66: Trajectories for lower limit droplet (PBS and RIPA) vs. PEO, A) main channel, B) expansion region .....	121
Fig. 67: Deformation of PBS and RIPA droplets .....	122
Fig. 68: Single cell encapsulation and lysis in droplets .....	123
Fig. 69: Shear thinning behavior of cell lysate solution .....	124
Fig. 70: Shear thinning behavior of amplified DNA solution .....	125

## LIST OF TABLES

Table 1: important parameters in identifying lift forces.....	8
Table 2: Viscous solutions .....	17
Table 3: Power law calculation for various Newtonian and non-Newtonian solutions .....	21
Table 4: Cross model calculations.....	22
Table 5: Validation of interfacial tension measurements .....	25
Table 6: droplet properties .....	52
Table 7: Dynamic viscosities, density and viscosity ration of the materials considered in the present study.....	54
Table 8: Newtonian Liquids .....	73
Table 9: Non-Newtonian Liquids.....	73
Table 10: Relaxation Time - Cross Model Validation .....	74
Table 11: Properties of PEO solutions.....	75
Table 12: Percentage viscosity variation for different solution undergoing varying shear rate....	81
Table 13: experimental condition.....	82
Table 14: flow time scale and Deborah number for different viscoelastic droplets – Qsh = 65 $\mu\text{L}/\text{min}$ .....	112
Table 15: deformability characterization .....	122

## ACKNOWLEDGEMENTS

I would like to express my most appreciation toward my advisor, Dr. Dino Di Carlo, for giving the opportunity to do research in his lab. His continuous support and guidance has been my encouragement for the past few years. Many thanks to my labmates for their helpful discussions and support. Thanks to Quique and Dunni!

I also would like to recognize the immense help from the undergraduate students who helped me with analyzing data and performing experiments in this work, and helped me grow as a mentor:

Thanks to Austin Lee (rheology measurements), Michael Bogumil (data analysis and programming), Negin Djajali (data analysis and cell culture), Rishav Roy and Samuel Bray.

Also, thanks to my friends Kaveh and Pamchal for our regular coffee breaks!

## VITA

### EDUCATION

- M.S. in Mechanical Engineering (2013), University of California, Los Angeles
- M.S. in Mechanical and Aerospace Engineering (2010), University of California, Irvine
- B.S. in Mechanical Engineering (2004), IAUSRB, Tehran, Iran

### RESEARCH APPOINTMENTS

- Graduate student researcher (2013-2018), University of California, Los Angeles  
Professor Dino Di Carlo
- Graduate student researcher (2011-2013), University of California, Los Angeles  
Professor Ivan Catton
- Graduate student researcher (2008-2010), University of California, Irvine  
Professor Derek Dunn-Rankin

### WORK EXPERIENCE

- Teaching Assistant, University of California, Los Angeles (2011-2018)  
BE167L: Bioengineering Laboratory
  - Cell culture, fluorescence microscopy and bioconjugationBE 177A: Bioengineering Capstone Design
  - Mentored Bioengineering senior students to design and prototype biomedical devices for diagnostics, screening and treatmentLS 30A: Mathematics for Life Scientists
  - Taught Python programming to Life Science students for modeling of biological systemsBE 155/255: Fluid-Particle and Fluid-Structure interactions in Microflows  
MAE 105D: Transport Phenomena  
MAE 157: Basic Mechanical Engineering Laboratory  
MAE 105A: Fundamentals of Engineering Thermodynamics (Instructor)
- Design Engineer/ Project Manager (2005-2010), GLP Engineering, Inc., Santa Ana, CA



## PUBLICATIONS

- (In Progress) Armin Karimi, Austin Lee, Michael Bogumil, and Dino Di Carlo, “*High Throughput Inertial Separation of Droplets Towards Single Cell Nucleic Acid Analysis*”
- Manjima Dhar, Jessica Wong, Armin Karimi, and Dino Di Carlo, “*High efficiency vortex trapping of circulating tumor cells*” – Journal of Biomicrofluidic 2015.
- Armin Karimi, Sean Reilly, and Ivan Catton, “*Enhanced Performance of a Thermal Ground Plane Utilizing an Inorganic Aqueous Solution*” – IThERM/ IEEE 2014.
- “*Thermal Deformation Analysis of Modular Mirrors – Karimi, 2010, University of California, Irvine.*” - M.Sc. thesis

## PRESENTATIONS

- Armin Karimi, Austin Lee, Michael Bogumil, and Dino Di Carlo, “*High Throughput Inertial Separation of Droplets Towards Single Cell Nucleic Acid Analysis*” – CYTO, 2018
- Armin Karimi, Austin Lee, and Dino Di Carlo, “*Passive Separation of Droplets in Microfluidic Platforms*” – Micro and Nanotechnology in Medicine, IEEE/ EMBS, 2016
- Armin Karimi, Rishav Roy, Samuel Bray, and Dino Di Carlo, “*Controlling Lateral Inertial Migration Rate of Particles in Microchannels*” – APS/ DFD, 2015
- Armin Karimi, Sean Reilly, and Ivan Catton, “*Enhanced Performance of a Thermal Ground Plane Utilizing an Inorganic Aqueous Solution*” – IThERM/ IEEE, 2014

## HONORS AND AWARDS

- Recipient of a travel award for CYTO 2018 conference, Prague, Czech Republic
- Recipient of a travel award for IEEE-IThERM 2014 conference, Orlando, FL
- Awarded the 2<sup>nd</sup> place for design and development of a real time visual feedback system that can be integrated on neonatal infusion pumps for a precise control of the amount of the administered drugs to infants; our team managed to design, prototype and present the proposed platform during a 24-hr competition - *Business of Science Center at UCLA* – Oct. 2013

# Chapter 1: Droplet Sorting

## 1. Introduction

Droplet microfluidics offers a unique liquid-handling capability for cell-based assays and screening. Compartmentalization of samples into small volume droplets not only reduces the cost associated with the use of reagents[1][2], but also allows for rapid analysis of a broad range of samples (Fig. 1)[3]. The ability to produce highly monodisperse pico-liter to nano-liter droplets has made droplet microfluidics a versatile tool for various applications, such as single cell analysis and sorting, chemical synthesis and biochemical assay development, diagnostics, drug screening, DNA sequencing and directed evolution. The small volume of sample used in each droplet is thousands to millions times less than in a microliter well plate, and each droplet can function as a precise chemical and bio-chemical reactor that can be independently controlled. Compartmentalization of single cells in droplets enables further genomic analysis or analysis of the proteins secreted from or by cells in each individual droplet [4] [5] [6]. In addition, fast reactions occur in droplets, owing to the small volume (and therefore high concentration) in each drop, which enables quick detection of individual cells of interest from large population of cells [7][8].

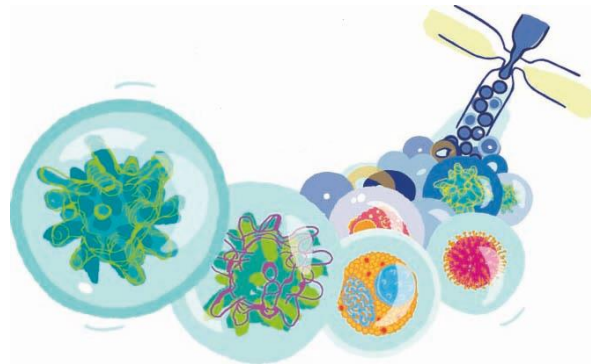


*Fig. 1: High throughput screening of a broad range of samples using droplet microfluidics [8]*

## 2. Droplet sorting techniques

Quantitative analysis of droplets containing samples with different contents is enabled by high throughput sorting of droplets. Several microfluidic techniques have been developed to sort droplets, both passive (depending on intrinsic properties) and active (depending on sensing of an internal signal within a droplet) have been demonstrated.

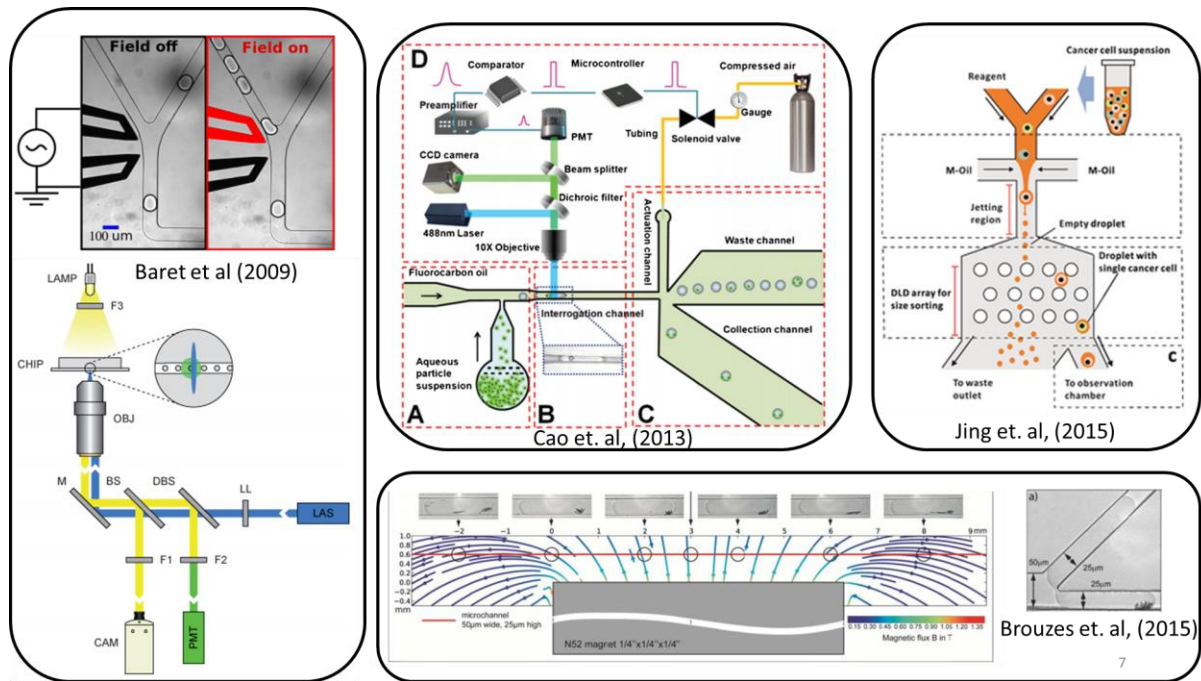


Fig. 2: Active and passive droplet sorting techniques [9]–[12]

A limiting factor for active sorting of droplets is the real time sensing and control mechanism that they require [13][14]. The active control components of active systems could make the fabrication of the sorting device complex and expensive, which could largely impact the energy demand and use of the system [15]. In addition, it could impose limitations on the parallelization of the system. A system that could potentially reduce the expensive active control components, provide a less complex fabrication and operation, and enable device parallelization is needed in this field. It is referred to as the passive droplet sorting and we will be focusing on the passive sorting in the work presented in this study.

## 2.1. Passive droplet sorting

Passive sorting of droplets in microfluidic systems can provide unique advantages, including lower cost instruments and increased parallelization, however, the physical properties and hydrodynamic forces determining droplet motion in microchannel systems should be connected to the reactions of interest in droplets to sort based on useful properties[16][13][17][18]. The passive sorting is mainly based on hydrodynamic forces applied on droplets, and depending on the droplet properties and its surrounding, the magnitude of the forces determine the motion of droplets in microfluidics channels. In order to achieve spatial control of droplets, an understanding of the droplet motion and lateral migration mechanism of droplets is required.

A straight channel with a rectangular cross-section is one of the most common geometries that can be used to sort particles and droplets. There are different forms of non-linearity that can be introduced to this system that can generate lift forces (defined as forces that are directed perpendicular to the direction of the flow) to manipulate the lateral migration of particles and droplets. In the following section we give an overview of the lateral migration mechanism of particles and droplets in microfluidics channels and later we discuss the magnitude and the relative importance of various forces that contribute to the dynamics and the migration of droplets.

## 3. Lateral migration of particles and droplets in microchannels

### 3.1. Solid Particles

#### 3.1.1. Inertial lift force

It was first observed by Segre and Silberberg [19] that a randomly distributed particles were focused on an annulus with a distance of around 0.6 times the radius from a center of a

cylindrical pipe (one cm in diameter). This behavior suggested that there must be at least two main opposing lift forces acting on these particles: one pushes particles away from walls (wall-induced lift force), and the other moves particles toward regions with larger shear rates (shear gradient-induced lift force) [17](Fig. 3).

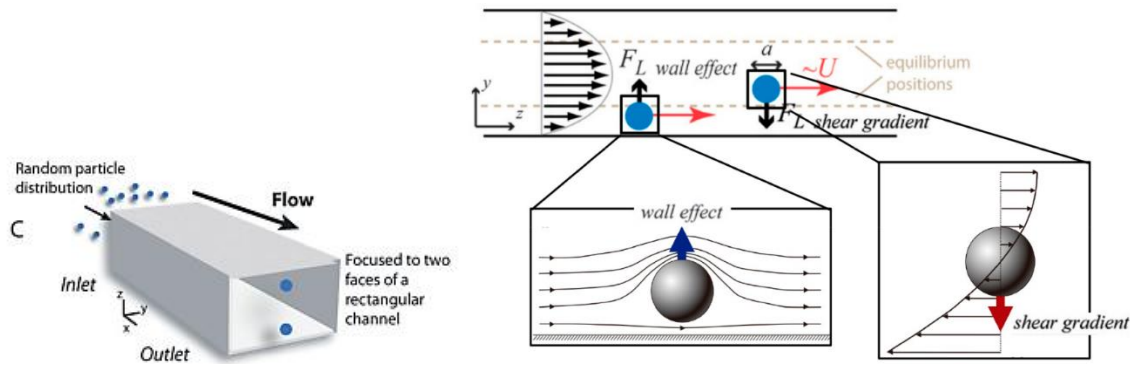


Fig. 3: two opposing lift forces action on particles in rectangular cross-section channels [17]

Solid rigid particles are used in many systems to study the migration mechanism, however, in real-life bio applications, i.e., cells, vesicles, and two-phase emulsion, are not rigid, and rather deformable. Deformability of particles can introduce additional nonlinearity to the system which results in additional lift forces. Fig. 4, illustrates different types of deformable particles, such as elastic solid particles, deformable droplets and capsules [17].

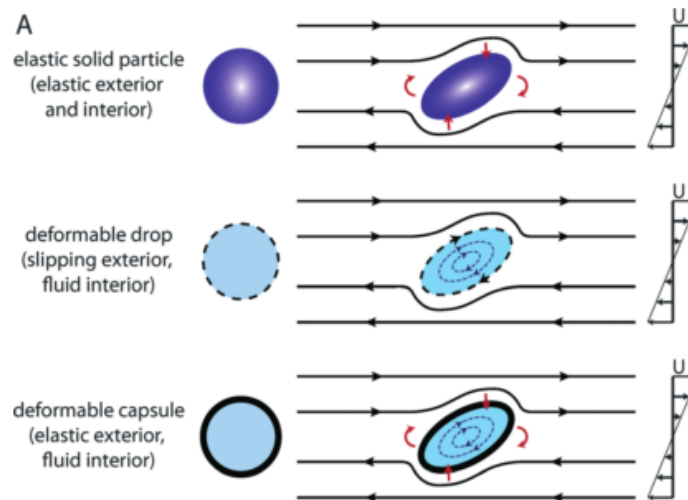


Fig. 4: deformable particles

### 3.2. Elastic particles

Lateral migration of elastic particles under shear flow condition was studied by Tam et al [20]. Small deformations caused by the viscous stresses acting on the surface of elastic particle creates an additional lift force in which results in a lateral migration of particles across undisturbed streamline. The deformation-induced lift force acts in superposition to inertial lift force which could alter the lateral equilibrium positions of deformable particles. The drift between the equilibrium position of elastic particles and solid particles suggests a possibility of particle separation based on deformability. If the system is calibrated well, the additional drift in the equilibrium position of the deformable particles could potentially be used to measure particle deformability [17].

The migration mechanism of solid and elastic particles is a step towards understating the more complex system of two-phase emulsions which is the focus of the current work. In the following we discuss the relevant forces that are imposed on liquid droplets in microchannels.

### 3.3. Liquid Droplets

A distinguishable difference between the dynamics of elastic particles and liquid drops was observed in an earlier work of Tam and Hyman (1973) [20] and a more recent study by Hur, et al [18]. Elastic particles experience no-slip condition on the surface, and the particle must adjust itself to the stresses, while in the case of liquid drops, the velocity and shear stress across the interface must be continuous to satisfy continuity equations - unless there is a surface tension gradient.

Additionally, there are some variations in the common forces, such as drag force, between droplets and particles, in which, due to the presence of a lubrication force droplets experience less drag compare to rigid particles [21].

### 3.3.1. Deformability-induced lift force

The non-solid interface between the droplet and the surrounding phase, results in additional dynamics that could contribute to the difference in the lateral migration mechanism of droplets compared to deformable elastic particles. Deformability of a droplet in a two-phase system creates additional forces that are not present for solid or elastic particles [21].

There are at least two factors contributing to the additional lift forces in deformable droplets; first is the change in the shape of the deformed droplet that creates asymmetry, and second factor is due to the non-linearities from matching forces on the interface between the two phases, i.e. the normal components of velocities and the tangential components of the viscous stresses must match at the interface. These result in a component of a force in the direction perpendicular to the undisturbed flow. Therefore, the direction of the lateral migration of droplets due to the deformation is towards the channel center, even in the absence of inertial forces [17]. The magnitude of the lateral drift can be related to the deformed shape of the droplet or the gradient of the forces at the interface.

### 3.3.2. Inertial lift force

In a two-phase emulsion droplet system, the inner phase is surrounded by a boundary that can slip under a flow of the outer (continuous) phase. Thus, the outer flow can influence the inner flow and create a recirculating flow inside the droplet. [17]. The deformation of droplets in viscous shear flow, leads to a lift force that causes the droplets to migrate towards low shear gradient regions, i.e. center of the channel in Poiseuille flow [22]. However, in the limit of moderate Reynolds number, the deformability-induced lift force might not fully explain the mechanism of droplet migration to the channel center and the contribution of other lift forces, such as inertial lift forces, viscoelastic and Marangoni lift forces needs to be investigated.

### 3.3.3. Other lift forces

In addition to the inertial lift force and the deformability-induced lift forces discussed earlier, there could be other forces due to the viscoelastic nature of non-Newtonian droplets, where nonuniform shear rate results in migration of droplets towards low shear rate region, or the presence of gradient in the concentration of surfactant at the interface of the two-phase systems, in which, the fluid will be pulled from lower surface tension region to higher surface tension region, resulting in a lateral migration towards channel center. The non-linearity caused by these forces creates additional lift forces on droplets.

The effect of buoyancy on the droplets for the case with mismatch densities between two phases could also be considered, especially when droplet size is considerably smaller than the channel height. Also, Dean forces could affect the lateral migration in the systems with curved channels. Fig. 5, illustrates some of the forces and their directions acting on the droplets.

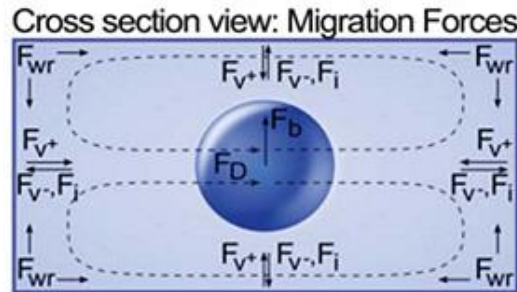


Fig. 5: Forces on droplets-  $F_d$ : Drag forces,  $F_b$ : Buoyancy,  $F_{wr}$ : Wall repulsion,  $F_{v^+}$ : Positive viscoelastic force,  $F_{v^-}$ : Negative viscoelastic force,  $F_i$ : Inertial forces (same direction as  $F_{v^-}$ ),  $F_D$ : Dean Forces (in case of curved channel) [13]

### 4.1. Scaling analysis

The dynamics of droplets is a complex study due to the various degrees of non-linearity. In order to understand the relative importance of the forces acting on droplets, which result in an overall lateral migration of droplets in microchannels, we must perform a scaling analysis. This



analysis enables us to understand how the balance of these forces may cause the droplets to laterality migrate, allowing to engineer microchannels for more efficient separation of droplets based on the drift in equilibrium positions.

The magnitude of the lift force and the lateral migration velocity depend on many parameters. The study of the relative importance of these forces can identify the main contributor to the lateral migration. Table 1 lists many independent variables that are associated with the complex two-phase system illustrated in Fig. 6.

Table 1: important parameters in identifying lift forces

Parameter	Symbol	Description
Channel dimensions	$H, W, L$	H: Height ( $\mu\text{m}$ ) W: Width ( $\mu\text{m}$ ) L: Length ( $\mu\text{m}$ )
Fluid properties	$\rho, \mu, \sigma, k, \lambda$	$\rho$ : Density ( $\text{kg/m}^3$ ) $\mu$ : Viscosity ( $\text{Pa}\cdot\text{s}$ ) $\sigma$ : Surface tension ( $\text{mN/m}$ ) k: Viscosity ratio, $k = \frac{\mu_d}{\mu_c}$ $\lambda$ : Relaxation time (sec)
Flow conditions	$U, u, v, w$	U: Average velocity (m/s) u: x-velocity (m/s) v: y-velocity (m/s) w: z-velocity (m/s)
Droplet size	a	a: diameter ( $\mu\text{m}$ )
Aspect ratio	$\varphi, \zeta$	$\varphi$ : channel aspect ratio, $\varphi = \frac{H}{W}$ $\zeta$ : droplet ratio, $\zeta = \frac{a}{H}$
Other contributors	-	Surfactant concentration, channel wettability, etc

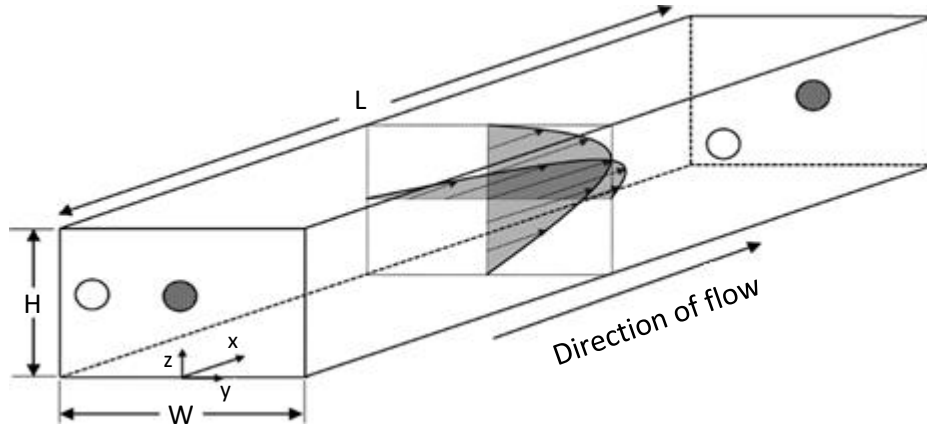


Fig. 6: independent parameters for scaling analysis

We can define many non-dimensional numbers to describe the system. However, in accordance with the forces that we introduced earlier, we identified the following dimensionless numbers to be the most significant ones to characterize the system.

#### 4.4.1. Reynolds number

Reynolds number is defined as the relative magnitude of viscous forces to inertial forces acting on fluid elements.

$$\text{Re} = \frac{\rho V L}{\mu} = \frac{\frac{\rho V^2}{L}}{\left(\frac{\mu V}{L^2}\right)} = \frac{\text{inertial force density}}{\text{viscous force density}},$$

Where  $\rho$  and  $\mu$  are the density and viscosity of the fluid, respectively, and  $V$  is the characteristic velocity of the fluid over a characteristic length  $L$ . Typically, in a rectangular channel, the characteristic length is defined as the hydraulic diameter,  $D_H = \frac{2HW}{H+W}$ .

The choice of the characteristic length could vary within systems depending on the importance of the parameters. For an instance, since we are exploring the relative strength of the inertial forces in the transverse direction, it is appropriate to choose channel width ( $W$ ) as

the characteristic length. Thus, the Reynolds number can be defined as follow, which characterizes the flow of carrier flow.

$$Re_c = \frac{\rho_c V_{avg} W}{\mu_c}$$

We can define a “particle” Reynolds number to characterize the motion of the droplet under local shear rate. The appropriate characteristic velocity is the local variation of velocity surrounding the droplet, rather than the average velocity in the channel. Therefore,  $V_{avg} \left(\frac{a}{W}\right)$  seems to be a good approximation for the characteristic local velocity across the droplet with radius  $a$ .

$$Re_p = \frac{\rho_c V_{avg} a^2}{\mu_c W}$$

Inertial lift forces on droplets become important for system with moderate Reynolds number.

#### 4.4.2. Capillary number

In the limit of low Reynolds number where viscous forces dominate inertial forces, droplets can still deform under shear flow. The relative importance of the viscous forces to interfacial forces are described as Capillary number,  $\frac{\mu_c V_{avg}}{\sigma}$ , where  $\sigma$  is an interfacial surface tension.

Capillary number is often used to quantify the extent of local deformation of a droplet, thus we can define “particle” Capillary number as follows:

$$Ca_p = \frac{\mu_c V_{avg} a}{\sigma W}$$

#### 4.4.3. Weber number

As the Reynolds number increases, deformation of droplet due to the fluid inertia can be described by Weber number. Weber number, the relative magnitude of inertial forces to interfacial forces, can be used to quantify droplet deformation.

$$We = \frac{\rho V_{avg}^2 a}{\sigma}$$

However, take into account the local velocity of droplet,  $V_{avg} \left(\frac{a}{W}\right)$ , the local deformation can be described as:

$$We_p = \frac{\rho V_{avg}^2}{\sigma} \left(\frac{a}{W}\right)^2$$

#### 4.4.4. Weissenberg number:

For viscoelastic fluids, we have in addition, a Weissenberg number, the ratio of viscous forces to the elastic forces, often used to characterize the viscoelasticity of the fluid. The definition might vary among sources, but usually is given by the relation of stress relaxation time of the fluid and a specific process time. For instance, in simple steady shear, it is defined as the shear rate times the relaxation time. Using the Maxwell Model and the Oldroyd model the elastic forces can be written as the first Normal force (N1) [23].

$$Wi = \frac{\text{elastic forces}}{\text{viscous forces}} = \frac{\tau_{xx} - \tau_{yy}}{\tau_{xy}} = \frac{\lambda \mu \dot{\gamma}^2}{\mu \dot{\gamma}} = \dot{\gamma} \lambda.$$

$\dot{\gamma}$  is the shear rate and  $\lambda$  is the fluid relaxation time.

#### 4.4.5. Viscosity ratio

Another important parameter in characterizing the shape of a deformable droplet is the ratio between the dynamic viscosity of fluids inside and outside of the droplet, dispersed and continuous phases, respectively.

$$k = \frac{\mu_d}{\mu_c}$$

Other non-dimensional numbers can be defined to compare various parameters within multiple systems, such as:

#### 4.4.6. Flow rate ratio

$$Q_r = \frac{Q_d}{Q_c}$$

#### 4.4.7. Channel aspect ratio

$$\varphi = \frac{H}{W}$$

#### 4.4.8. Droplet aspect ratio

$$\zeta = \frac{a}{H}$$

In this section we defined non-dimensional number which will be used to characterize the performance of the system in this study.

## 5. Conclusions

There are not available literature describing the magnitude of inertial lift force on droplets in moderate Reynold number regime. In this study we will investigate the effect of inertia in

migration of droplets and provide an empirical correlation to predict the magnitude of the inertial lift force. We use the scaling analysis and the non-dimensional parameters to describe the lateral migration mechanism.

## 6. References

- [1] H. N. Joensson and H. Andersson Svahn, "Droplet microfluidics-A tool for single-cell analysis," *Angew. Chemie - Int. Ed.*, vol. 51, no. 49, pp. 12176–12192, 2012.
- [2] M. Chabert and J.-L. Viovy, "Microfluidic high-throughput encapsulation and hydrodynamic self-sorting of single cells," *Proc. Natl. Acad. Sci.*, vol. 105, no. 9, pp. 3191–3196, 2008.
- [3] A. M. Klein et al., "Droplet barcoding for single-cell transcriptomics applied to embryonic stem cells," *Cell*, vol. 161, no. 5, pp. 1187–1201, 2015.
- [4] L. Mazutis, J. Gilbert, W. L. Ung, D. A. Weitz, A. D. Griffiths, and J. A. Heyman, "Single-cell analysis and sorting using droplet-based microfluidics," *Nat. Protoc.*, vol. 8, no. 5, pp. 870–891, 2013.
- [5] J. Clausell-Tormos et al., "Droplet-Based Microfluidic Platforms for the Encapsulation and Screening of Mammalian Cells and Multicellular Organisms," *Chem. Biol.*, vol. 15, no. 5, pp. 427–437, 2008.
- [6] W. Lee, L. M. Walker, and S. L. Anna, "Role of geometry and fluid properties in droplet and thread formation processes in planar flow focusing," *Phys. Fluids*, vol. 21, no. 3, 2009.
- [7] P. Zhu and L. Wang, "Passive and active droplet generation with microfluidics: a review," *Lab Chip*, vol. 17, no. 1, pp. 34–75, 2017.
- [8] H. Song, D. L. Chen, and R. F. Ismagilov, "Reactions in droplets in microfluidic channels," *Angew. Chemie - Int. Ed.*, vol. 45, no. 44, pp. 7336–7356, 2006.
- [9] J. Baret et al., "Fluorescence-activated droplet sorting ( FADS ): efficient microfluidic cell sorting based on enzymatic activity †," vol. 9, no. 13, 2009.
- [10] Z. Cao et al., "Droplet sorting based on the number of encapsulated particles using a solenoid valve," *Lab Chip*, vol. 13, no. 1, pp. 171–178, 2013.
- [11] E. Brouzes, T. Kruse, R. Kimmerling, and H. H. Strey, "Rapid and continuous magnetic separation in droplet microfluidic devices," *Lab Chip*, vol. 15, no. 3, pp. 908–919, 2015.
- [12] T. Jing, R. Ramji, M. E. Warkiani, J. Han, C. T. Lim, and C. H. Chen, "Jetting microfluidics with size-sorting capability for single-cell protease detection," *Biosens. Bioelectron.*, vol. 66, pp. 19–23, 2015.
- [13] A. C. Hatch, A. Patel, N. R. Beer, and A. P. Lee, "Passive droplet sorting using viscoelastic flow focusing," *Lab Chip*, vol. 13, no. 7, p. 1308, 2013.
- [14] C.-H. Yang et al., "Microfluidic emulsification and sorting assisted preparation of monodisperse chitosan microparticles," *Lab Chip*, vol. 9, no. 1, pp. 145–150, 2009.
- [15] S.-Y. Teh, R. Lin, L.-H. Hung, and A. P. Lee, "Droplet microfluidics," *Lab Chip*, vol. 8, no. 2, p. 198, 2008.

- [16] H. A. Nieuwstadt, R. Seda, D. S. Li, J. B. Fowlkes, and J. L. Bull, "Microfluidic particle sorting utilizing inertial lift force," *Biomed. Microdevices*, vol. 13, no. 1, pp. 97–105, 2011.
- [17] H. Amini, W. Lee, and D. Di Carlo, "Inertial microfluidic physics," *Lab Chip*, vol. 14, no. 15, p. 2739, 2014.
- [18] S. C. Hur, N. K. Henderson-MacLennan, E. R. B. McCabe, and D. Di Carlo, "Deformability-based cell classification and enrichment using inertial microfluidics," *Lab Chip*, vol. 11, no. 5, p. 912, 2011.
- [19] and A. S. Segre, G., "Behavior of macroscopic rigid spheres in Poiseuille flow," *J. Fluid Mech.*, vol. 14, no. 1958, pp. 136–157, 1962.
- [20] C. K. W. Tam and W. A. Hyman, "Transverse motion of an elastic sphere in a shear field," *J. Fluid Mech.*, vol. 59, no. 1, pp. 177–185, 1973.
- [21] R. M. Erb, D. Obrist, and P. W. Chen, "Predicting sizes of droplets made by microfluidic flow-induced dripping †," no. 10, pp. 8757–8761, 2011.
- [22] C. A. Stan, L. Guglielmini, A. K. Ellerbee, D. Caviezel, H. A. Stone, and G. M. Whitesides, "Sheathless hydrodynamic positioning of buoyant drops and bubbles inside microchannels," *Phys. Rev. E - Stat. Nonlinear, Soft Matter Phys.*, vol. 84, no. 3, p. 4840, 2011.
- [23] R. Poole, "The Deborah and Weissenberg numbers," *Rheol. Bull.*, vol. 53, no. 2, pp. 32–39, 2012.

## Chapter 2: Rheology

### 1. Material

In the work presented here, various solutions with different properties are used. The physical properties of the solutions must be known either from literature or experimental measurements. These properties include dynamic viscosity ( $\mu$ ), density ( $\rho$ ), interfacial tension ( $\gamma$ ), and relaxation time ( $\lambda$ ). Therefore, this chapter will introduce the methods used to measure these physical properties and compile results for all solutions used in droplet sorting studies.

Our passive droplet sorting system is a two-phase platform utilizing a continuous fluorinated oil phase in conjunction with a disperse aqueous droplet phase. The continuous phase is consistent throughout all experiments as Novec 7500 Engineered Fluid (3M, Maplewood, MN) with 0.5% Picosurf 1 (Sphere Fluidics, Babraham, UK) as surfactant to provide droplet stability. The properties of the continuous phase are easily referenced where  $\mu_c = 1.24\text{E-}3$  Pa.s,  $\rho = 1.61$  g/cm<sup>3</sup> at 20 °C, and  $\gamma = 16.2$  mN/m. All solutions were aqueous-based with additives such as glycerol, polyethylene oxide (PEO), polyacrylamide (PAA), cell lysate, and amplified DNA.

We used glycerol solutions with a range of 50-100% weight, and polymer-based solutions ranging from 1-3% weight, mixed in water. Glycerol was chosen as an additive because it is readily miscible in water and significantly increases fluid viscosity at high concentration. Viscosity of viscous solutions for various mixture, along with density measurement and the viscosity ratio are presented in Table 2.

Polymer solutions such as PEO and PAA were chosen because they are common water-miscible polymers with known viscoelastic properties. They mimic the structure of biological macromolecules such as DNA and serve as an analog to cell lysate solutions.



Relaxation time which is a property of non-Newtonian solutions, is measured only for polymer solutions, however, at very high shear rates, Newtonian solutions also exhibit some shear thinning behavior which is ignored in this study. To determine the required parameters for each polymer solution, data was analyzed using multiple rheological fitting methods such as the Power Law and Cross Models.

## 2. Methods:

The continuous phase oil was prepared by diluting 5% Picosurf 1 with additional Novec 7500. The aqueous glycerol solutions were prepared by adding the appropriate volumes of Glycerin (Sigma-Aldrich, St. Louis, MO) to distilled water using a positive displacement pipette (ThermoFisher Scientific, Canoga Park, CA). Aqueous polymer solutions were prepared by dissolving appropriate amounts of PEO MW~1E6 and PAA MW~5E6 - 6E6 (Sigma-Aldrich, St. Louis, MO) in distilled water at room temperature. To ensure solution homogeneity and prevent aggregation of polymer clumps, these solutions magnetically stirred at < 60 RPM for 48 hours. Rheometric analysis of all solutions were performed with a Discovery HR-2 Hybrid Rheometer (TA Instruments, New Castle, DE) using a 40mm 2.016° cone plate (TA Instruments, New Castle, DE) at shear rates of  $0.1 \text{ s}^{-1}$  to  $1000 \text{ s}^{-1}$  at constant temperature of  $20.00 \pm 0.01 \text{ }^{\circ}\text{C}$ . Shear stress, shear rate, and dynamic viscosity data were characterized using Trios Rheology Software then imported into Microsoft Excel and MATLAB.

For interfacial tension, a DSA-100 goniometer (Kruss, Hamburg, GE) was used to measure the pendant drop interfacial tension of 0.5% Picosurf 1 in Novec 7500 as the drop phase within a liquid phase of aqueous droplet solution. The disperse and continuous phase were switched for these measurements because the oil has higher density than the aqueous solutions. Videos were taken of droplet beading and the maximum drop size before detachment was used to trace drop profiles and calculate  $\gamma$  using the Pendent\_Drop ImageJ plugin [1]

### 3. Results & Discussion:

Table 2: Viscous solutions

Solution (% Wt)	$\eta_{avg}$ (Pa s)	$\rho$ ( $\frac{g}{cm^3}$ ) @ 20°C	$k = \frac{\mu_d}{\mu_c}$
Gly 100	1.0156	1.261	819.06
Gly 93.9	0.3343	1.246	269.63
Gly 92.5	0.3079	1.242	248.29
Gly 90.9	0.2436	1.238	196.48
Gly 88.5	0.1661	1.231	133.96
Gly 87.2	0.1434	1.227	115.63
Gly 85.5	0.1056	1.223	85.12
Gly 85	0.0958	1.222	77.27
Gly 80	0.0557	1.209	44.92
Gly 75	0.0335	1.195	27.05
Gly 70	0.0209	1.181	16.82
Gly 65	0.0150	1.168	12.06
Gly 55	0.0075	1.140	6.04
Gly 50	0.0056	1.124	4.55

Table 2 displays a full list of viscous solutions used as the disperse phase. Distinct sets of glycerol solutions were made for two different studies, one from 50-85% weight to assess the effects of viscosity on migration rate of viscous droplets to compare with the theoretical correlations proposed by Chan and Leal, and Hatch, et al, [2], [3], while another set from 85.5-100% was used to compare with viscoelastic polymer solutions. Density for glycerol solutions was obtained from literature [4] while density for non-glycerol solutions was taken to be approximately 1 g/cm<sup>3</sup> since they were at least 97% water. Rheometer measurements obtained data for shear stress, shear rate, and viscosity. Since glycerol solutions are known to be Newtonian, their viscosity did not vary significantly with shear rate as shown in Fig. 7.

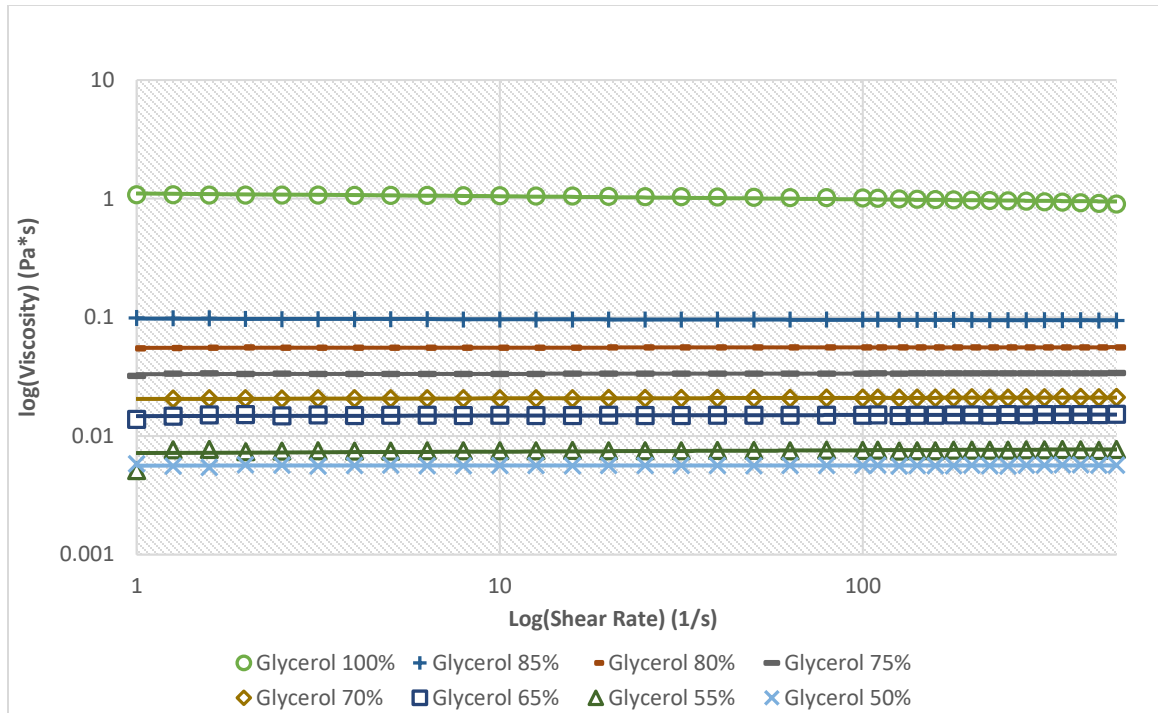


Fig. 7: Viscosity measurements for Newtonian solutions

As expected, viscosity increases rapidly at higher concentrations ranging from 5.6E-3 Pa.s for 50% glycerol to 1.02 Pa.s for 100% glycerol. This corresponds to a similar increase in viscosity ratio,  $k$ , yet density only ranges from 1.124-1.261 g/cm<sup>3</sup> at 20 °C.

The viscosity values were validated by comparison to previous work by Cheng et al (2008) [5], which determined an empirical correlation to determine aqueous glycerol solution viscosity at any concentration. Viscosity values from the correlation are compared to experimentally measured values in Fig. 8, which demonstrate high accuracy at concentrations from 50-85% weight, but at higher concentrations measured viscosity is lower than the literature value. Human error is a possible explanation for this discrepancy, since viscosity increases exponentially at higher concentrations and a small inaccuracy in volume can lead to a significant viscosity difference.

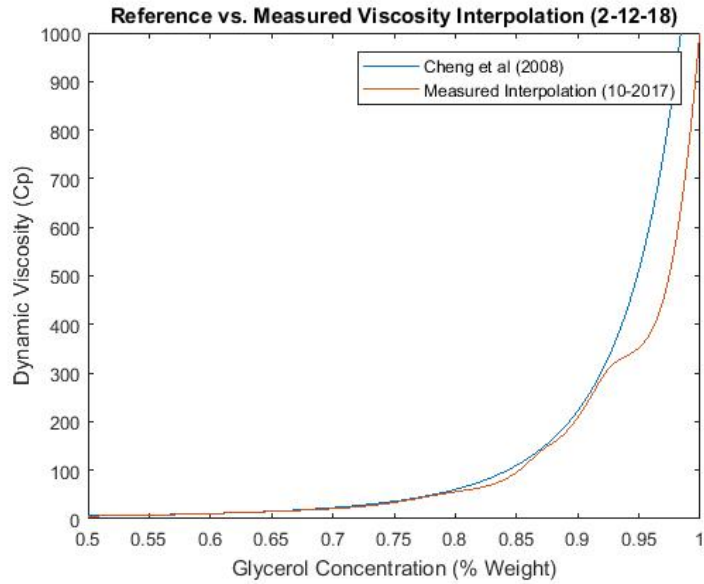


Fig. 8: Viscosity measurement compared with empirical correlations

The second set of glycerol concentrations from 85.5-93.9% were chosen based on the maximum shear rate experienced by droplets in the channel from the approximation proposed by Son et al (2007) [6]. This maximum shear rate was  $316 \text{ s}^{-1}$  and we aimed to match glycerol solution viscosity to the PEO solutions at this shear rate, so that a measurable viscosity difference and subsequent change in lateral migration could be observed as shear rate decreased in a portion of our device, so called, expansion region. In this case the PEO solution viscosity would increase at lower shear rates while that of glycerol solutions would remain constant. We then created a set of 3 glycerol solutions to compare with each PEO solution aiming for a perfect viscosity match at  $316 \text{ s}^{-1}$  together with  $\pm 25\%$  viscosity change.

All aqueous droplet solutions were first analyzed by the Power Law Model which characterizes Newtonian and Non-Newtonian flow behavior [7]. This model is widely used for intermediate shear rates such as the range of 0.1-1000  $1/\text{s}$  used in this study. Power law analysis is performed by fitting the rheometric flow curves of shear rate  $\dot{\gamma}$  ( $1/\text{s}$ ) versus shear

stress  $\sigma$  (Pa). Examples of flow curves and their Power Law fit lines for selected solutions are shown in Fig. 9. The Power Law Model given by, Koblan, et al, [8].

$$\sigma = K\dot{\gamma}^n$$

where K is referred to as the consistency index and is equal to the viscosity of a Newtonian solution at  $\dot{\gamma} = 1$  (1/s) while n is a dimensionless quantity called the fluid flow index. The fluid flow index measures deviation from Newtonian flow where if  $n = 1$  the solution is perfectly Newtonian, dilatant for  $n > 1$ , and pseudoplastic for  $n < 1$ . Table 3 and Fig. 9, compile results from Power Law analysis for all disperse phase solutions.

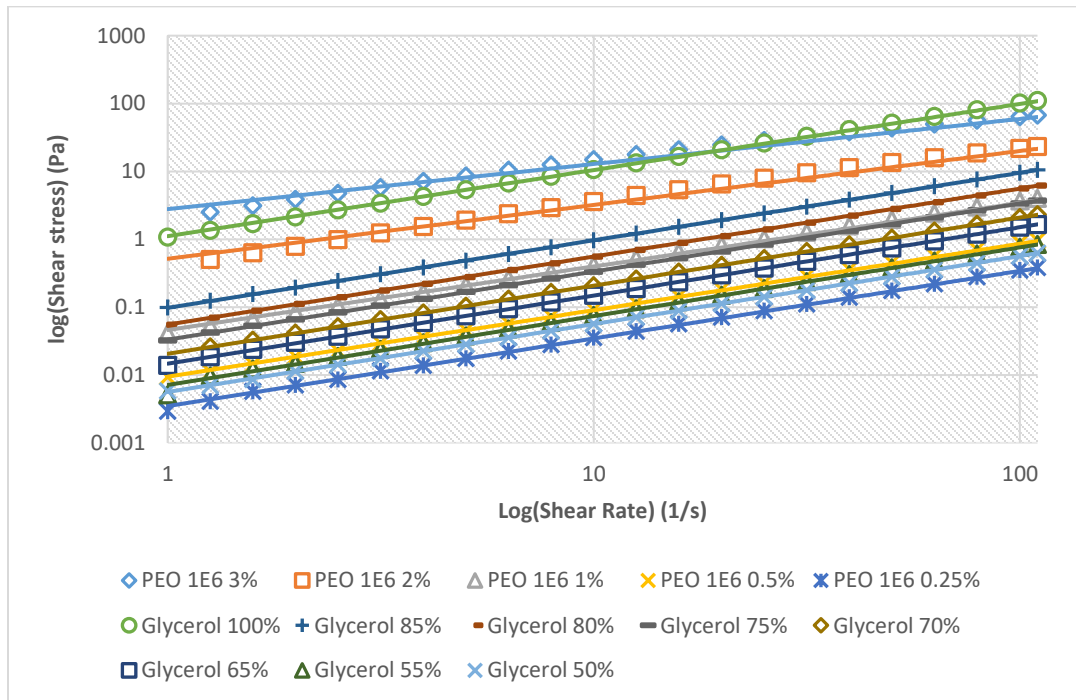


Fig. 9: Power law calculation for all solutions

Table 3: Power law calculation for various Newtonian and non-Newtonian solutions

Solution (Wt%)	K (Pa s <sup>n</sup> )	n
Gly 100	1.111	0.975
Gly 93.9	0.357	0.981
Gly 92.5	0.334	0.976
Gly 90.9	0.261	0.98
Gly 88.5	0.174	0.987
Gly 87.2	0.149	0.989
Gly 85.5	0.111	0.986
Gly 85	0.098	0.995
Gly 80	0.055	1.002
Gly 75	0.033	1
Gly 70	0.021	1.004
Gly 65	0.015	1
Gly 55	0.007	1.003
Gly 50	0.006	1.001
PAA 3	10.883	0.383
PAA 2	0.487	0.792
PAA 1	0.144	0.75
PEO 3	2.942	0.65
PEO 2.5	1.288	0.717
PEO 2	0.501	0.791

As expected, all glycerol solutions have flow behavior indices of ~1 which confirms their lack of shear-thinning Non-Newtonian properties. However, for polymer and biological solutions, fluid flow indices are as low as 0.383 for 3% PAA which represents significant shear-thinning behavior. Trends can be seen for these solutions where higher polymer concentrations yielded higher viscosity and a lower fluid flow index. These trends are intuitive because solutions with higher polymer concentrations will greater viscous interactions (cite). However, previous work by Ebagninin et al [8] found that at low concentrations, aqueous PEO solutions do not display significant shear thinning which was confirmed by their relatively high fluid flow indices. Thus, only PEO solutions from 2-3% weight were used for passive droplet sorting. PEO solutions with concentration higher than 3% could not be used because they greatly exceeded the viscosity of 100% glycerol and droplet generation became more difficult to control.

Likewise, a solution like 3% PAA was also too viscous to easily form droplets and was not included in further experiments.

The stress relaxation time ( $\lambda$ ), which is an important component of viscoelasticity can be determined by applying Cross Model analysis to the Non-Newtonian droplet solutions. Polymer relaxation time is related to the entanglement-disentanglement process between polymer chains as the solution is subjected to shear. Therefore, relaxation time is high in viscoelastic polymer solutions and very low for Newtonian solutions. The Cross Model is a modified version of the Power Law Model which covers a greater range of shear rates and includes a time constant parameter ( $\gamma$ ) which can be treated as a relaxation time for the solution [8]. The Cross Model equation is given by

$$\frac{\eta - \eta_{\infty}}{\eta_0 - \eta_{\infty}} = \frac{1}{1 + (\lambda \cdot \dot{\gamma})^m}$$

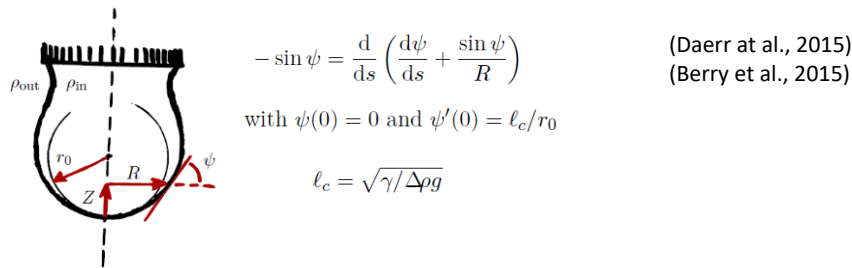
where  $\eta$  is the dynamic viscosity at a given shear rate,  $\eta_0$  and  $\eta_{\infty}$  are the asymptotic dynamic viscosities at zero and infinity,  $\lambda$  is the time constant or relaxation time (s),  $\gamma$  (1/s) is the shear rate, and  $m$  is the rate constant which indicates the degree of Newtonian behavior.

*Table 4: Cross model calculations*

Solution (% Wt)	$\lambda$ (s)	$m$	$\eta_0$ (Pa s)	$\eta_{\infty}$ (Pa s)
PEO 3	0.042	0.749	2.344	0.058
PEO 2.5	0.023	0.761	0.986	0.045
PEO 2	0.012	0.877	0.408	0.043
PAA 3	1.324	0.733	20.808	0.053
PAA 2	0.011	0.821	0.397	0.035
PAA 1	0.021	0.799	0.113	0.012

Cross Model analysis for Non-Newtonian droplet solutions is compiled in Table 4. The values for  $\lambda$  in PEO solutions are similar to those measured by Ebagninin et al. which confirms the accuracy of PEO solutions used in this study. This parameter will be used extensively in calculating the Weissenberg number (Wi) which characterizes degree of viscoelasticity in a solution.

Interfacial tension was measured using the pendant drop method described previously. For glycerol solutions, this process was straightforward due to the large index of refraction difference between glycerol and Novec 7500 which provided sufficient contrast for a drop outline to be traced. Interfacial tension between the oil and aqueous solution was calculated using the Young-Laplace Equation and subsequent parameters shown in Fig. 10.



Measurement accuracy verified using the Worthington Number  $Wo > \sim 0.6$  gives high accuracy

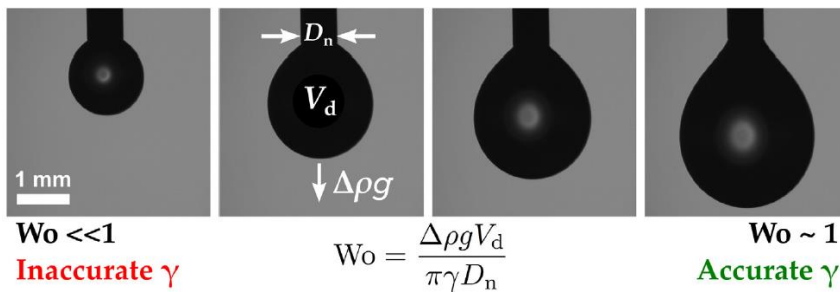


Fig. 10: Interfacial tension calculations [9]

However, for PEO and PAA solutions, this measurement was not as straightforward. PEO and Novec 7500 have a similar index of refraction thus the drop outline was not distinct. Contrast was altered and in some cases the droplet was colored black in Adobe Photoshop to



provide sufficient contrast for the Pendent\_Drop plugin the trace an outline. Although the pendant drop method is a simple method to measure interfacial tension it is associated with a high degree of error. Therefore, previous work by Berry et al. shown in Fig. 10 was used to confirm the accuracy of experimental interfacial tension measurements. They created a dimensionless Worthington number ( $Wo$ ) to characterize the accuracy of pendant drop measurements.

$$Wo = \frac{\Delta\rho g V_d}{\pi\gamma D_n}$$

In the  $Wo$ ,  $\Delta\rho$  represents the density difference between the two phases,  $g$  is the force of gravity,  $V_d$  is droplet volume,  $\gamma$  is the measured interfacial tension, and  $D_n$  is the needle diameter used to dispense the droplet. A  $Wo$  that trends toward 1 indicates an accurate measurement (Fig. 10) but it should be noted that the maximum value of  $Wo$  found in the paper was about 0.8. This is benchmark that the measurements for the solutions used in this study will be compared to. For each solution four droplets were dispensed and captured on the video before their interfacial tension was calculated and averaged in Table 5.  $Wo$  was calculated for each solution and all indicate high accuracy based upon their  $Wo$  which ranges from 0.634-0.793. Interfacial tension does vary between solutions and shows an increasing trend with higher glycerol concentration. A similar increase is shown in polymer solutions. These values are vital to calculating the Capillary number ( $Ca$ ) which characterizes droplet deformability.

Table 5: Validation of interfacial tension measurements

Solution (Wt%)	$\gamma$ (mN/m)	Wo
Gly 100	8.778	0.793
Gly 93.9	7.299	0.771
Gly 92.5	6.928	0.775
Gly 90.9	6.796	0.794
Gly 88.5	6.217	0.781
Gly 87.2	5.901	0.783
Gly 85.5	5.334	0.786
Gly 85	5.320	0.759
Gly 80	5.096	0.756
Gly 75	4.488	0.726
Gly 70	3.877	0.753
Gly 65	3.565	0.731
Gly 55	3.160	0.766
Gly 50	3.077	0.762
PAA 3	7.643	0.752
PAA 2	4.063	0.746
PAA 1	3.957	0.713
PEO 3	***	***
PEO 2.5	4.211	0.693
PEO 2	1.796	0.634

#### 4. Summary:

Now that the physical properties of relevant solutions used in this study have been evaluated, the dimensionless parameters for the entire system can be characterized. This data demonstrates that among all the physical properties measured ( $\rho$ ,  $\mu$ ,  $\gamma$ ,  $\lambda$ ) dynamic viscosity exhibits the greatest change across solution concentration in all solution types that were studied (Fig. 11). This indicates that viscosity is the dominant parameter dictating these dimensionless numbers and that tuning viscosity will have a more significant effect on droplet trajectories.

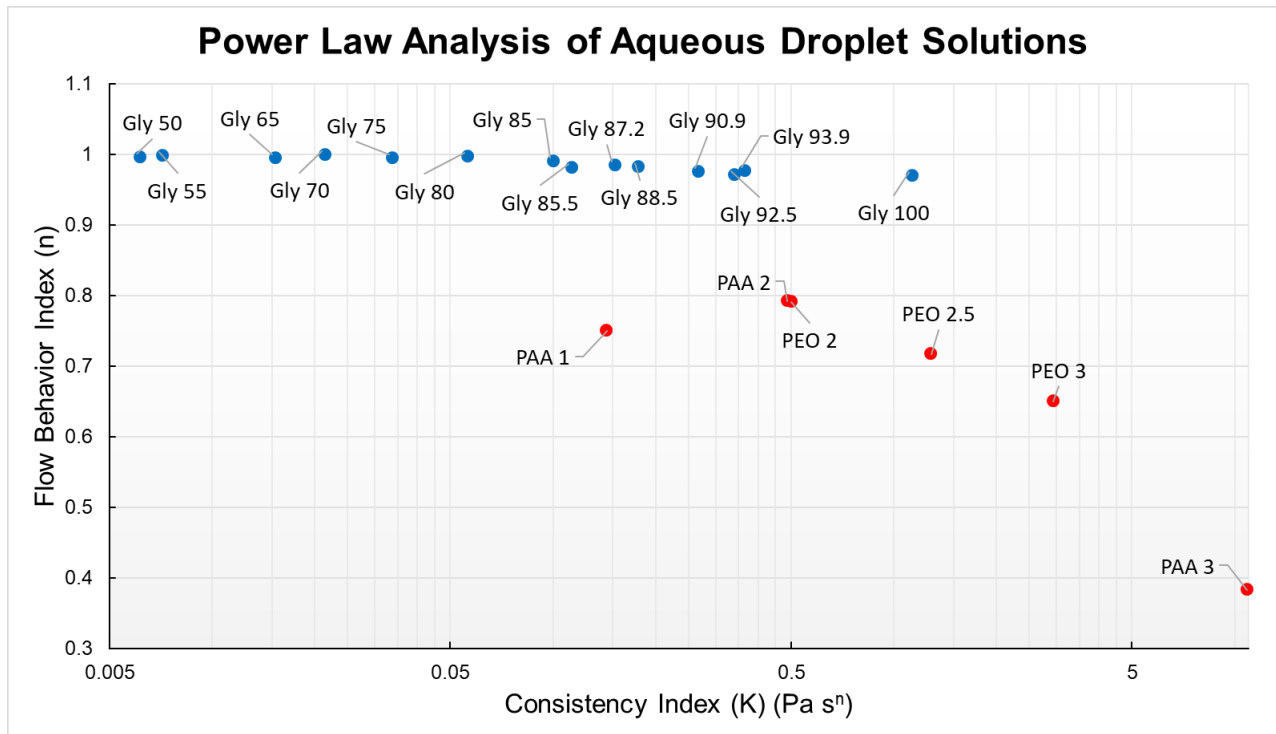


Fig. 11: Power Law analysis for viscosities of solutions

## 5. References:

- [1] D. S. Analysis, "DSA4 Software for Drop Shape Analysis User manual part 1: Installation, introduction, working in standard mode," 2004.
- [2] P. C. H. Chan and L. G. Leal, "The motion of a deformable drop in a second-order fluid," *J. Fluid Mech.*, vol. 92, no. 1, pp. 131–170, 1979.
- [3] A. C. Hatch, A. Patel, N. R. Beer, and A. P. Lee, "Passive droplet sorting using viscoelastic flow focusing," *Lab Chip*, vol. 13, no. 7, p. 1308, 2013.
- [4] Dow, "Density of Glycerine-Water Solutions," Edge, p. 99800.
- [5] N. Cheng, "Formula for Viscosity of Glycerol-Water Mixture," pp. 3285–3288, 2008.

- [6] Y. Son, "Determination of shear viscosity and shear rate from pressure drop and flow rate relationship in a rectangular channel," *Polymer (Guildf.)*, vol. 48, no. 2, pp. 632–637, 2007.
- [7] W. Lee, L. M. Walker, and S. L. Anna, "Role of geometry and fluid properties in droplet and thread formation processes in planar flow focusing," *Phys. Fluids*, vol. 21, no. 3, 2009.
- [8] K. W. Ebagninin, A. Benchabane, and K. Bekkour, "Rheological characterization of poly(ethylene oxide) solutions of different molecular weights," *J. Colloid Interface Sci.*, vol. 336, no. 1, pp. 360–367, 2009.
- [9] J. D. Berry, M. J. Neeson, R. R. Dagastine, D. Y. C. Chan, and R. F. Tabor, "Measurement of surface and interfacial tension using pendant drop tensiometry," *J. Colloid Interface Sci.*, vol. 454, pp. 226–237, 2015.

## Chapter 3: Microfluidics platform

### 1. Device fabrication

The microfluidics devices used in this study were fabricated by standard soft lithography techniques in a cleanroom facility. The 2D geometry was designed in AutoCAD (Autodesk, San Francisco, CA) then inverse printed to create a transparency that included measurement tick marks for spatial orientation. Liquid photoresist KMPR 1050 (or KMPR 1025) (Microchem, Westborough, MA) was spin coated onto a 4-inch diameter silicon wafer solidified via baking at 95 °C for 5 minutes. Next, the photoresist was covered with a photomask and exposed to UV light. The wafer was washed with developer solution to remove unexposed photoresist, thus, creating the device mold with feature height measured by a surface profiler Dektak (Bruker, Goleta, CA). Polydimethylsiloxane (Sylgard-184) (Dow-Corning, Midland, MI) with a 10:1 base to crosslinker ratio was poured over the mold then baked at 65 °C for minimum 4 hours before being cut and punched with a 0.5 mm blunt nosed needle to create inlets and outlets. Finally, the chamber was plasma treated for 45 - 60 seconds at 500 mTorr, then bonded to a glass slide (VWR, Radnor, PA), to fabricate a fully functional microfluidic device. Prior to experiments, devices were treated with Aquapel (Aquapel Glass Treatment, Pittsburgh, PA) to remove hydrophilicity in the device channels. Fluid flow was introduced into the device using Polyetheretherketone (PEEK) (Idex, Oak Harbor, WA) and Tygon (US Plastics, Lima, OH) tubing [1].

### 2. Device design

Different variations of devices were tested in this study, however, the device as will be referred to as the integrated device was used for most of the experiments performed here. The integrated device consists of a droplet generator upstream, integrated to a separation platform. This integrated device continuously generates droplets upstream and the droplets move to the

downstream platform for analysis/ sorting. The integrated device requires 4 independent syringe pumps. Two for droplet generation, one for the sheath flow, and a final syringe pump to act as a spacer flow for droplets before they enter the main channel (Fig. 12).

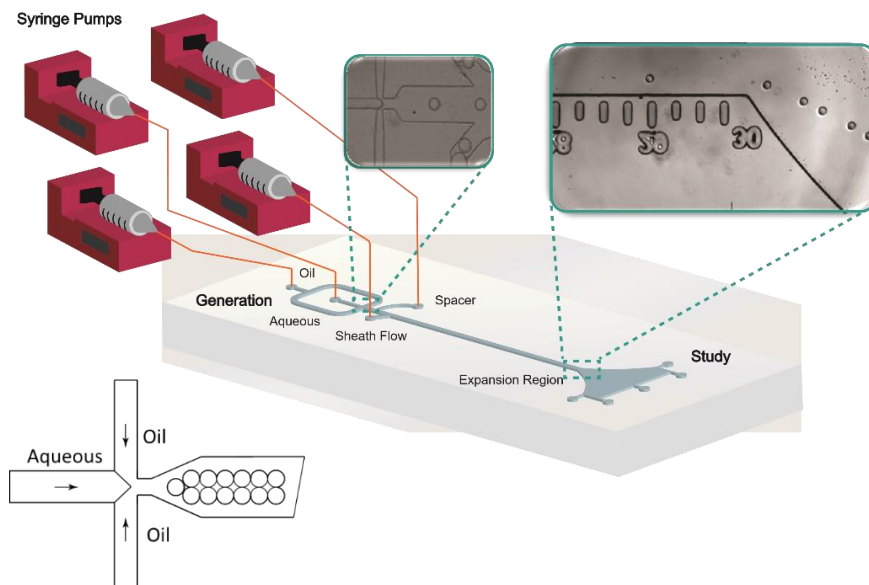


*Fig. 12: schematic of an integrated device with a 2-inlet droplet generation device*

Alternatively, for many applications where incubation of some sort is required, a droplet generation device was designed separately, and generated droplets were stored in an off-chip reservoir before they were injected to the separation platform. The incubation device has a separate droplet reservoir and generator devices from the main channel which can be interchanged depending on the type of droplets we intend to study (Fig. 13). Since each component is run separately for this device only two syringe pumps are needed for each stage of the system.

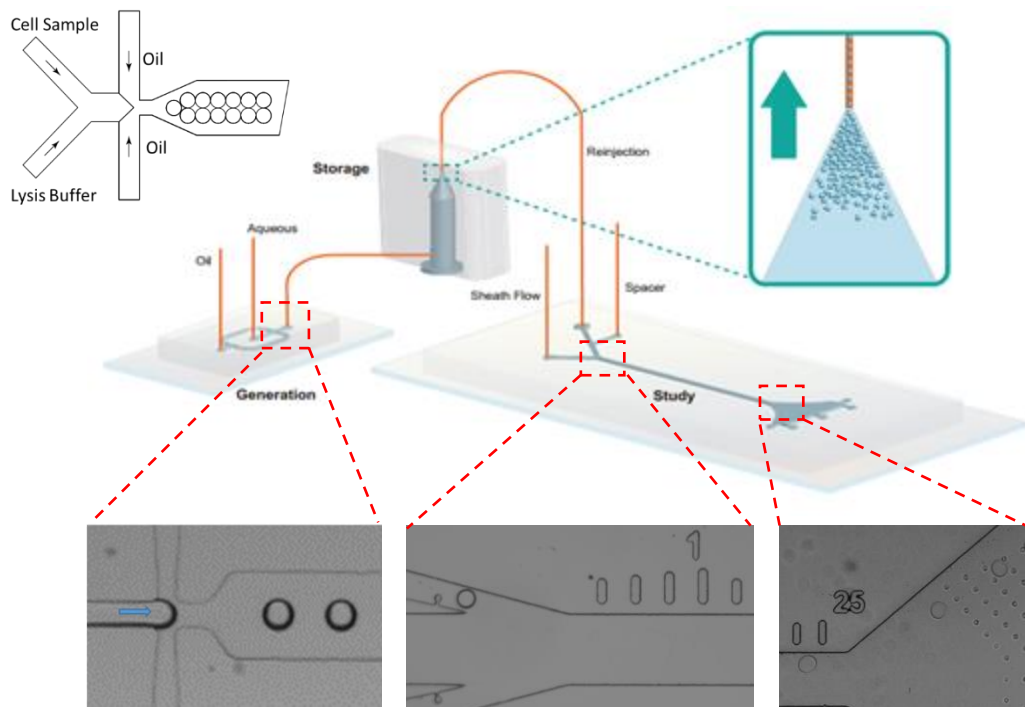


*Fig. 13: Schematic of alternative device for applications requiring incubation with a 3-inlet droplet generation device*

The fabrication process explained earlier was used for both the integrated device and the off-chip incubation device.

## 2.1. Integrated device

In the integrated device, the original flow focusing droplet generator was redesigned and integrated with the main channel in a two-layer mold fabrication process. To minimize droplet interactions a spacer stream was added in between the droplet generator and the main channel (Fig. 12). In this device, at it will be explained in Chapter 4, droplet sizes can be adjusted via altering the ratio between the droplet generator flow rates and the spacer flow rate as long their sum remains constant to ensure consistency in the main channel's flow fields. Following generation, the droplets enter the main channel and are pushed to the channel wall by the sheath flow when they initially enter the channel. They then migrate towards the center of the channel as they travel along the channel towards the expansion region where their physical

properties catalyze differences in trajectory and provides a mechanism for passive sorting. For these studies the sheath flow rate has been kept constant at 100  $\mu\text{L}/\text{min}$  while the sum between generation and spacer has been either 6  $\mu\text{L}/\text{min}$  or 9  $\mu\text{L}/\text{min}$ . While the height of the droplet generator portion has stayed constant at 50 microns, the height of the main channel has varied from 50-150 microns across various devices to measure droplet response to dynamic deformation.

For an integrated device, three types of droplet generator and two different separation channels were used based on the experiments. Droplet generation were fabricated with the height of 60-70  $\mu\text{m}$  and the separation channel varied between 50  $\mu\text{m}$  to 150  $\mu\text{m}$ . We fabricated 2-layer device in order to be able to control the size of each section. Any combination of the following can be used (Fig. 14).



Generation section (upstream)

Separation section (downstream)

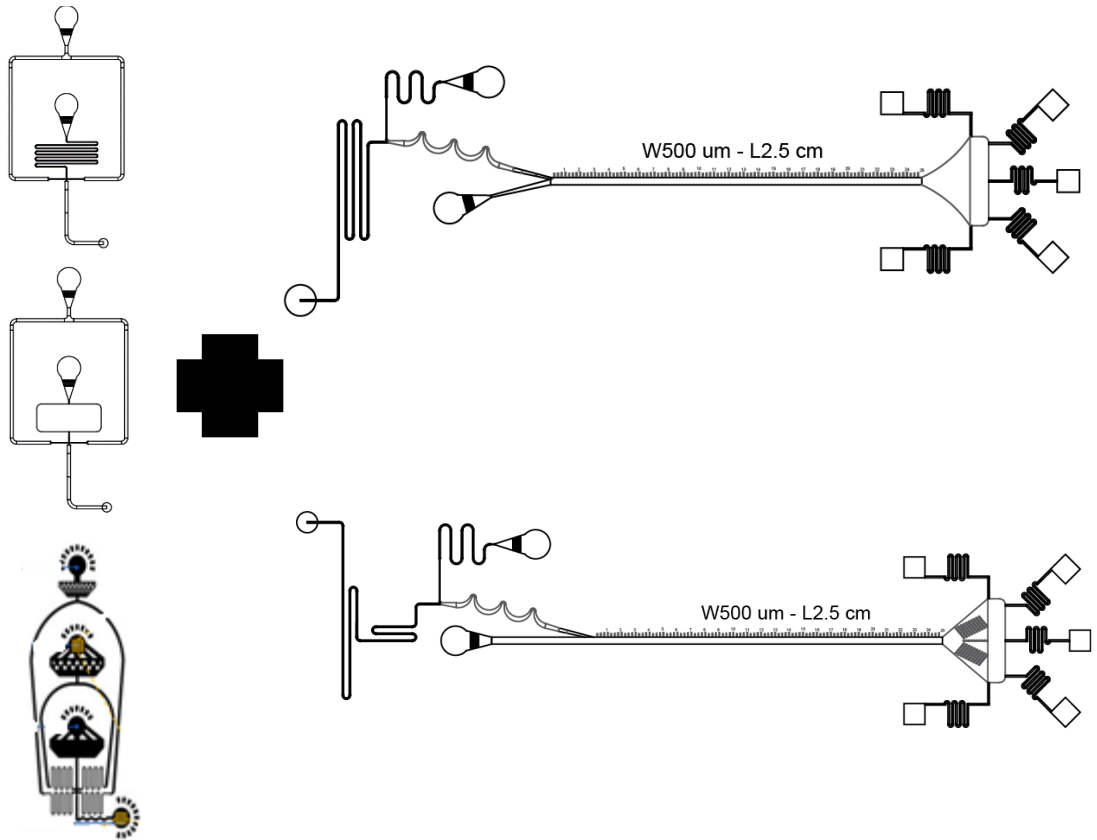


*Fig. 14: various combination of integrated device*

Three different channels for the downstream were used in this study:

Device 1):  $W = 500 \mu\text{m}$ ,  $H = 120 \mu\text{m}$ ,  $L = 2.5 \text{ cm}$  (in the main channel)  $\rightarrow$  channel aspect ratio  $\varphi = 0.24$  (Used in Chapter 5)

Device 2):  $W = 500 \mu\text{m}$ ,  $H = 150 \mu\text{m}$ ,  $L = 2.5 \text{ cm}$  (in the main channel)  $\rightarrow$  channel aspect ratio  $\varphi = 0.3$  (Used in Chapter 6)

Device 3):  $W = 500 \mu\text{m}$ ,  $H = 50 \mu\text{m}$ ,  $L = 2.5 \text{ cm}$  (in the main channel)  $\rightarrow$  channel aspect ratio  $\varphi = 0.1$  (Used in Chapter 7)

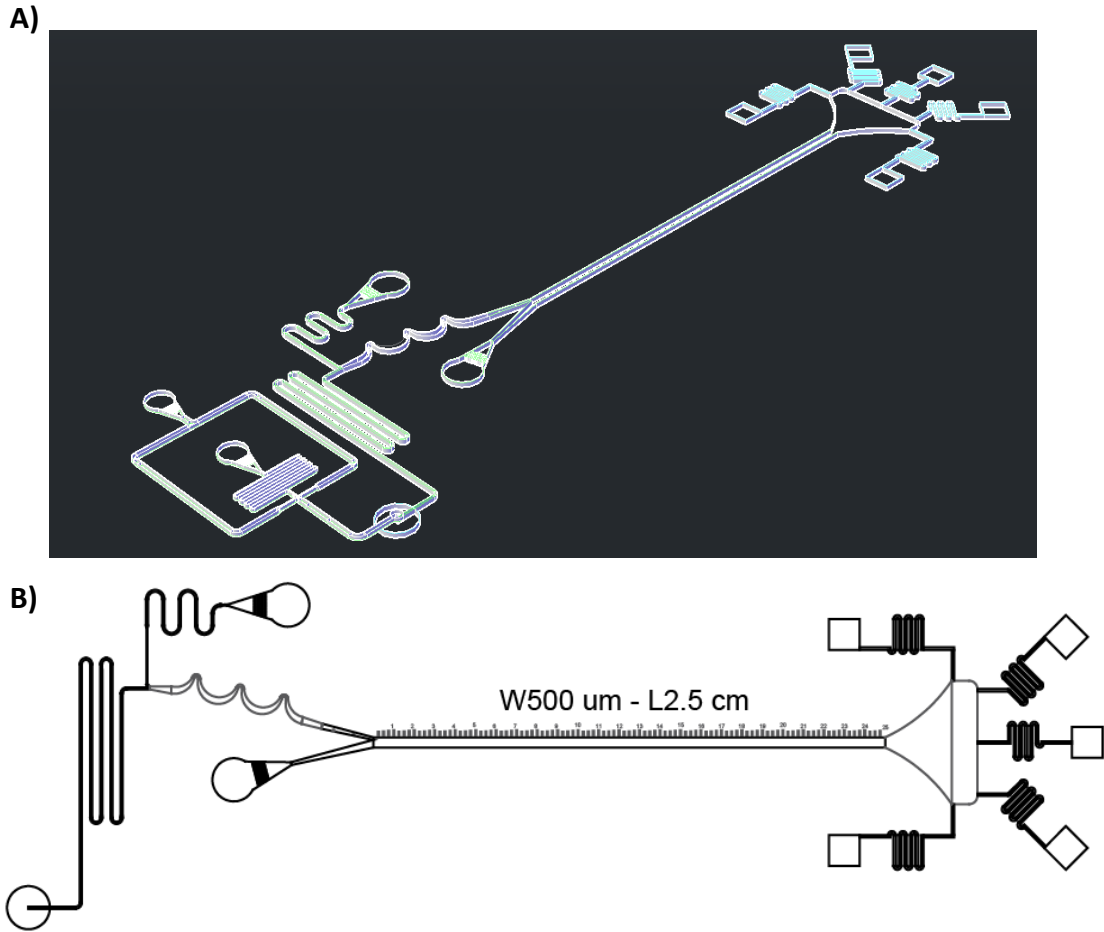


Fig. 15: schematic of a simple 2-inlet droplet generator device, A) Integrated device B) Incubation device

We will discuss the performance of various devices in depth in later chapters: droplet generation in Chapter 4 and the separation study in Chapter 5,6, and 7.

## 2.2. Incubation device

A device so called, Incubation device, consists of a separate droplet generation and a separation platform, with different variations of off-chip reservoirs. Some designs with on-chip storage reservoirs were also tested but not included in this ty. (Fig. 13). The droplets can be generated and collected for off-chip incubation then reinjected into the storage reservoir.

Natural buoyancy force will cause the droplets to rise toward the top of the storage reservoir to be flowed into the main study device. The ability to store droplets off-chip and reinject afterwards is important for applications such as PCR with DNA-based droplets or when encapsulating cells or cell lysate which require lengthy incubation processes [2][3][4].

### 3. Device iterations

Before we came to the finalized “integrated” and “incubation” platforms, this system underwent many different design iterations. The primary challenges in designing an efficient droplet sorting platform came from the droplet reservoir. Initially, the reservoir was a 3D printed block that was glued onto the silicon wafer mold by UV curing while droplet generation occurred on a separate flow focusing device. This reservoir was very tall compared to the rest of the channel and the device had to be flipped over when running experiments or else it would be impossible for droplets to move down the reservoir due to the buoyancy. However, when this happened we encountered problems with analyzing droplets in isolation because there was no method to control their entry into the main channel. This resulted in immediate loss of 50-80% of the generated droplets as well as difficult in operating the system upside down and a significant loss in image quality.

Additional experiments were run with the large on-chip reservoir concept. The first concept utilized a reservoir that was independently filled with mineral oil to gradually force droplets into the channel without flipping the device (Fig. 16A). Unfortunately, this design was not successful because the interface between mineral oil and the aqueous droplet layer formed a convex meniscus which prevented droplets from reaching the device channel. Additionally, once the reservoir was fully filled there was backflow out of the mineral oil inlet due to the greater fluidic resistance on the device side (Fig. 16C).

The second design change made the reservoir open and create a more flexible PDMS cap which was flexed by magnets on either side of the device. The magnetic force caused the reservoir cap to compress and force some droplets into the channel without flipping the device (Fig. 16B). This method ultimately proved to be impractical because repeated flexion of the reservoir cap caused premature rupture of the PDMS and the compression pulse inadvertently affected the velocity fields within the main channel. It was also observed that the magnet often simply forced droplets to the side of the reservoir rather than down into the channel (Fig. 16D).

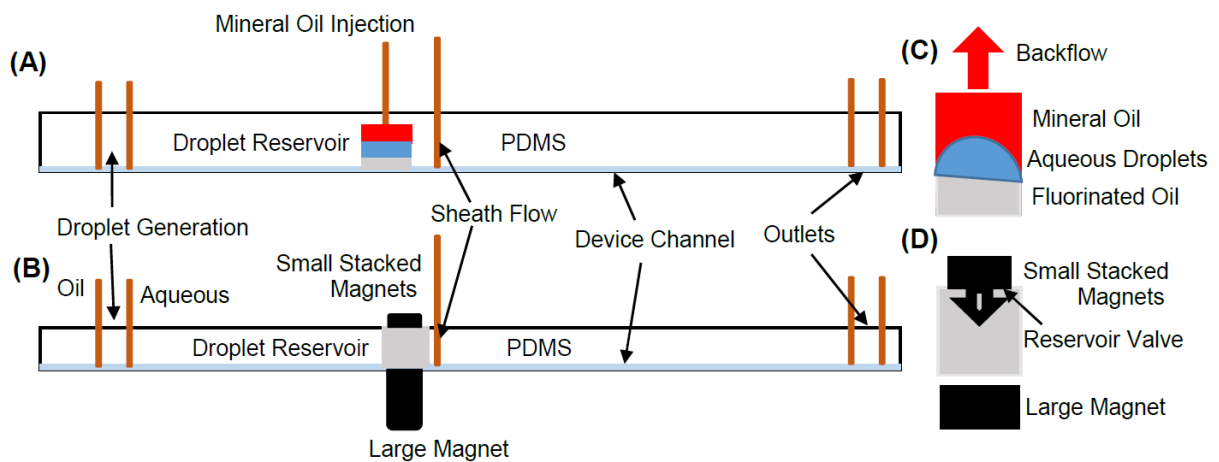


Fig. 16: Various attempts for design improvements

The next iteration of the system had a redesign of the droplet reservoir. Instead of using a 3D printed plastic block, layers of scotch tape were pasted directly onto the wafer and reapplied periodically. This layered reservoir was much easier to manufacture compared to a multilayer silicon wafer chip and was highest at the droplet inlet before incrementally stepping down into the channel entrance. This ensured that droplets did not get stuck prior to entering the channel and prevented the large influxes of interacting droplets seen in previous designs. The original reservoir shape was oval (Fig. 17A) but various geometries were tested before a S-shape was found to be the most effective at maximizing droplet yield from the reservoir into the channel (Fig. 17B & C). Since the taped reservoir had limited volume compared to previous

component, an off-chip storage device was engineered in conjunction with this design. It consisted of an Eppendorf tube sealed in a PDMS block which prevented leakage and allowed for efficient reinjection into the droplet reservoir. Ultimately this design was not favored over the subsequent integrated device because frequent re-taping of the reservoir was required which resulted in inconsistent reservoir performance. Furthermore, the height of scotch tape proved to be too low at times and resulted in droplet deformation which caused coalescence in some cases (Fig. 17D).



*Fig. 17: Reservoir design iterations*

Following retirement of the taped droplet reservoir, the integrated droplet sorting system with continuous generation was developed, as it was discussed earlier.

#### 4. References:

- [1] † Dongeun Huh et al., “Gravity-Driven Microfluidic Particle Sorting Device with Hydrodynamic Separation Amplification,” vol. 79, no. 4, pp. 1369–1376, 2007.
- [2] C. Zhang and D. Van Noort, *Cells in microfluidics*, vol. 304. 2011.
- [3] A. Didelot et al., “Multiplex picoliter-droplet digital PCR for quantitative assessment of DNA integrity in clinical samples,” *Clin. Chem.*, vol. 59, no. 5, pp. 815–823, 2013.
- [4] N. R. Beer et al., “On-chip single-copy real-time reverse-transcription PCR in isolated picoliter droplets,” *Anal. Chem.*, vol. 80, no. 6, pp. 1854–1858, 2008.

## Chapter 4 - Droplet generation

### 1. Introduction

One key parameter in droplet generation is the droplet size. Droplet size largely impacts the droplet migration mechanism for separation purposes. It also determines the sample volume in various applications essential for controlling reactions, which signifies the importance of generating monodisperse droplets. In addition, it is an important parameter in evaluating the non-dimensional numbers that are used to characterize the system.

To better exploit the potential of droplet microfluidics, a physical understanding of the droplet formation process is required. In a general sense, droplets originate from instabilities of two phases; typically, two immiscible fluids meet and create an immiscible interface, then a large deformation of the interface brings it to an unstable state, which in turn leads to fragmentation of the unstable interface, resulting in the formation of discrete droplets[1] [2].

### 2. Droplet generation methods

There are several methods of droplet generation in microfluidics, mostly passive and a few active methods. In this work, we only discuss some of the passive methods.

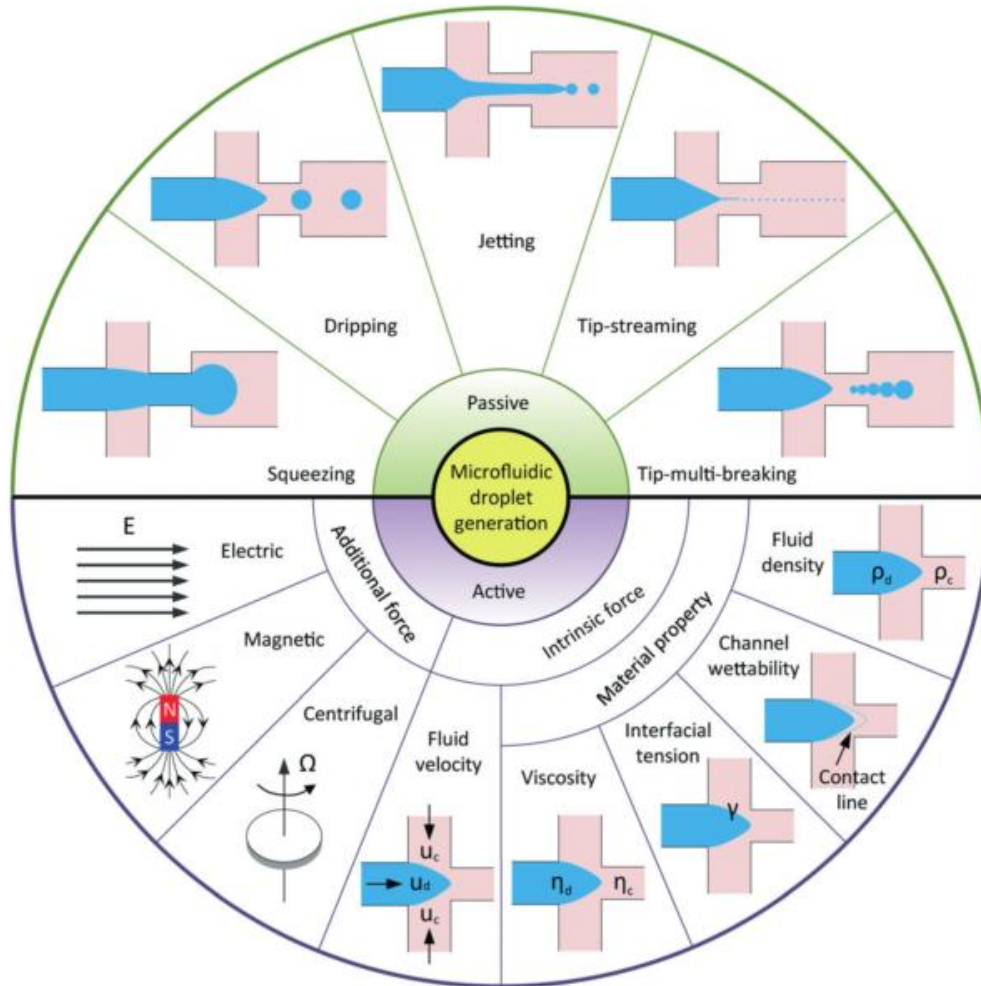


Fig. 18: Schematic of passive and active droplet generation [2]

The confinement of microfluidic channels creates a restriction in the flow of liquids which impacts the droplet generation. Fig. 19 shows some of the typical droplet generation devices. Major passive droplet formation devices include: Co-flow, flow focusing and cross-flow (T-junction) which use viscous shear force to break up droplets and step emulsification which uses the variation in channel confinement to facilitate the droplet breakup. In this work we chose to use flow focusing device throughout the experiments for several reasons that will be explained further throughout this chapter.

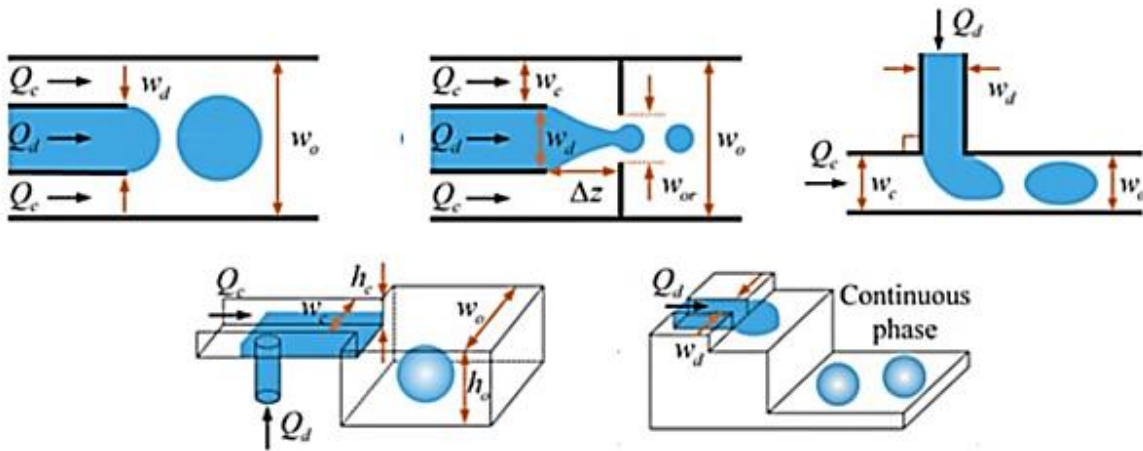


Fig. 19: Typical microfluidic droplet generation devices [2]

## 2.1. Flow Focusing Device

In a flow focusing device, a stream of a continuous liquid surrounds a central stream containing a second immiscible liquid of a dispersed phase. Thereafter, the liquids flow together and elongate through a contraction where the central stream breaks into disperse droplets.

An important question is: What are the characteristics of the system?

To better understand the mechanism behind the formation of droplets in flow focusing device we can study the parameters within the following three categories:

- Geometric characteristics
- Flow characteristics (flow rates of each liquid)
- Fluids properties

The overall dimension of the flow focusing device influences the droplet formation.

Schematic of a flow focusing device is shown in Fig. 20.



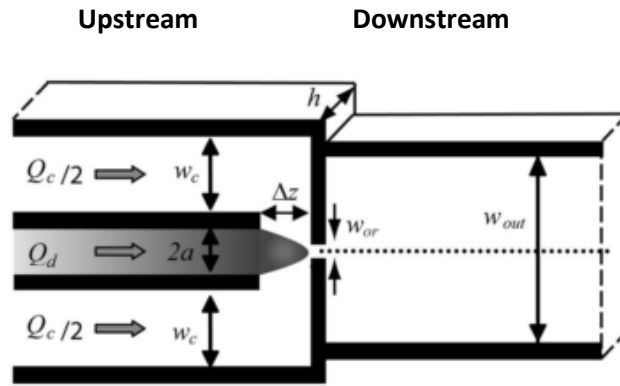


Fig. 20: schematic of planar flow focusing device [3]

The geometric characteristics of the flow focusing device includes the width of oil and aqueous channels ( $w_c$  and  $w_d$ , respectively), the width of the orifice ( $w_{or}$ ) in which the two immiscible liquids flow in together, its distance ( $dz$ ) downstream from the end of the aqueous channel, the width of the outlet channel ( $w_{out}$ ) and the height of the channel ( $h$ ). The volumetric flow rates of the two liquids,  $w_c$  and  $w_d$ , are controlled independently and each one influences the droplet formation differently. The fluid properties including, densities  $\rho_c$  and  $\rho_d$ , viscosities  $\mu_c$  and  $\mu_d$ , and the interfacial tension between the liquids  $\sigma$  play a role in droplet formation mechanism. Here, the subscripts  $c$  and  $d$  denote the continuous and dispersed phase of this two-phase system, respectively.

For a given geometry of the flow focusing device, the flow rate of the continuous phase impacts the droplet volume (size) the most and the aqueous flow rate is mainly controlling the time interval (frequency) between the generation of discrete droplets [4]. Since the droplet size is coupled to the device geometry, the length scale of the device fabrication controls the lower limit of the droplets size. Thus, if generating smaller droplets are desired, it requires fabrication of a smaller scale device; which in turn it typically requires a more expensive and complex fabrication processes [3] and makes the devices more susceptible to small scale complications, such as high internal pressure and clogging issues.

### 3. Scaling Analysis (droplet generation)

The behavior of immiscible liquids of the continuous phase and the dispersed phase in a two-phase flow is well described by the continuum hypothesis [5]. The continuity equation and the Navier-Stokes equation [6] for incompressible Newtonian fluids (momentum equation) are shown in the following equations:

$$\nabla \cdot \mathbf{u}_s = 0,$$

$$\rho_s \frac{\partial \mathbf{u}_s}{\partial t} + \rho_s \mathbf{u}_s \cdot \nabla \mathbf{u}_s = -\nabla p_s + \eta_s \nabla^2 \mathbf{u}_s + \mathbf{f}_s,$$

Subscript 's' denotes either 'd' or 'c', corresponding to dispersed or continuous phase fluid, respectively. However, it is important to understand the flow conditions and the forces on the interface between the two immiscible phases [7][8]. According to the continuity the normal components [9] of the velocity and the tangential viscous stresses [10] [11] should be continuous, this mean:

$$\mathbf{u}_d \cdot \mathbf{n} = \mathbf{u}_c \cdot \mathbf{n},$$

$$\boldsymbol{\sigma}_d \cdot \mathbf{t} = \boldsymbol{\sigma}_c \cdot \mathbf{t},$$

Also, the Normal stress difference between the two phases should balance the capillary pressure

$$\mathbf{T}_d \cdot \mathbf{n} - \mathbf{T}_c \cdot \mathbf{n} = -\gamma \kappa,$$

Based on the governing equations described herein, we can identify the corresponding forces that govern the droplet formation. The following forces (inertia, viscous and capillary forces) are presented in terms of stress (force per unit area) with 'L' being the characteristic length.

$$f_i \sim \rho_s u_s^2$$

$$f_v \sim \eta_s u_s / L,$$

$$f_\gamma \sim \gamma / L$$

In principle we can define a non-dimensional number by comparing the ratio of any of the two stresses.

#### 4. Droplet break-up

Droplet break-up process is controlled by a balance between interfacial tension forces, viscous stresses and inertial forces acting on the droplets. Viscous forces causing deformation of the droplet and the interfacial tension forces resist deformation by minimizing the interfacial area (minimum interfacial energy) [2] [12]. Dimensionless numbers are used to characterize the relative importance of these forces. Inertial forces are typically neglected in droplet generation as the flow rates are quite low [13]. Provided that the relative importance of inertial forces to viscous forces, so called Reynolds number, is significantly small [14][15]. There are two main dimensionless numbers that can be used to characterize the droplet formation process[16]. The relative importance of viscous forces to the interfacial forces is described by the Capillary number. [3]. It is also called dimensionless shear rate [12].

$$Ca = \frac{\mu_c G a}{\sigma}$$

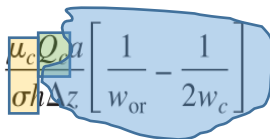
Where  $G$  is the effective rate of strain (fluid shear rate),  $\sigma$  is equilibrium interfacial tension,  $a$  is the undeformed droplet radius, which in this case is half of the channel width of the dispersed phase liquid [3].

$G$  is defined in terms of the velocity gradient along the channel centerline.

$$G \approx \frac{\Delta U}{\Delta z}$$

$$Ca \equiv \frac{\mu_c a}{\sigma} \frac{\Delta U}{\Delta z}$$

According to Lee, et al [3],  $\Delta U$  can be estimated as the difference between the average velocity of the continuous phase and the velocity inside the constriction (orifice). The final expression for the Capillary number is then described as

$$Ca \equiv \frac{\mu_c a}{\sigma} \frac{\Delta U}{\Delta z} = \frac{u_c Q_d a}{\sigma h \Delta z} \left[ \frac{1}{w_{or}} - \frac{1}{2w_c} \right]$$


geometric characteristics

Flow conditions, flow rate ratio  $\varphi = \frac{Q_d}{Q_c}$

Fluid properties, viscosity ratio  $\lambda = \frac{\mu_d}{\mu_c}$

The contribution of geometry, flow conditions, and fluid properties can be distinguished in this correlation [10][17]. For a given geometry for the droplet generation, the flow rate ratio between dispersed and continuous phases flow rates can determine the size and frequency of a droplet generation [3]. Oftentimes we deal with different types of solutions with various properties, therefore, the same flow rate ratio to obtain the same size droplet would not be possible, and new flow conditions should be used to balance the  $Ca$  number correlation. We

can generate a so-called flow map, to establish some operating conditions, and obtain various conditions for different size of droplets, for a given set of continuous/ dispersed solutions.

## 5. Flow map

It is often a common practice to generate a flow map a specific droplet generation device to characterize the operation of the system as function of flow rates of both phases.

Fig. 21 shows an example of such an analysis [2]. Based on the magnitude of the Capillary number five different modes of the droplet generation in the flow focusing device can be identified as: squeezing ( $Ca < 0.1$ ), dripping ( $0.1 < Ca < 0.3$ ), jetting, tip streaming ( $0.6 < Ca < 0.8$ ), and tip-multi-breaking ( $0.4 < Ca < 0.5$ ) [18][19][20][21]. The transition between different modes occurs when either or both flow rate passes a critical value. The jetting and tip-streaming usually happen at high flow rates of the dispersed phase and the continuous phase, respectively. In the squeezing regime, channel confinement inhibits the capillary instability during the droplet growth and pinch off making the drop formation a quasi-static process [22][23]. In contrast, the other modes, Rayleigh-Plateau instability plays a dominant role in droplet break up [24]. Identifying the regimes in which the droplet generation is performing in our experimental data is not a part of the current work. However, based on our observation the droplet formation in this study falls under the dripping mode for the most part, and for some extreme cases under the squeezing and jetting regimes.

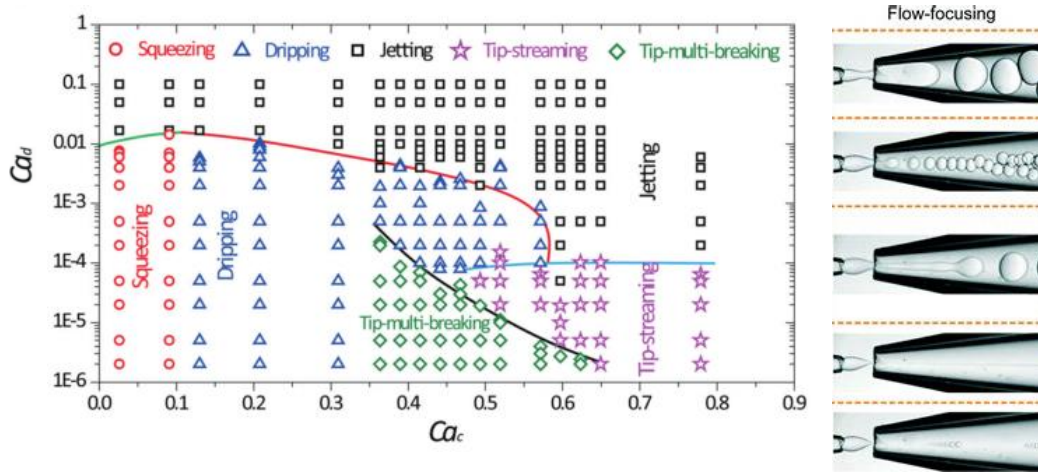


Fig. 21: example of a flow map for different droplet generation modes [3]

## 6. Droplet Size

Viscosity ratio,  $\lambda = \frac{\mu_d}{\mu_c}$ , and the ratio of the volumetric flow rates  $Q_r = \frac{Q_d}{Q_c}$  are important parameters in our study to obtain droplet size[16][25][26]. In our work we established a similar flow map to identify the size of the generated droplets as a function of flow rates and the property of the dispersed phase. Flow rate of the continuous phase  $Q_c$  was varied between 3  $\mu\text{L}/\text{min}$  to 8  $\mu\text{L}/\text{min}$  while the dispersed phase flow rate  $Q_d$  remained constant at 1  $\mu\text{L}/\text{min}$ . The fluids properties are discussed in Chapter 1.

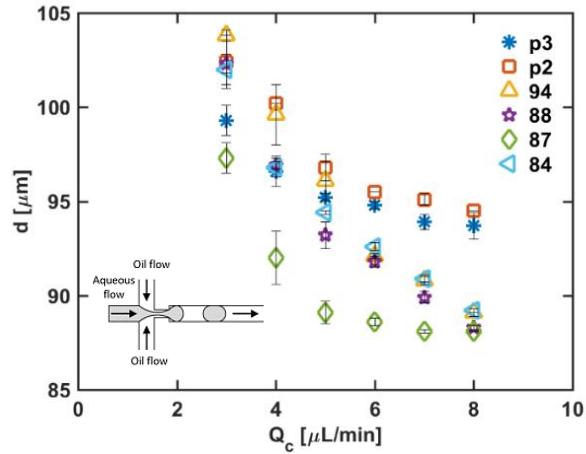


Fig. 22: droplet size as a function of flow rates for different aqueous phase fluids

### 6.1. Capillary number

Capillary number of droplet generation was varied by changing the continuous phase flow rate,  $Q_c$ . The result is shown in Fig. 23. We used the correlation from reference [16] to calculate the Capillary number. We observed that for the same set of flow rate ratios, different size droplets were generated, because of different Capillary numbers; this signifies the importance of the properties of the solutions. numbers are obtained,

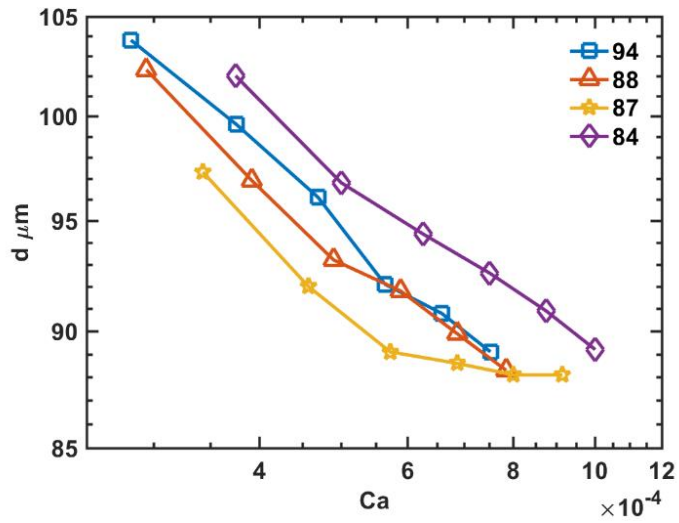


Fig. 23: Critical Capillary number as a function of droplet diameter

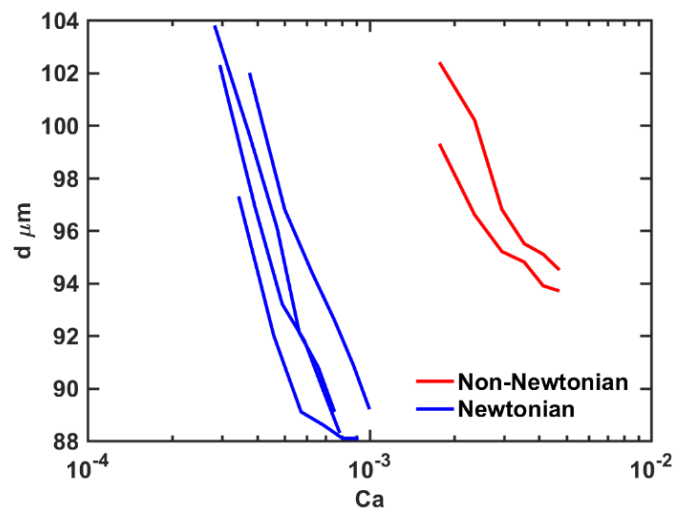


Fig. 24: Capillary number changing with  $Q_c$

However, we noticed, the correlation explained in [16] was not sufficient to describe our system and a modified Capillary number was required. Several modification could be used such as using the actual diameter of the undeformed droplet, a slight modification to the value of the average velocity, and the viscosity ratio must be incorporated in the modified correlation. We established a modified correlation for the Capillary not, however, we did not include it in this work.



Another important observation was regarding viscoelastic solutions. We believe the main parameter that causes the difference in behavior of the non-Newtonian solutions was the relaxation time of the polymer. Relaxation time in the context of droplet generation is described as the resistance to the deformation (droplet elasticity inhibits droplet deformation) required for the pinch off by the continuous phase. In the other words, an increase in the degree of viscoelasticity (increase in  $Wi$  or  $De$  number) increases the critical Capillary number of droplet generation [27]. Therefore, a Deborah number with the following form must be used, which uses a more appropriate time scale of droplet generation [2] [3] [4].

$$De = \frac{t_{polym}}{t_R} = \frac{\lambda}{\sqrt{\rho \ell^3 / \sigma}}$$

## 7. Conclusions

In this chapter, we described important parameters involved in droplet generation, and we categorized them into, geometric parameters, flow conditions, and properties of solutions. We were able to generate a flow map for the aqueous droplets used in the study, in addition to finding their corresponding Capillary number for each set of parameters. These steps were necessary to characterize performance our platform in order to generate same size droplets, for different types of solutions. As was described earlier, and we will show the results in the upcoming chapters, droplet size is one the most important parameters in migration mechanism and isolation of droplets.

## 8. References

- [1] M. Seo, C. Paquet, Z. Nie, S. Xu, and E. Kumacheva, "Microfluidic consecutive flow-focusing droplet generators," *Soft Matter*, vol. 3, no. 8, p. 986, 2007.
- [2] P. Zhu and L. Wang, "Passive and active droplet generation with microfluidics: a review," *Lab Chip*, vol. 17, no. 1, pp. 34–75, 2017.
- [3] W. Lee, L. M. Walker, and S. L. Anna, "Role of geometry and fluid properties in droplet and thread formation processes in planar flow focusing," *Phys. Fluids*, vol. 21, no. 3, 2009.
- [4] J. Husny and J. J. Cooper-White, "The effect of elasticity on drop creation in T-shaped microchannels," *J. Nonnewton. Fluid Mech.*, vol. 137, no. 1–3, pp. 121–136, 2006.
- [5] S. L. Anna and H. C. Mayer, "Microscale tipstreaming in a microfluidic flow focusing device," *Phys. Fluids*, vol. 18, no. 12, 2006.
- [6] A. Gupta and M. Sbragaglia, "Deformation and break-up of Viscoelastic Droplets Using Lattice Boltzmann Models," *Procedia IUTAM*, vol. 15, pp. 215–227, 2015.
- [7] C. Zhang and D. Van Noort, *Cells in microfluidics*, vol. 304. 2011.
- [8] D. Qi, D. J. Hoelzle, and A. C. Rowat, "Probing single cells using flow in microfluidic devices," *Eur. Phys. J. Spec. Top.*, vol. 204, no. 1, pp. 85–101, 2012.
- [9] A. J. Franck, "Normal stresses in shear flow," *TA Instruments*, vol. AN007, pp. 1–4, 2014.
- [10] F. Dutka, A. S. Opalski, and P. Garstecki, "Nano-liter droplet libraries from a pipette: step emulsificator that stabilizes droplet volume against variation in flow rate," *Lab Chip*, vol. 16, no. 11, pp. 2044–2049, 2016.
- [11] S. Mortazavi and G. Tryggvason, "A numerical study of the motion of drops in Poiseuille flow. Part 1. Lateral migration of one drop," *J. Fluid Mech.*, vol. 411, pp. 325–350, 2000.
- [12] B. H. A. Stone and B. J. B. L. G. Leal, "An Experimental Study of Transient Effects in the Breakup of Viscous Drops.PDF," pp. 131–158, 1986.
- [13] Z. Nie et al., "Emulsification in a microfluidic flow-focusing device: Effect of the viscosities of the liquids," *Microfluid. Nanofluidics*, vol. 5, no. 5, pp. 585–594, 2008.
- [14] J. Yan, W. A. C. Bauer, M. Fischlechner, F. Hollfelder, C. F. Kaminski, and W. T. S. Huck, "Monodisperse water-in-oil-in-water (W/O/W) Double emulsion droplets as uniform compartments for high-throughput analysis via flow cytometry," *Micromachines*, vol. 4, no. 4, pp. 402–413, 2013.
- [15] S.-Y. Teh, R. Lin, L.-H. Hung, and A. P. Lee, "Droplet microfluidics," *Lab Chip*, vol. 8, no. 2, p. 198, 2008.
- [16] S. L. Anna, N. Bontoux, and H. A. Stone, "Formation of dispersions using 'flow focusing' in microchannels," *Appl. Phys. Lett.*, vol. 82, no. 3, pp. 364–366, 2003.

- [17] D. Robert and D. Carlo, "Title: High-Speed Manipulation of Cells and Particles for Single-Cell Analysis and Mechanophenotyping," 2012.
- [18] E. Z. Macosko et al., "Highly parallel genome-wide expression profiling of individual cells using nanoliter droplets," *Cell*, vol. 161, no. 5, pp. 1202–1214, 2015.
- [19] A. S. Utada, A. Fernandez-Nieves, H. A. Stone, and D. A. Weitz, "Dripping to jetting transitions in coflowing liquid streams," *Phys. Rev. Lett.*, vol. 99, no. 9, pp. 1–4, 2007.
- [20] T. P. Lagus and J. F. Edd, "A review of the theory, methods and recent applications of high-throughput single-cell droplet microfluidics," *J. Phys. D. Appl. Phys.*, vol. 46, no. 11, 2013.
- [21] C. N. Baroud, F. Gallaire, and R. Dangla, "Dynamics of microfluidic droplets," *Lab Chip*, vol. 10, no. 16, p. 2032, 2010.
- [22] C. A. Stan, S. K. Y. Tang, and G. M. Whitesides, "Independent Control of Drop Size and Velocity in Microfluidic Flow-Focusing Generators Using Variable Temperature and Flow Rate," vol. 81, no. 6, pp. 2399–2402, 2009.
- [23] A. M. Pit, M. H. G. Duits, and F. Mugele, "Droplet manipulations in two phase flow microfluidics," *Micromachines*, vol. 6, no. 11, pp. 1768–1793, 2015.
- [24] T. Beatus, R. H. Bar-Ziv, and T. Tlusty, "The physics of 2D microfluidic droplet ensembles," *Phys. Rep.*, vol. 516, no. 3, pp. 103–145, 2012.
- [25] A. C. Hatch, A. Patel, N. R. Beer, and A. P. Lee, "Passive droplet sorting using viscoelastic flow focusing," *Lab Chip*, vol. 13, no. 7, p. 1308, 2013.
- [26] C. A. Stan, L. Guglielmini, A. K. Ellerbee, D. Caviezel, H. A. Stone, and G. M. Whitesides, "Sheathless hydrodynamic positioning of buoyant drops and bubbles inside microchannels," *Phys. Rev. E - Stat. Nonlinear, Soft Matter Phys.*, vol. 84, no. 3, p. 4840, 2011.
- [27] D. Zhou, P. Yue, and J. Feng, "Viscoelastic effects on drop deformation in a converging pipe flow," *J. Rheol. (N. Y. N. Y.)*, pp. 469–487, 2008.

## Chapter 5 – Migration rate of droplets in microchannels

### 1. Introduction:

High throughput screening and sorting of compartmentalized droplets are essential for a variety of biological and bio-chemical[1] applications, e.g., single cell analysis [2][3], genomics [4], and directed evolution of enzymes [5][6][7]. We described the pros and cons of the passive sorting in Chapter 1, in this chapter we aim to have a more in-depth discussion regarding this method of droplet sorting.

Passive sorting of droplets requires an understanding of different types of lift forces acting upon droplets, which indeed depend on droplet size, physical properties of continuous and disperse solutions, flow condition, and channel geometry, as were indicated in Table 1. Some of these properties, such as droplet size and mechanical properties of droplets can undergo some intrinsic changes during biological/ bio-chemical processes as illustrated in Fig. 25.

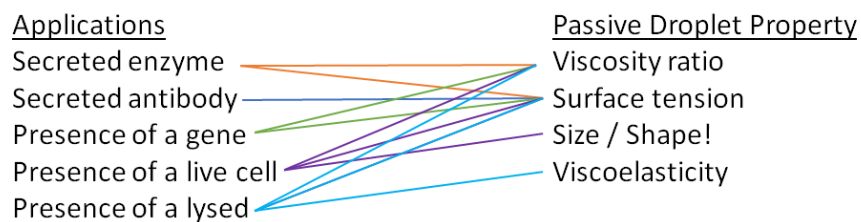


*Fig. 25: Property changes of droplets in during common biological processes*

We can categorize these properties into distinct groups and study the influence of each parameter (or a combination of parameters) on migration of droplets in microfluidics channels. Table 6 includes some of these parameters and the current sorting techniques available for each category, e.g., passive [8][9] or active sorting [5]. We focus our study in this work on the passive sorting methods.

Table 6: droplet properties

Variable type	Intrinsic droplet properties	Sorting method
Geometric	<i>size</i>	Passive – hydrodynamic / Active
Mechanical properties	<i>viscosity ratio, interfacial tension, density, viscoelasticity, and deformability</i>	Passive – hydrodynamic / Active
Other properties	optical, electrical, magnetic, acoustic, thermal	Active – varies according to the property

### 1.1. Systematic study procedure:

We laid out a systematic study to explore the effect of varying intrinsic properties of droplets on droplet trajectory and migration rates in microchannels as shown in Fig. 26. We must be considering the fact that in a multiple variable system, a change in one property might have an impact on the other properties of a substance, but not necessarily in a linear way. One example for this is the effect of temperature change in viscosity [10] and density of a substance; both density and viscosity decrease with temperature, however, viscosity has an exponential relationship, while density holds a linear relationship. This implies that changes in the properties of a system can occur at different rates, e.g., density might vary slightly with temperature, while viscosity can change rapidly [11].

The systematic study as described in Fig. 26, isolates the contribution that each intrinsic property has on migration of droplets, e.g, the viscosity ratio changes can be studied while the changes in the interfacial tension and density are controlled. The effect of viscosity ratio will be studied in this chapter.

However, most biological solutions exhibit non-Newtonian [12] behavior and the effect of viscoelasticity is shown to be essential for droplet separation. There are not many studies that have fully investigated various parameters affecting migration of non-Newtonian droplets in microfluidics channels, specifically in the moderate Reynolds number regimes [12]. The numerical simulation by [13] and experimental work by (Abe Lee, et al , Hur, et al) are to name a

few available sources[8][9]. We will investigate the viscoelastic forces in Chapter 6 and the effect of deformability on droplet migration will be discussed in Chapter 7.

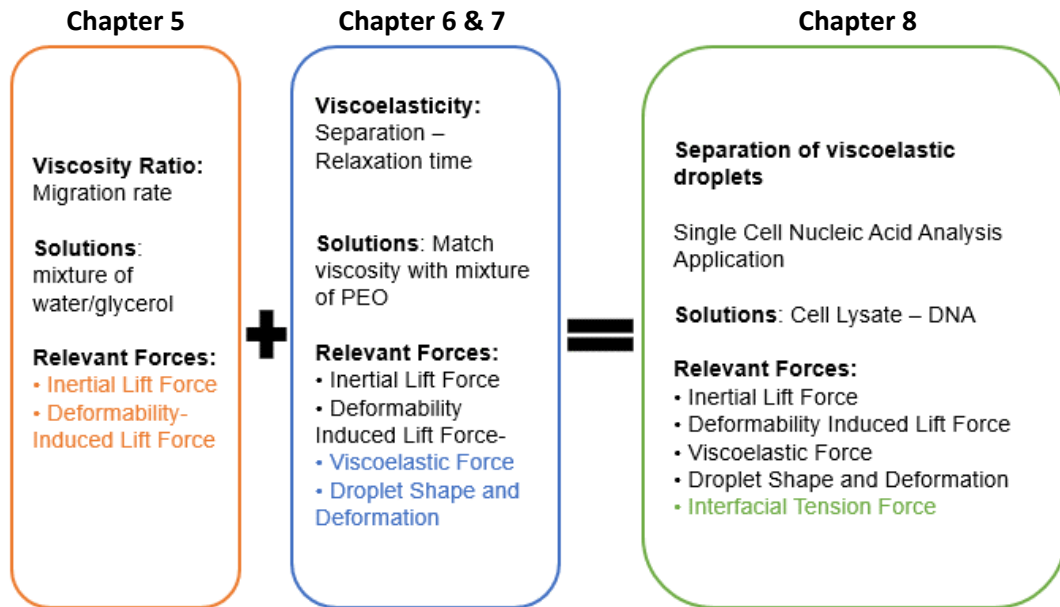


Fig. 26: Systematic study

## 2. Material

### 2.1. Effect of interfacial tension variation

Mixture of water/ glycerol with different mass fractions were used in this study. A particular advantage that water/ glycerol mixtures has is that the viscosity ratio changes across different mixtures is significantly larger than the changes in the interfacial tension [14][15][16]. Therefore, it is reasonable to assume that the changes in the interfacial tension stay relatively constant, allowing to study the effect of viscosity ratio by itself.

Table 7: Dynamic viscosities, density and viscosity ratio of the materials considered in the present study

Solution (% Wt)	Dynamic Viscosity $\eta_{avg}$ (Pa s)	Density $\rho$ ( $\frac{g}{cm^3}$ ) @ 20°C	Viscosity Ratio $k = \frac{\mu_d}{\mu_c}$
Novec 7500	0.00124	1.610	-
Water/ glycerol mixtures	1.0156	1.261	819.06
$x_g = 100$	0.0958	1.222	77.27
$x_g = 85$	0.0557	1.209	44.92
$x_g = 80$	0.0335	1.195	27.05
$x_g = 75$	0.0209	1.181	16.82
$x_g = 70$	0.0150	1.168	12.06
$x_g = 65$	0.0075	1.140	6.04
$x_g = 55$	0.0056	1.124	4.55
$x_g = 50$			

$x_g$  = mass fraction of glycerol.

## 2.2. Effect of density variation

Reference [13] numerically investigated the effect of density for both low and moderate Reynold number regimes. Based on their simulations, for small flow inertia, density does not play a significant role in the drop migration. However, for a case with a high flow inertia ( $Re_d = 37$ ), they observed some small influences as the density increases, but they concluded that the effect of viscosity ratio is more significant [13]. It is worth noting that, the density ratio used in their simulation was more than twice of the density ratio in our experiment; density ratio of the mixtures used in our work could range from 0.69 to 0.78, versus the density ratio of 2 used in their simulation. Also, the flow inertia in our experimental study ( $Re_d \sim 0.6$ ) was smaller than their flow condition. The ratio of droplet diameter to channel height in their work was much smaller than ours, in which, it could explain the effect of the density ratio they observed in their simulation. The density changes in our experiment was less than 0.09 for the most extreme mixtures (e.g. water/ glycerol with  $x_g = 50\%$  and  $x_g = 100\%$ ), thus, it is a very reasonable assumption to exclude the impact of density ratio in this study. Fig. 27 shows that the changes

in viscosity ratio is much more significant than the variation in interfacial tension and density.

The data presented in Fig. 27 were measured as described in Chapter 2.

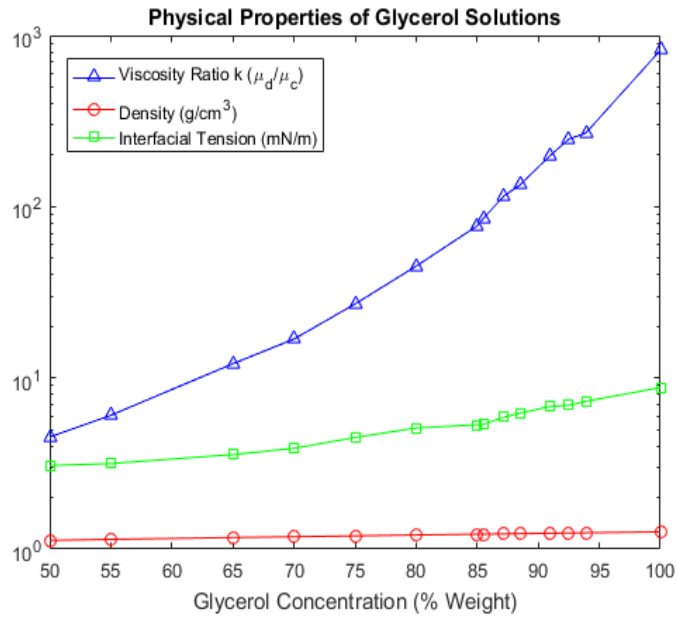


Fig. 27: Comparison of interfacial tension and density changes with viscosity ratio variations

### 3. Experimental set up

We used an integrated device in this study in which the details were provided in Chapter

3. The schematic of the device is shown in Fig. 28 for reference.



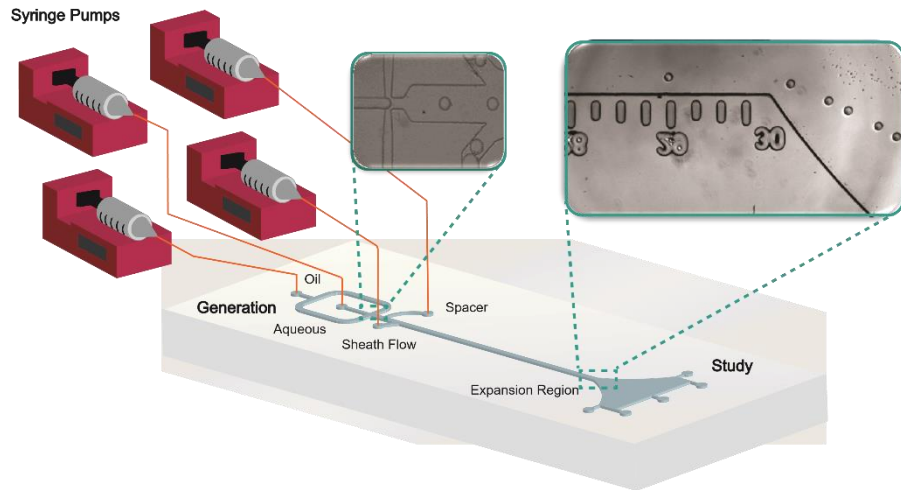


*Fig. 28: schematic of our integrated platform*

Even though the system consists of two sections: upstream droplet generation and downstream droplet separation, integrated in a continuous platform, we focus our study on the analysis of droplets in the downstream, where the migration of droplets in a straight rectangular channel is studied.

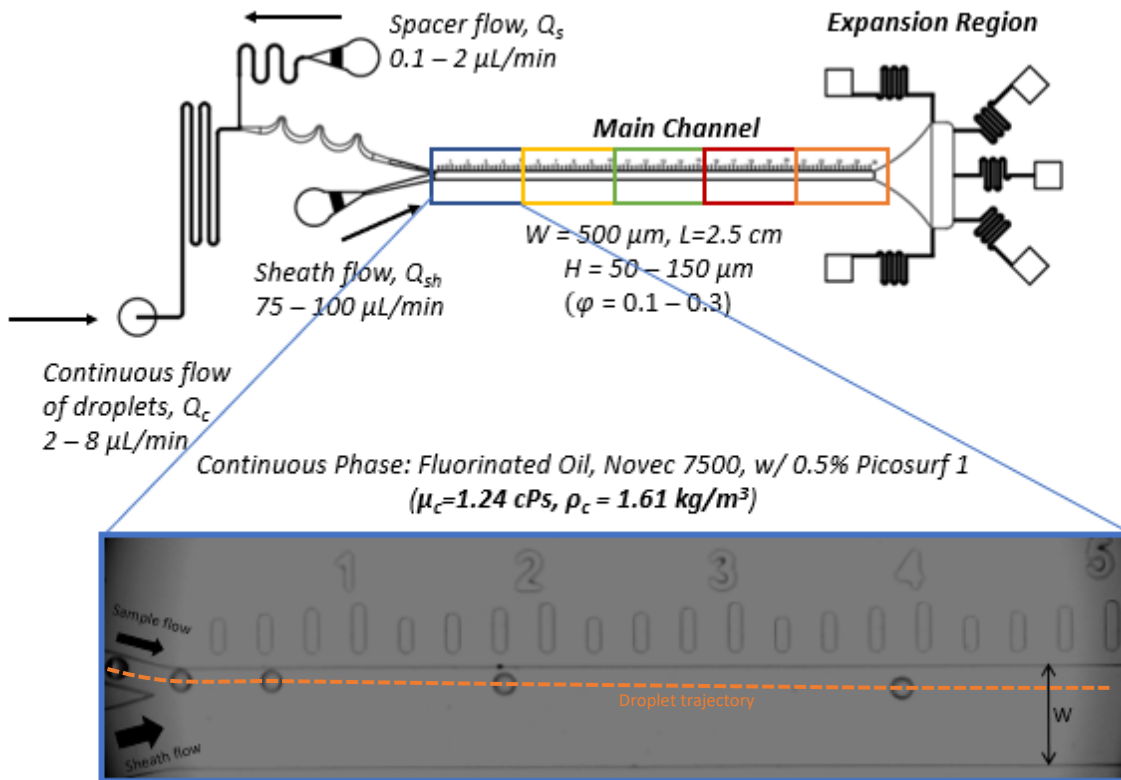


Fig. 29: schematic of an integrated device for sorting – and trajectory and equilibrium position of droplets

### 3.1. System performance:

The schematics of the downstream of the experimental setup in this study is shown in Fig. 29. The downstream section of the device consists of a straight channel with a rectangular cross section ( $W=500\ \mu\text{m}$ ,  $H=150\ \mu\text{m}$  and  $L=2.5\ \text{cm}$ ), and a gradually expanding region downstream with 5 outlets. The straight channel in the schematic is segmented into five equally long sections of  $500\ \mu\text{m}$  each, shown with distinct colors for each segment. We will use the color coded sections later for the study of the migration rate in the main channel. The expansion region is designed to maintain droplets in their focusing streamlines, allowing for an enhancement in the separation distance between droplets, where the droplets can be directed to multiple collection outlets.

Before the main channel, the design of the device includes a side channel, referred to as a “spacer” flow, positioned in between the upstream droplet generator and the downstream straight channel. In this setup, droplets are continuously being generated in an immiscible carrier fluid, Novec 7500 with 0.5% Picosurf, and transported downstream for analysis and separation.

The “spacer” flow, with a flow rate,  $Q_s$  ( $\mu\text{L}/\text{min}$ ) is an essential component in our design and plays a crucial role in the operation of our system throughout this study. It is designed to perform multiple purposes depending on the operation of the system: a) the main use of the “spacer” in our platform was to modulate the flow rate ratio between the upstream and downstream while maintaining the same flow in the main channel, b) also, it was used to maintain the same Capillary number when different aqueous solutions were used to generate droplets; the continuous phase of the droplet generator needed to be adjusted according to the properties of each aqueous solution, c) it was also used to pump additional fluids in order to increase the flow rate of the carrier fluids in the main channel, and d) was used to introduce a perpendicular flow to the main flow stream in order to space out the droplets to avoid droplet-droplet interactions before they enter the main channel.

Other parameters of the system that influence the trajectory of the droplet include droplet starting position, and flow rate of the carrier fluid [8].

### 3.2. Starting position

The starting position of droplets is shown to influence the droplet migration [8]. The sheath stream with flow rate,  $Q_{sh}$  ( $\mu\text{L}/\text{min}$ ) is used to enforce the droplet to have the same starting position at the beginning of the straight channel. The droplet position at any given time was obtained by measuring the distance,  $y$ , between droplet centroid and the channel wall. The

time lapse of the droplet position is used to obtain a complete droplet trajectory along the channel in the direction of the flow (Fig. 29).

### 3.3. Flow rate ratio

The platform used in this study is continuously transport the generated droplets to the downstream with a flow rate,  $Q_c$  ( $\mu\text{L}/\text{min}$ ), before the “spacer” flow rate increases the flow rate of the sample stream by  $Q_s$  ( $\mu\text{L}/\text{min}$ ). Then after, droplets experience a significant increase in the flow from the “sheath” stream,  $Q_{sh}$  ( $\mu\text{L}/\text{min}$ ), right at the beginning of the straight channel. An appropriate flow rate ratio is required to characterize the flow of the droplets in the straight channel. We defined two different flow rate ratios as follow: a) the ratio between upstream ( $Q_c$ ) and downstream ( $Q_s + Q_{sh}$ ) flow rates, denoted as,  $Q_{c/(s+sh)} = \frac{Q_c}{Q_s + Q_{sh}}$ , and b) the ratio between the spacer  $Q_s$  and the sheath flow, denoted as,  $Q_{s/sh} = \frac{Q_s}{Q_{sh}}$ .

### 3.4. Flow simulation

Due to the complexity of the multiple flow streams, i.e.,  $Q_c$ ,  $Q_s$ , and  $Q_{sh}$  merging at different positions in the channel, and the gradual change in the channel geometry in the expansion region, we performed a numerical simulation using COMSOL to gain a better understanding of the flow behavior within the channel. Droplets are forced to be at the wall once they enter the straight channel – this is done with an aid of the relatively large flow rate of the sheath flow compare with the sample stream ( $Q_{sh} \geq 10 (Q_c + Q_s)$ ). The flow field is still developing at the beginning of the channel, where the upstream sample flow carrying droplets ( $Q_c + Q_s$ ), merges with the sheath flow ( $Q_{sh}$ ). This is shown as Sec I in Fig. 29. The complex flow field in the entry developing region (Sec I) prevented us from accurately calculating the shear rate analytically, however, numerical simulation enabled us to quantify the shear rate in the entry region. As it pointed with an arrow in Fig. 29, the entry length in which the flow

becomes fully developed is less than 0.45 mm ( $< 2.5\%$  of the total channel length) for all the flow conditions used in this study. Therefore, it's a good assumption to neglect the effect of developing flow regime in this study.

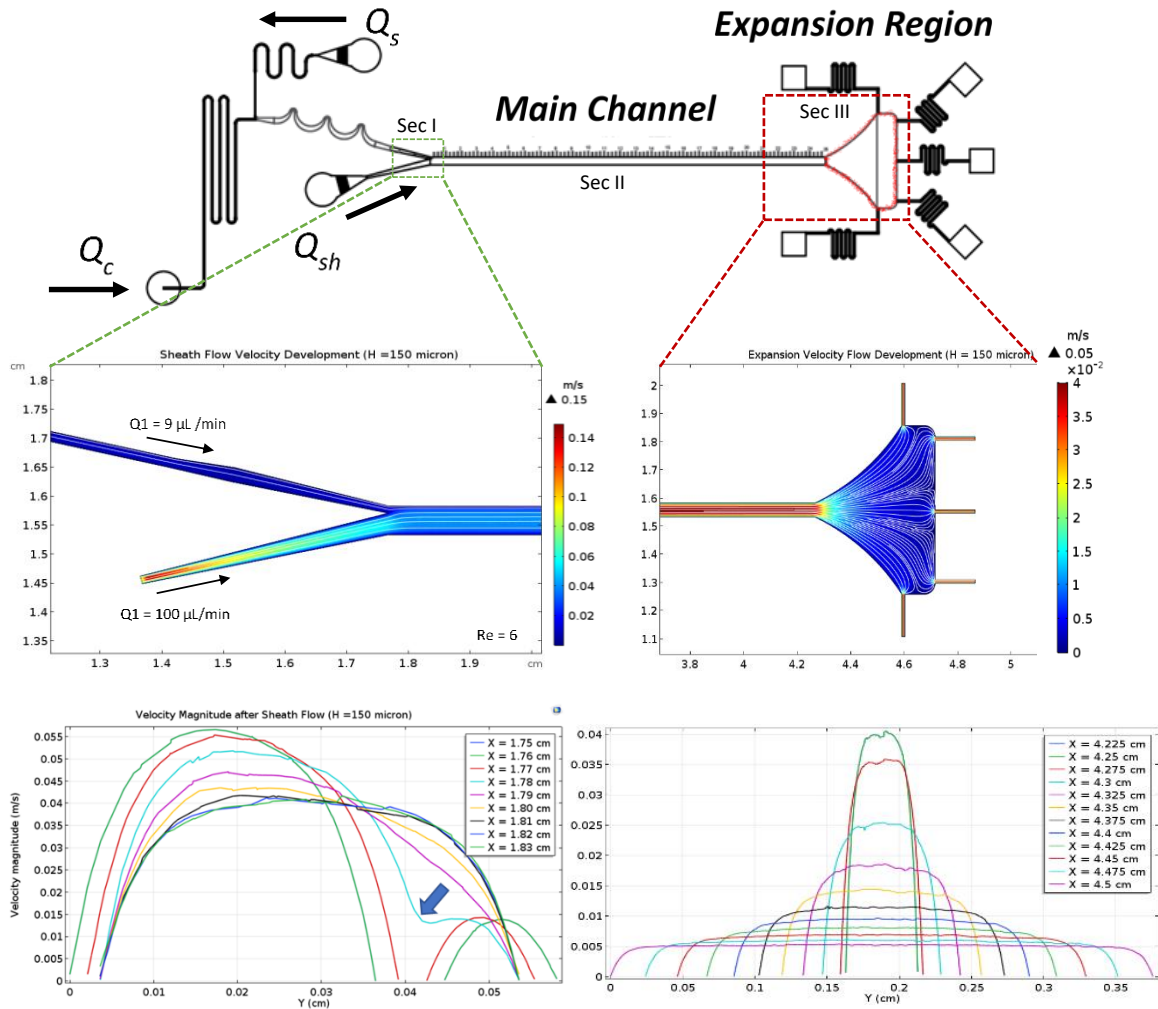


Fig. 30: COMSOL simulation of flow in different sections of the channel – Sec I: developing flow and droplets are located close to the wall, Sec II: Fully developed flow and lateral migration of droplets, Sec III: Sudden decrease in velocity in the expansion region where droplets separation occurs

#### 4. Migration rate

In the experimental work by Hatch et al, viscous droplets mostly migrated towards the channel centerline regardless of their viscosity ratio [8]. However, their migration rate of droplets

may vary depending on the size and the viscosity ratio. Rather than studying the trajectory and the equilibrium position of droplets with various viscosity ratio, we decided to investigate the migration rate instead. Migration rate is defined as the lateral displacement as a function of time. The migration rate of one set of aqueous droplets, in this case the glycerol/water solution 55% wt with viscosity ratio,  $k = 6.04$ , is presented in Fig. 31.

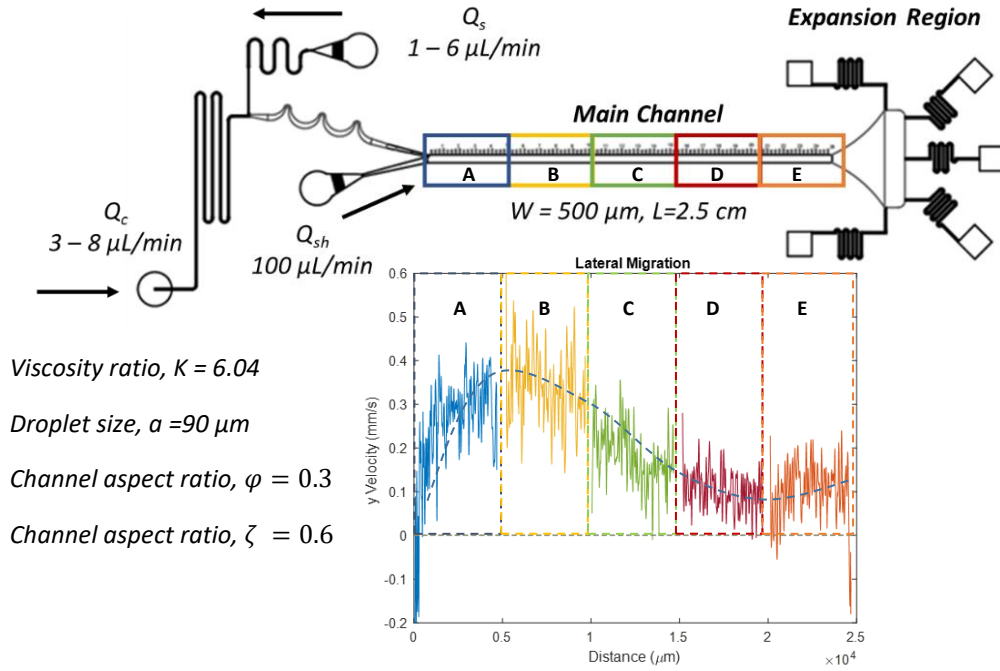


Fig. 31: Migration rate for the entire main channel. Each color represents one section, e.g., Section A is the beginning of the main channel and Section E is the last section of the channel before the expansion region

We calculated the average migration rate of droplets perpendicular to the flow direction in the main channel (in each section). At the beginning of the channel, so called Section A, droplets are positioned close to the wall because of the sheath flow, therefore they experience a large inertial wall lift force pushing them away from the wall. The wall-induced lift force of the inertial lift is the dominating force in this section, until it reaches a maximum, where it starts to decay. The influence of the lift force induced by the gradient of the velocity across the droplet (shear-gradient lift force) becomes more apparent as the droplet migrates towards the channel

centerline. There are other forces acting on droplets, but we expect the inertial force be the main contributor to the force balance.

#### 4.1. Slip velocity

We also obtained the slip velocity of the droplet (the difference between average velocity of the channel and the droplet velocity) which shows that droplets lag behind the undisturbed flow in their surroundings. The magnitude of the axial velocity of the droplet and the average channel velocity is shown in Fig. 32.

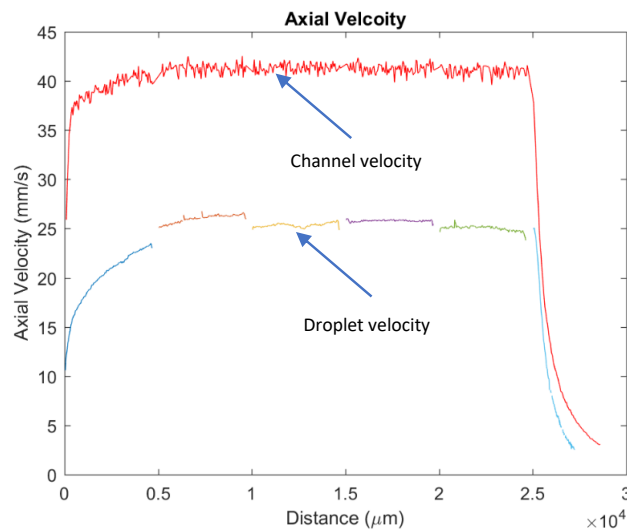


Fig. 32: Slip velocity of droplets

#### 4.2. Effect of droplet size

Previous studies have demonstrated efficient hydrodynamic separation of droplets based on size. It is shown that larger droplets experience larger lift forces towards channel center. This technique could be useful for applications where there is a large population of polydisperse droplets in which droplets can be differentiated from each other by their distinct

size. However, microfluidics is often used to generate monodisperse droplets, with a small variation in size, which makes the size-based separation ineffective. Therefore, the ability to sort droplets with more than one intrinsic property, besides droplet size, is desired in many applications in chemistry and biology. In this study, we focus on the contribution of some of the mechanical properties listed in Table 6, including: viscosity ratio, viscoelasticity, and interfacial tensions of droplets.

### 4.3. Effect of viscosity ratio

The effect of viscosity ratio on migration of droplets was studied in previous work, however, to the best of our knowledge, most of the experimental work were done in low Reynolds regimes, where the inertial effects are negligible, and the droplet deformation causes the droplets to migrate towards low shear rate regions [17] [9] [8]. However, the inertial effects were numerically simulated for a wide range of Reynolds numbers by Mortazavi, et al. [13].

## 5. Scaling analysis

### 5.1. Deformability-induced lift force

Theoretical work by Chan and Leal was the first study to investigate the impact of viscosity ratio on lateral migration of droplets. They proposed that migration rate is a function of viscosity ratio ( $k = \frac{\mu_d}{\mu_c}$ ). Chan and Leal predicted that the droplets migrate towards the low shear rate region (channel center) for most viscosity ratios, and for a viscosity ratio between  $0.5 < k < 10$ , the direction of the lateral migration changes and droplets migrate towards high shear (channel wall). The magnitude of the lateral migration is a function of droplet size,  $a$ , the characteristic length,  $d$ , droplet location from the wall,  $y$ , maximum fluid velocity in Poiseuille flow,  $V_m \sim (3/2) V_{avg}$ , viscosity of the continuous phase,  $\mu_0$ , and the interfacial tension,  $\gamma$ . The



starting position of droplets,  $y$ , is also an important parameter as droplets that are closer to the wall experience a larger lateral migration force. Hatch et al, derived the following correlation to find the magnitude of the migration velocity.

$$\mu_m = 16\alpha C a_p \left( Vm \frac{a}{w} \right) \left( \frac{a}{w} \right) \left( 1 - \frac{2y}{w} \right)$$

The dependence of migration to the viscosity ratio,  $k$ , is presented in as  $\alpha$ . The inversion in droplet migration direction occurs when  $\alpha$  becomes negative, between the viscosity ratio  $0.5 < k < 10$  (Fig. 33). In this case, droplet migrates towards high shear gradient region.

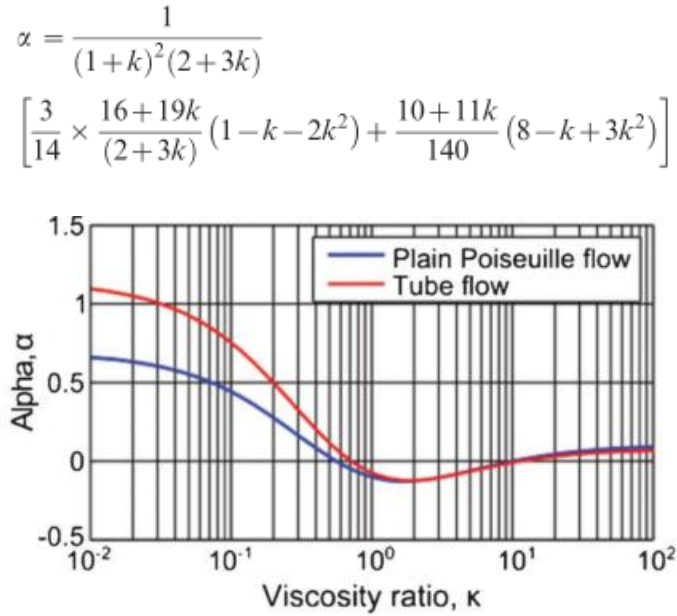


Fig. 33: viscosity ratio dependence of Alpha [Hatch et al. 2013]

Similarly, Stan et al, derived the following correlation for the magnitude of the lift force.

$$F_{L,deformation} = \mu_o V_m a C a_p \left( \frac{a}{w} \right) \frac{y}{w} f(k)$$

Where  $f(k)$  is a function of viscosity ratio and is defined very similar to  $\alpha$ .

$$f(k) = \frac{128\pi}{(k+1)^3} \left( \frac{11k+10}{140} (3k^2 - k + 8) + \frac{3}{14} \frac{19k+16}{3k+2} (2k^2 - k - 1) \right)$$

Hur et al, studied the effect of viscosity ratio on the equilibrium position of elastic particles and silicone oil droplets in water, in a high channel aspect ratio channel ( $\varphi = H/W \approx 2$ ). They observed that the droplets migrated towards the centerline, and the droplets moved closer to the centerline as the as the viscosity ratio decreased. A shift in the direction of the lateral migration lift force occurred for droplets with  $k < 4.6$ , where droplets migrated away from the center, in an agreement with Chan and Leal predictions [17]. In a numerical study done by Mortazavi and et al, they performed simulations on droplets with different viscosity ratio and their result was in agreement with Chan and Leal predictions, within the limitations of their theoretical work. Mortazavi argued that the reason for the bi-directional migration behavior of droplets approaching the lower limit of viscosity ratio as it was proposed by Chan and Leal, is the thickness of the lubrication layer. Since the higher viscosity droplet, (i.e.,  $k = 8$  in their simulation) more effectively slows down the surrounding flow, therefore, the lower viscosity droplets (i.e.,  $k = 2$  in their simulation) would have a thinner lubrication layer between the droplet and the wall, which results in a smaller distance from the channel wall [13].

The theoretical prediction of Chan and Leal was limited to small droplet size, small droplet deformation, and it is not clear how they counted for the confinement of the channel [13]. The numerical simulation of [13] expanded the limitations of [17] and in their work they performed simulations of the lateral migration of droplets with different viscosity ratio, size, deformability, and flow rates. Their simulation was in agreement with [17] prediction, within the limitations of the theoretical work. They concluded that, large droplets with a diameter comparable to the channel height migrate to the center of the channel regardless of the viscosity ratio, unlike the smaller drops. Their simulation result could explain the experimental result of [8]. In a more recent study, [8] showed that Newtonian droplets migrate towards the channel centerline, regardless of their viscosity ratio. The migration rate, however, might vary with the viscosity ratio. However, they showed that non-Newtonian droplets behave differently

than Newtonian drops. It is unclear if the question proposed by [17] takes into an account the non-Newtonian behavior of fluids and the dependence of the viscosity to the shear rate [8]. The deviations of [8] and [13] from [17] prediction could be related to the droplet size, deformation, channel confinement, and the Newtonian characteristics of the equation.

In the absence of fluid inertia, nonlinearity introduced by deformation is the only means of lateral migration in the limit of low Reynolds number for spherical particles [13]. The viscous forces are important, and the appropriate dimensionless number is Capillary number (ratio of viscous forces to interfacial tension forces). Droplets with lower viscosity ratio are more deformable. They also exhibit a more deformed shape near the wall because of shear stress differences as a function of position, and this could contribute to the faster migration rate of more deformable droplets towards the centerline [9] [13]. They also exhibit a slightly higher axial velocity than less deformable droplets. Larger droplets disturb the flow more and they migrate to the center of channel at a higher rate [13].

As the Re number increases, droplets enter an inertial regime. Contribution of fluid inertia impacts the droplet deformability and migration. The ratio of the inertial forces to interfacial tension forces determines the droplet deformability. This ratio is called Weber number. Deformability increases with an increase in Weber number and the equilibrium position of more deformable droplets is closer to the channel centerline. In the limit of moderate Reynolds number, the major axis of the deformable droplet is oriented about 45 degrees with respect to channel wall. As the deformability of droplet increases the major axis becomes more aligned to the flow direction. As the drop becomes more deformable, its cross section becomes thinner, making the velocity difference across the drop smaller. This weakens the shear-gradient lift force pushing the droplets away from the center [13]. A more deformed droplet exhibits lower resistance to the flow, due to the smaller drag force. This results in a higher axial velocity. The

combination of higher axial velocity of the more deformed droplet, weaker shear gradient force pushing it away from the center causes the more deformable drop to migrate faster to the channel center [13]. In addition, deformable droplets close to the wall experience more deformation. The elongated droplet located along the wall creates a longer gap between droplet and wall. This could result in larger repulsive lubrication force that aids in pushing the droplet away from the wall. Mortazavi defined slip velocity as the drop velocity minus undisturbed flow velocity. Particles and droplets always lag behind the undisturbed flow and have a negative slip velocity. Slip velocity will be lowest for the most deformable drop. The negative slip velocity and the curvature of the velocity profile generate a force that drives the particle/ droplet away from the center of the channel [13]. This is referred to as the shear gradient lift force. More viscous droplets lag the surrounding flow more. This results in an increase in viscous forces in the lubrication layer, (viscous blocking - lubrication force - wall repulsion). This effect is similar to rotating solid particles where as they are closer to the wall the sphere is inhibited from rotating [13]. Increasing Reynolds number, reduces the viscous effects present near the wall. The lubrication force decreases, resulting in a smaller force pushing droplet away from the wall. Large droplets with a diameter comparable to the channel height always migrate to the channel centerline regardless of Reynolds number. It is also observed that at higher Reynolds numbers droplets undergo some oscillatory motion before they stabilize in their steady equilibrium positions. The amplitude of the oscillatory motion increases with Re number and the oscillation damps with a decrease in viscosity ratio. They concluded that unlike in lower Reynolds number where deformability drives the droplet to the equilibrium position, at high Re, inertia has the most significant contribution to the lateral migration [13]. The recent work by Hatch et al, showed that viscoelastic droplets migrate towards the channel wall with the magnitude directly related to the degree of viscoelasticity. Droplets with weak viscoelastic properties were close to the centerline, but slightly off-centered, because of the insufficient viscoelastic-induced lift force, whereas, strong viscoelastic droplets migrated near the wall [8]. A complete understanding of

underlying physics behind lateral migration of viscoelastic droplets is needed. Further investigation is then required to better understand the impact of viscoelasticity of the migration of droplets. We will discuss these in depth in Chapter 6 and 7.

## 5.2. Inertial effect on migration

Inertial flow results in additional lift forces on the droplets. In this section we seek to exploit the inertial effects that influence the migration of droplets for droplets with various viscosity ratio  $k = \frac{\mu_d}{\mu_c}$ .

We calculated the migration rates of droplets of various viscosity ratios from our experiment and compared the values with the deformability-induced lift force correlation, for the entire length of our channel. We observed that the effect of inertia has amplified the migration rates, as it was expected. We deduce this because the magnitude of the lateral migration of droplet in our system significantly deviated from the deformability-induced lift force correlations (Fig. 34).

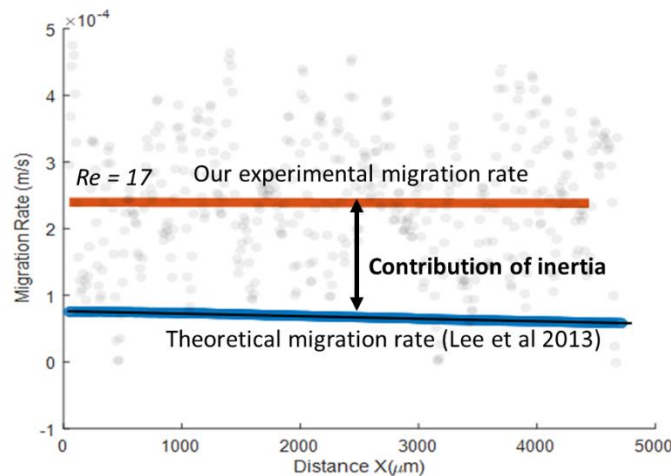


Fig. 34: contribution of inertia on migration rate

We proposed a correlation to predict the migration rates, which takes into an account the effect of inertia through Weber number.

$$We_P = \frac{\rho V_{avg}^2}{\sigma} \left(\frac{a}{W}\right)^2, We = Re \cdot Cap$$

$$\text{Migration rate } \left(\frac{m}{s}\right) \cong C_0 We \left[ Vm \left(\frac{a}{W}\right) \right] \left\{ \left(\frac{a}{W}\right) \right\} \left\{ \left(1 - \frac{2y}{W}\right) \right\}$$

In order to find the constant  $C_0$ , we curve fitted all the migration rate data from our experiment into our proposed correlation. The result is presented in Fig. 35 for each section of the channel.

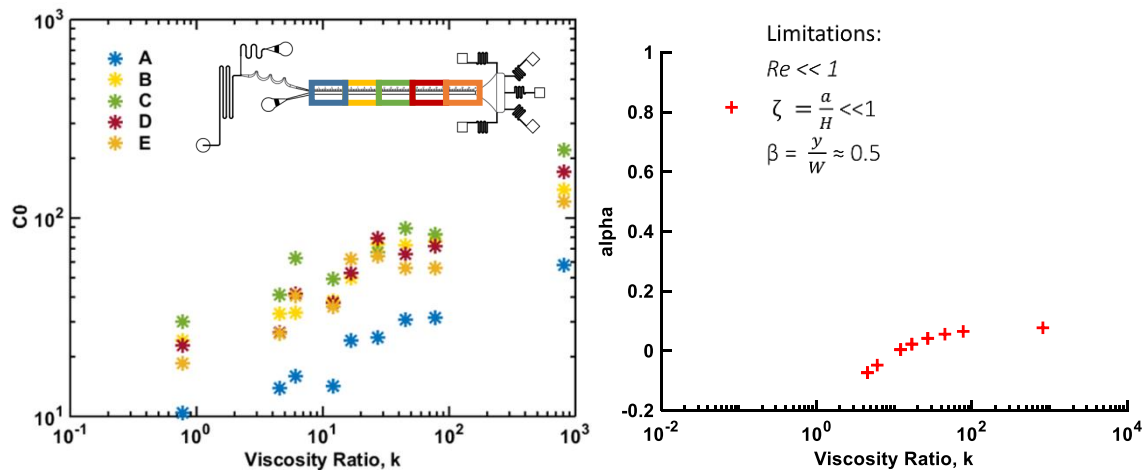


Fig. 35:  $C_0$  dependence on viscosity ratio

The correlation in Fig. 35 follows the same trend as the  $\alpha$ -correlation proposed by (Hatch et al 2013). It addresses the shortcoming of the previous correlations: a) it covers a wide range of Reynolds number in an inertial regime, b) it can be used for different size droplets, and c) this correlation is taking into an account the effect of channel wall in which the droplets can be located anywhere in the channel, yet this correlation can predict the migration rate. With the same analogy we can obtain a correlation for Inertial Lift force proposed by Stan. et, al. in the inertial regime.

$$FL \left(\frac{Kg m}{s^2}\right) \cong C1 \mu_0 Vm a We \left(\frac{a}{W}\right)^2 \left(1 - \frac{2y}{W}\right)$$

## 6. Conclusions

In this chapter we were able to isolate the effect of viscosity ratio in migration rate of droplets. A new correlation for the migration rate in the inertial regime was proposed in which did not have the droplet size ratio and the droplet position limitations. We expanded our correlation to predict the inertial lift forces on the droplets of varying viscosity ratio in microchannels.

## 7. References

- [1] F. Dutka, A. S. Opalski, and P. Garstecki, "Nano-liter droplet libraries from a pipette: step emulsificator that stabilizes droplet volume against variation in flow rate," *Lab Chip*, vol. 16, no. 11, pp. 2044–2049, 2016.
- [2] C. Zhang and D. Van Noort, *Cells in microfluidics*, vol. 304. 2011.
- [3] S. W. Lim, T. M. Tran, and A. R. Abate, "PCR-activated cell sorting for cultivation-free enrichment and sequencing of rare microbes," *PLoS One*, vol. 10, no. 1, pp. 1–16, 2015.
- [4] A. Didelot et al., "Multiplex picoliter-droplet digital PCR for quantitative assessment of DNA integrity in clinical samples," *Clin. Chem.*, vol. 59, no. 5, pp. 815–823, 2013.
- [5] S.-Y. Teh, R. Lin, L.-H. Hung, and A. P. Lee, "Droplet microfluidics," *Lab Chip*, vol. 8, no. 2, p. 198, 2008.
- [6] D. Qi, D. J. Hoelzle, and A. C. Rowat, "Probing single cells using flow in microfluidic devices," *Eur. Phys. J. Spec. Top.*, vol. 204, no. 1, pp. 85–101, 2012.
- [7] J. Yan, W. A. C. Bauer, M. Fischlechner, F. Hollfelder, C. F. Kaminski, and W. T. S. Huck, "Monodisperse water-in-oil-in-water (W/O/W) Double emulsion droplets as uniform compartments for high-throughput analysis via flow cytometry," *Micromachines*, vol. 4, no. 4, pp. 402–413, 2013.
- [8] A. C. Hatch, A. Patel, N. R. Beer, and A. P. Lee, "Passive droplet sorting using viscoelastic flow focusing," *Lab Chip*, vol. 13, no. 7, p. 1308, 2013.
- [9] S. C. Hur, N. K. Henderson-MacLennan, E. R. B. McCabe, and D. Di Carlo, "Deformability-based cell classification and enrichment using inertial microfluidics," *Lab Chip*, vol. 11, no. 5, p. 912, 2011.
- [10] Dow, "Density of Glycerine-Water Solutions," Edge, p. 99800.

- [11] K. Sarkar, "Deformation and breakup of a viscoelastic drop in a Newtonian matrix under steady shear," *J. Fluid Mech*, vol. 584, pp. 1–21, 2017.
- [12] D. Zhou, P. Yue, and J. Feng, "Viscoelastic effects on drop deformation in a converging pipe flow," *J. Rheol. (N. Y. N. Y.)*, pp. 469–487, 2008.
- [13] S. Mortazavi and G. Tryggvason, "A numerical study of the motion of drops in Poiseuille flow. Part 1. Lateral migration of one drop," *J. Fluid Mech.*, vol. 411, pp. 325–350, 2000.
- [14] S. L. Anna and H. C. Mayer, "Microscale tipstreaming in a microfluidic flow focusing device," *Phys. Fluids*, vol. 18, no. 12, 2006.
- [15] X. Bin Li, F. C. Li, H. Kinoshita, M. Oishi, and M. Oshima, "Dynamics of viscoelastic fluid droplet under very low interfacial tension in a serpentine T-junction microchannel," *Microfluid. Nanofluidics*, vol. 18, no. 5–6, pp. 1007–1021, 2015.
- [16] M. Seo, C. Paquet, Z. Nie, S. Xu, and E. Kumacheva, "Microfluidic consecutive flow-focusing droplet generators," *Soft Matter*, vol. 3, no. 8, p. 986, 2007.
- [17] P. C. H. Chan and L. G. Leal, "The motion of a deformable drop in a second-order fluid," *J. Fluid Mech.*, vol. 92, no. 1, pp. 131–170, 1979.
- [18] C. A. Stan, L. Guglielmini, A. K. Ellerbee, D. Caviezel, H. A. Stone, and G. M. Whitesides, "Sheathless hydrodynamic positioning of buoyant drops and bubbles inside microchannels," *Phys. Rev. E - Stat. Nonlinear, Soft Matter Phys.*, vol. 84, no. 3, p. 4840, 2011.



## Chapter 6: Passive separation of viscoelastic droplets

### 1. Viscoelasticity-based separation

In this chapter we demonstrate viscoelastic based separation of droplets in our platform, and we quantify the viscoelastic properties based on appropriate non-dimensional numbers. The proposed deformability-induced lift force by Chan and Leal [12] does not address the impact of viscoelasticity of non-Newtonian droplets on droplet migration. There is no indication of a shear rate dependence of the fluid viscosity in previously developed analyses. As noted earlier, it is limited to small droplet size, small deformability (low  $Ca$ ), low Reynolds number regime, and it does not take into an account the effect of wall on droplets' behavior.

There are limited resources available in the current literature that have studied the migration of viscoelastic droplets. Hur et al obtained the equilibrium position of PDMS particles with various elasticities (0.5-100 kPa) to be closer to the centerline than viscous (Newtonian) droplets, indicating the direction of elasticity-induced lift force towards the center (they referred to this force as “viscoelasticity-induced lift force”) [9]. Viscoelastic droplets would have a different force balance mechanism than the elastic rigid particles. We can point out to the experimental work by Hatch et al [5] as one of the very few studies available on migration of viscoelastic droplets. Hatch et al demonstrated that viscoelastic droplets migrated towards the channel for a combination of device designs including straight channel, gradual widening of the straight channel, and spiral [5]. They were able to distinguishable a difference between the equilibrium position of Newtonian and non-Newtonian droplets.

## 2. Material

The systematic approach in this chapter is to isolate the contribution of viscoelasticity on the lateral migration of droplets. A list of solutions used in this study are shown in Table 8 (Newtonian) and Table 9 (No-Newtonian).

The goal for this study was to choose Newtonian solutions that have a similar viscosity to of PEO solutions. With that we could explore the influence of only viscoelasticity on droplet migration.

*Table 8: Newtonian Liquids*

Solution (% Wt)	Dynamic Viscosity $\eta_{avg}$ (Pa s)	Density $\rho$ ( $\frac{g}{cm^3}$ ) @ 20°C	Viscosity Ratio $k = \frac{\mu_d}{\mu_c}$
Novec 7500	0.00124	1.610	-
Water/ glycerol mixtures	$x_g = 100$	1.0156	819.06
	$x_g = 93.9$	0.3343	269.63
	$x_g = 92.5$	0.3079	248.29
	$x_g = 90.9$	0.2436	196.48
	$x_g = 88.5$	0.1661	133.96
	$x_g = 87.2$	0.1434	115.63
	$x_g = 85.5$	0.1056	85.12

*Table 9: Non-Newtonian Liquids*

Solution (% Wt)	Dynamic Viscosity $\eta_{avg}$ (Pa s) Shear rate: 1 – 500 (1/s)	Density $\rho$ ( $\frac{g}{cm^3}$ ) @ 20°C	Viscosity Ratio $k = \frac{\mu_d}{\mu_c}$ Shear rate: 1 – 500 (1/s)
Water/ PEO	$x_g = 3$	1.26	1626 - 225
	$x_g = 2$	1.23	322 - 93

Fig. 36 shows our viscosity measurement of selected solutions within the shear rate range investigated in this study ( $1 - 500 \text{ s}^{-1}$ ). By a quick comparison between viscous solutions denoted as: g85, g88, and g 94, corresponding to the water/ glycerol mixtures with 85%, 88%,

and 94% glycerol, and the polymer solutions denoted as: p2 and p3 corresponding to 2% and 3% of MW =  $1 \times 10^6$  g/mol<sup>-1</sup> PEO mixtures, it is apparent that the PEO solutions exhibit shear thinning behavior which increases with shear rate. The larger the molecular weight of the polymer or the larger the percentage of the mixture, the greater the shear thinning behavior that the polymer exhibits.

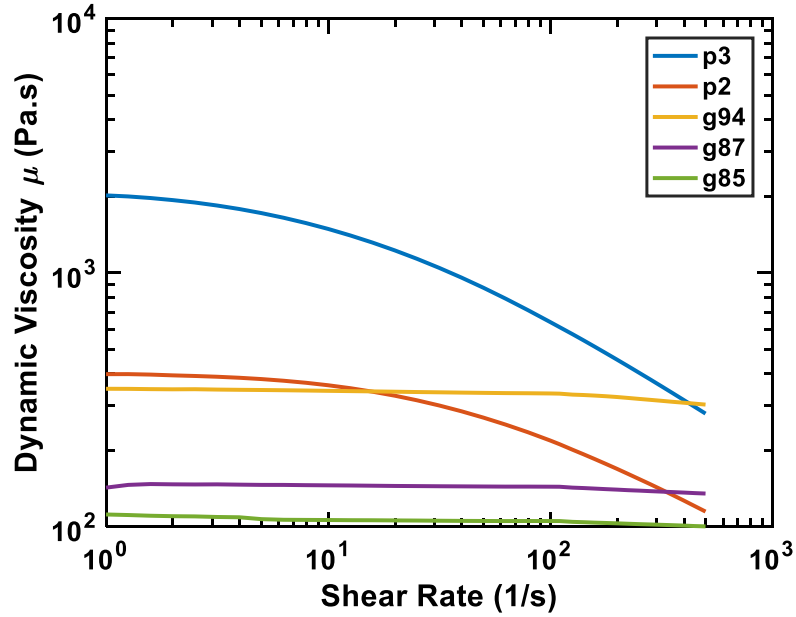


Fig. 36: Shear-rate dependence of viscosity of PEO (non-Newtonian) solutions compared with the selected Newtonian solutions of glycerol/ water mixtures from Table 8

The shear thinning behavior of PEO solutions exhibits power law relations [16]. The viscoelasticity of the solutions is characterized in Table 9, and the corresponding relaxation times are calculated based on Cross Model as shown in Table 10.

Table 10: Relaxation Time - Cross Model Validation

$\frac{\eta - \eta_{\infty}}{\eta_0 - \eta_{\infty}} = \frac{1}{1 + (\lambda \cdot \dot{\gamma})^m}$	Solution (%Wt)	Relaxation time $\lambda$ (s)	Weissenberg number $Wi = \dot{\gamma} \lambda$	m	$\eta_0$ (Pa s)	$\eta_{\infty}$ (Pa s)
	$x_g = 3$	0.042	2.1	0.749	2.344	0.058
	$x_g = 2$	0.012	0.6	0.877	0.408	0.043

### 3. Viscoelastic scaling

#### 3.1. Weissenberg number

Weissenberg number is the ratio of viscous forces to the elastic forces, often used to characterize the viscoelasticity of the fluid. The definition might vary among sources, but usually is given by the relation of stress relaxation time of the fluid and a specific process time. For instance, in simple steady shear, it is defined as the shear rate times the relaxation time.

$$Wi = \frac{\text{elastic forces}}{\text{viscous forces}} = \frac{\tau_{xx} - \tau_{yy}}{\tau_{xy}} = \frac{\lambda \mu \dot{\gamma}^2}{\mu \dot{\gamma}} = \dot{\gamma} \lambda.$$

$\dot{\gamma}$  is the shear rate and  $\lambda$  is the fluid relaxation time.

#### 3.2. Deborah number

The Deborah number distinguishes how a particular material will behave over a given timeframe (we inherently assume that the material must be experiencing a deformation over this timeframe). If the time of observation is long or the relaxation time of the material is short, then “fluid-like” behavior is to be expected. Conversely, if the relaxation time of the material is large, or the time of observation short, then the Deborah number is high and the material behaves, for all practical purposes, as a solid [22]. Hence, Deborah number can be described as a “time scale of the process” or “fluid residence time” in a given regime within a complex flow field.

Table 11: Properties of PEO solutions

$De = \lambda/tp$	Solution (% Wt)	Relaxation time, $\lambda$ (s)	$De^1$ Main channel	$De$ Expansion
Water/ PEO	$x_g = 3$	0.042	$\sim 0.042$	$\sim 0.023$
	$x_g = 2$	0.012	$\sim 0.012$	$\sim 0.007$

<sup>1</sup> The average frame number per second is used to find the appropriate timeframe. This number is around 1.0 second for the main channel and 1.8 seconds for the expansion region

The shear-rate-dependence of viscosity of the shear thinning PEO solutions and the concentration-dependence viscoelastic properties of these solutions makes the study of the dynamic behavior interesting and complex at the same time.

## 4. Viscoelasticity

The previous studies failed to explore and address two of the most important aspects of viscoelastic droplets: a) shear-rate dependence of viscosity, and b) the relaxation time associated with polymer concentration.

### 4.1. Shear rate dependence of viscosity

The global shear rate and the localized shear gradient profile in which droplets experience in the channel are important parameters that need to be investigated. Our approach in this section will address these questions which helps with a better understanding of underlying physics and the transient behavior of droplets as they experience a range of shear rates while migrating in our rectangular cross-section channel.

We can estimate the apparent shear rate from the flow rate of the main channel with rectangular cross section, according to proposed by [15]. In their work, they investigated the shear viscosity and shear rate for rectangular channels with an aspect ratio  $\phi = H/W$  from 0.1 to 1.0. However, they noted that the error associated with their calculation becomes large as the aspect ratio deviates from one. The following correlation estimates an average global shear rate; however, it does not provide an accurate measure of local shear rates.

$$\dot{\gamma}_a = \left( \frac{6Q}{WH^2} \right) \left( 1 + \frac{H}{W} \right) f^* \left( \frac{H}{W} \right)$$

The trajectory of droplets in our channel indicated that droplets undergo a varying shear rate, associated with the local shear rate as they laterally migrate towards the channel center. This implies that the droplet local viscosity might vary for the duration of the migration of the

droplet. Therefore, investigating the dynamics of the droplets as they experience varying local shear rates, could be helpful to better understand their real-time migration behavior. The average wall shear rate of  $275 \text{ s}^{-1}$  corresponding to the volumetric flow rate of  $Q = 107 \text{ }\mu\text{L}/\text{min}$  was obtained from the above correlation which includes an approximated 25% error estimated for our aspect ratio of  $\varphi = 0.3$  ( $f^*_{0.3} = 0.7597$ ).

The shear-rate on droplets can be calculated by knowing their local velocity gradient. We can obtain the local shear rate of a droplet by combining the experimental result with our numerical simulation of the flow field. Droplet position (centroid) in the channel was obtained by analyzing the high-speed videos of our experiment and the local flow field surrounding the droplet was known from the simulation. Therefore, we incorporated the average trajectory of droplets from our experiment into the simulation and calculated the local shear rate corresponding to each droplet at any given position. This approach interconnects the experimental data (both from the high-speed videos of droplet migration and also from the viscosity measurement data) and the simulation of the flow to give a reasonable approximation of the local shear rate, and consequently, local viscosity of the droplets along the channel. shows the calculated shear rate from the simulation along the path of the average droplet trajectory obtained from the experiment which was incorporated into the COMSOL model.

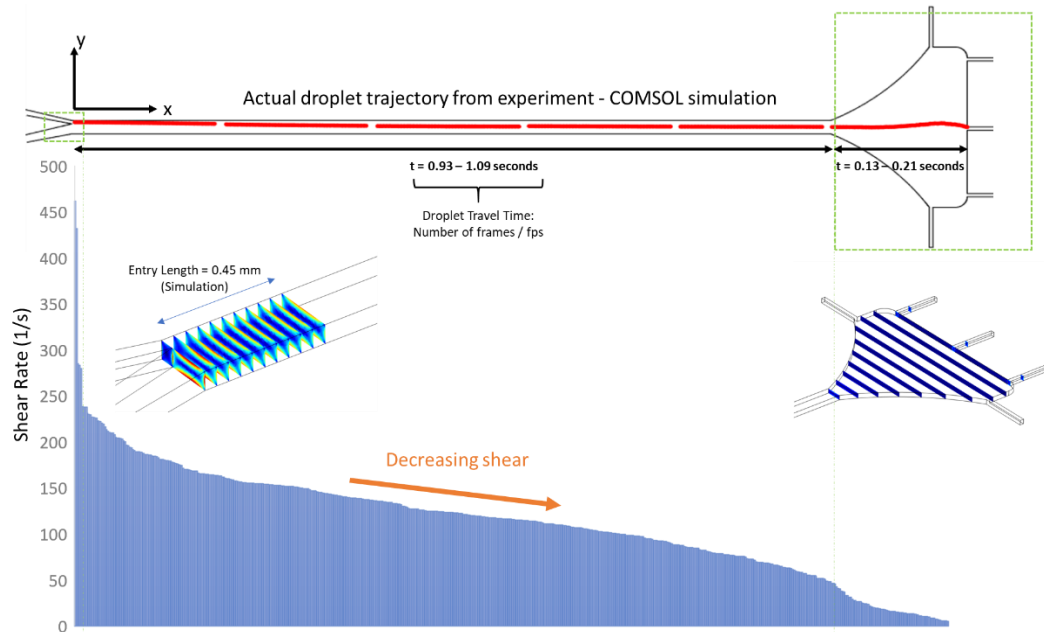


Fig. 37: shear rate along channel

At the beginning of the main channel, droplets initially start very close to the wall, then migrate towards the channel center, and at the end of the main channel they enter the expansion region. As expected, the shear rate decreased along the channel in the path of droplet migration trajectory.

In the developing flow region denoted as Sec I in Fig. 29, the droplets experience a large wall shear rate. The wall shear from [15] was around  $275 \text{ s}^{-1}$  ( with a  $\pm 25\%$  associated error) which was slightly lower than the calculated wall shear rate of  $300 - 450 \text{ s}^{-1}$  obtained from the numerical simulation. As shown in Fig. 36, at this shear rate, the viscosity is the lowest within the range of our measurements. However, we assume that this increase in the shear rate which can largely reduce the viscosity does not have an impact in the viscosity of the non-Newtonian droplets, considering the time it would take for the polymeric droplet to experience this change. On the other word, the time scale of a change in the polymer droplet (relaxation time) is greater than the time that the PEO droplet experience the very large shear rate. We estimated the time that a droplet remains in this region (Sec I) is around 0.025 seconds which is an order of magnitude smaller than the relaxation time of the polymer droplet. Within this time, the shear

rate that the droplet experience, drops from  $\sim 450 \text{ s}^{-1}$  to around  $250 \text{ s}^{-1}$ . This implies that the viscosity of the droplet may not change within the length of the transient region of Sec I (0.45 – 0.5 mm). Therefore, we assumed that the largest shear rate that the droplet experiences at the beginning of the straight channel is around  $250 \text{ s}^{-1}$ .

A more quantifiable values for the local shear rates of two segments of the straight channel is shown in Fig. 38.

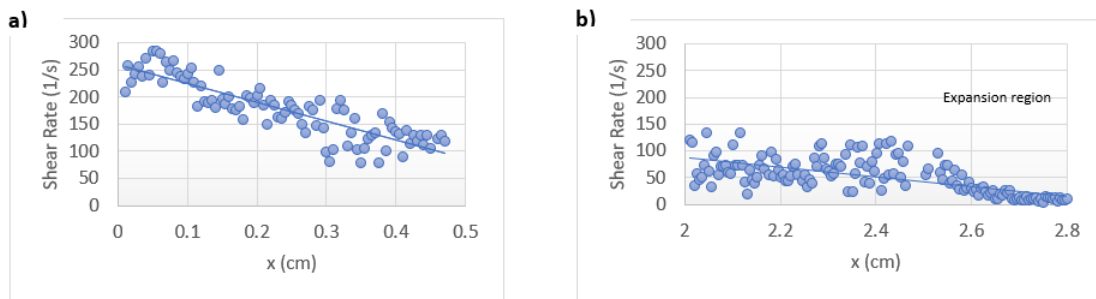


*Fig. 38: Localized shear rate of droplets – a) first 500  $\mu\text{m}$  region, b) 50  $\mu\text{m}$  upstream of the expansion region and the expansion region*

According to the range of the shear rate, for a given droplet trajectory along the channel, we can identify the shear-rate dependence viscosity of the droplets in the main channel and the expansion region. Due to the geometrical differences between these two regions, they can be easily separated from each other. The green region in Fig. 39 represents the viscosity variation in the main channel, and the blue region corresponds to the range of viscosity changes in the expansion region.



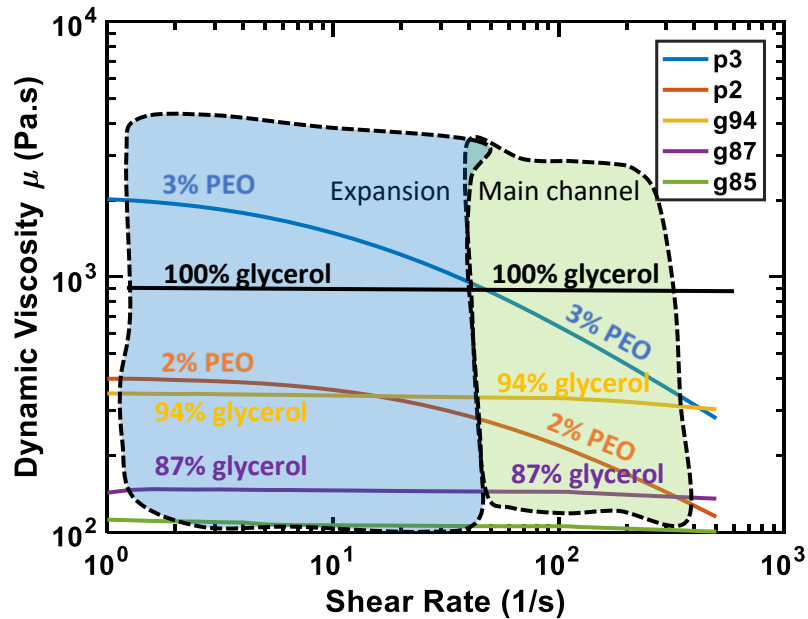


Fig. 39: Viscosity chart for PEO and GW solutions in the main channel (green) and the expansion region (blue) – shear thinning behavior of PEO solutions. The legends indicating different solutions.

Based on the viscosity chart presented in Fig. 39, viscosity of 2% PEO solution may vary between the range of the viscosity of 87% and 94% glycerol/water mixture solutions in the main channel (green region), and is comparable to viscosity of the 94% glycerol/water mixture, in the expansion region (blue region). In the expansion region, the viscosity of both 2% PEO and 94% glycerol/water mixture remains relatively constant, allowing us to isolate the contribution of viscoelasticity of non-Newtonian solutions. We note that viscosity of 3% PEO and 100% glycerol/water mixture equate at a around shear rate of  $50 \text{ s}^{-1}$ , however, due to the very large variations in the viscosity of 3% PEO, we did not choose any of these two solutions in our study.

We used the shear-rate dependent viscosity from our measurement data for both Newtonian and non-Newtonian solutions (Fig. 39) and estimated the local viscosity of each droplet corresponding to the local shear rate of each droplet trajectory along the channel. The estimated local viscosity of droplets for the entire length of the channel including the expansion region is shown in Table 12.

Table 12: Percentage viscosity variation for different solution undergoing varying shear rate

	Solution (% Wt)	Dynamic Viscosity	% change	Dynamic Viscosity	% change
		$\eta_{avg}$ (Pa s) Shear rate: 250 - 70 (1/s) Main channel		$\eta_{avg}$ (Pa s) Shear rate: Below 70 (1/s) Expansion	
Water/ glycerol mixtures	$x_g = 93.9$	$\sim 0.33$	$< 1.5\%$	$\sim 0.33$	$< 1.5\%$
	$x_g = 87.2$	$\sim 0.14$	$< 1.5\%$	$\sim 0.14$	$< 1.5\%$
Water/ PEO	$x_g = 3$	$0.4 - 0.75$	87%	$0.75 - 1.6$	113 %
	$x_g = 2$	$0.15 - 0.24$	60%	$0.24 - 0.36$	50%

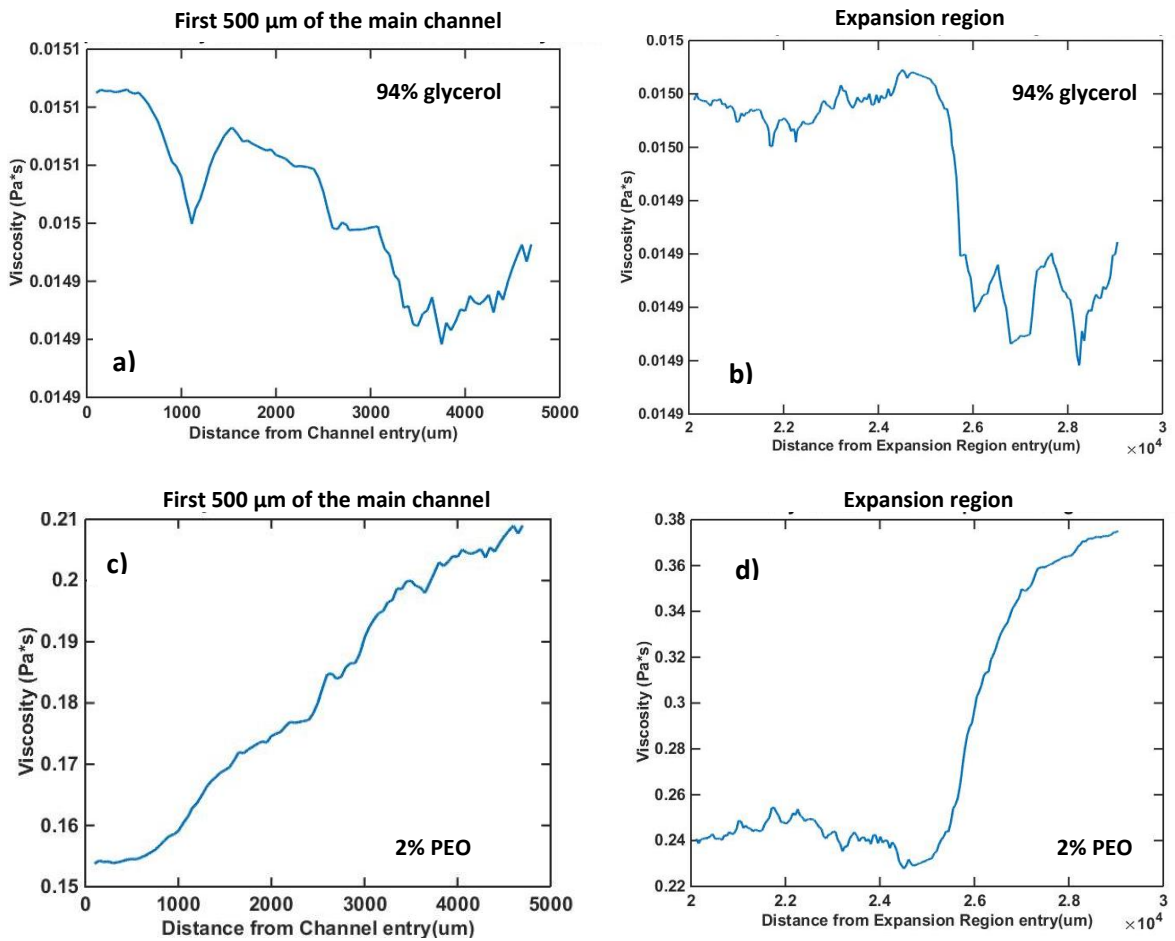


Fig. 40: Localized viscosity for the first 500 μm region, and 50 μm upstream of the expansion region and the expansion region, a,b) Newtonian Droplets, c,d) non-Newtonian droplets

## 5. Results

As in the case for Newtonian droplets, non-Newtonian droplets migrated to the channel center owing to the large inertial migration effects, regardless of their viscosity ratio or relaxation time. However, numerically predicting their inertial migration rate would be more complex than the Newtonian droplets, due to the variation in droplet viscosity in the channel and the relaxation time of the non-Newtonian droplets. As a result, unlike the previous approach in Chapter 6, we focus our study on obtaining the average droplet trajectories as a mean to investigate the effect of viscoelasticity in droplet separation.

### 5.1. Experiment condition

The experimental condition for this study is shown in Table 13 with a comparison with the previous study of the viscosity ratio effect in Chapter 5.

*Table 13: experimental condition*

	<b>Viscosity ratio experiment (Ch 5)</b>	<b>Viscoelasticity experiment (Ch 6)</b>
<b>Material</b>	Glycerol/water mixture 50-85%	Glycerol/water 85-100%, PEO 2-3 %
<b>Channel height / Channel aspect ratio</b>	$H = 120 \mu\text{m} / \varphi = 0.24$	$H = 150 \mu\text{m} / \varphi = 0.3$
<b>Avg. droplet size / droplet aspect ratio</b>	$a = 82 \mu\text{m} / \zeta = 0.58$	$a = 105 \mu\text{m} / \zeta = 0.86$
<b>Total flow rate</b>	$Q_{\text{tot}} = 106 \mu\text{L}/\text{min}$	$Q_{\text{tot}} = 109 \mu\text{L}/\text{min}$

In this chapter first, we present the result that shows separation enhancement for Newtonian droplets as the channel aspect ratio ( $\varphi$ ), and the droplet size ratio ( $\zeta$ ) become larger. Remember from our previous discussion that the droplet size directly influences the magnitude of the inertial lift force; larger droplets migrate faster to the channel enter – sometimes regardless of their properties. Based on the previous result, we expect that the droplets that are located at the center of the channel, having the maximum velocity before entering the expansion

region and their axial velocity asymptotically decreases. The schematic of the device and the area of interest (AOI) is shown in Fig. 41.

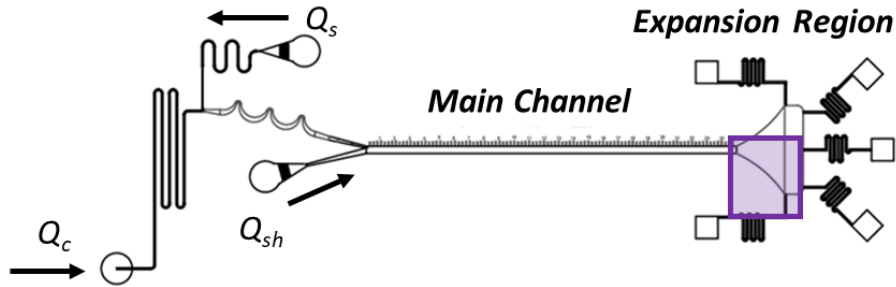


Fig. 41: Device schematic identifying the AOI in this section

## 6. Discussion

Fig. 42, shows the experimental result for this section. We observed a larger separation between trajectories with an increase in droplet size ratio ( $\zeta$ ). Further increase in droplet size ratio ( $\zeta$ ) resulted in droplets with lower viscosity ratio entered the middle outlet while others entered the side outlet. This result shows the importance of droplet size that can be used for an enhancement of viscosity ratio-based separation mostly towards the end of the channel where distinct trajectories for droplets with different viscosity ratios was observed. This result signifies the effect of droplet size ratio, denoted as,  $\zeta$ .

In the expansion region, inertial effect becomes less dominant (Reynold number decreases), allowing for a more pronounce contribution of the viscosity ratio. In this region, the sudden change in the flow condition may result in a deformation of droplets depending on the viscosity ratio. As the viscosity ratio increases, droplets become less deformable (lower Ca number). This is in addition to the slower motion of the more viscous droplets (due to the thinner lubrication layer). However, as it is shown in the Fig. 42B, the axial velocity of the droplets is quite similar to one another, therefore, we attribute the difference in the droplet trajectory to the

deformability of the droplets (deformability-induced lift force). The more deformable droplets stay closer to the channel centerline. The effect of gradual area (velocity) change needs to be also considered. We conclude that, droplet size and channel confinement contribute to an enhanced separation of droplets; larger channel aspect ratio,  $\phi$ , and larger droplet size ratio,  $\zeta$ , result in a more distinct trajectories for a given droplet viscosity ratio.

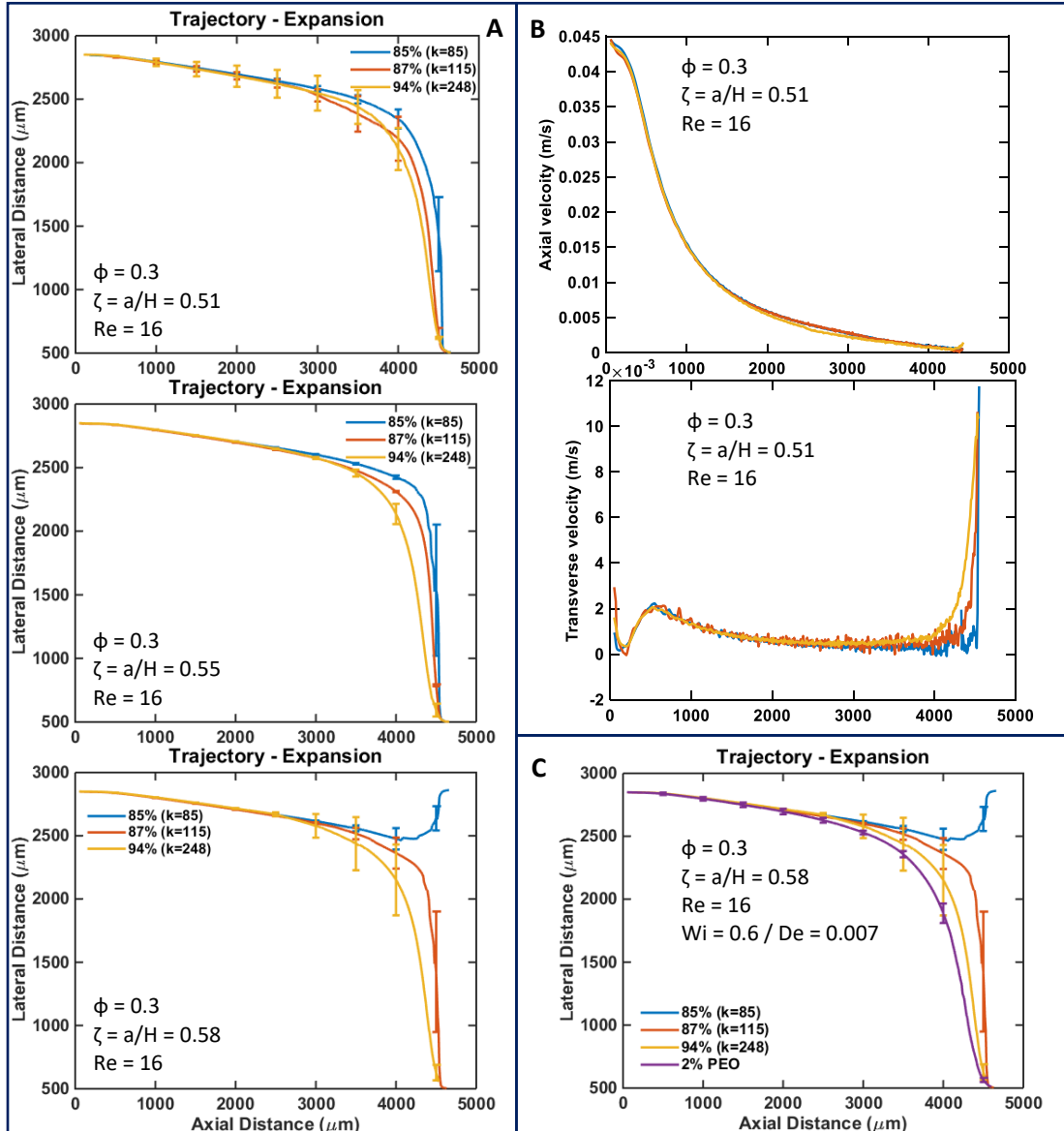


Fig. 42: A) Trajectories of Newtonian droplets in the expansion region ( $\zeta = 0.51 - 0.58$ ,  $\phi = 0.3$ ), B) Axial and Transverse velocity along the expansion region, C) Trajectories of Newtonian & non-Newtonian droplets in the expansion region ( $\zeta = 0.58$ ,  $\phi = 0.3$ )

As it can be seen in Fig. 42, for  $\zeta = 0.58$ , the droplets containing solution of 85% glycerol/ water mixture were collected in a different outlet (middle outlet) from the other solutions. The trajectories were so distinct with small standard deviation. Therefore, the current design can be used to distinguish between droplets of varying viscosities. However, more outlets can be implemented in the expansion region for optimizing droplet collection (Fig. 43).

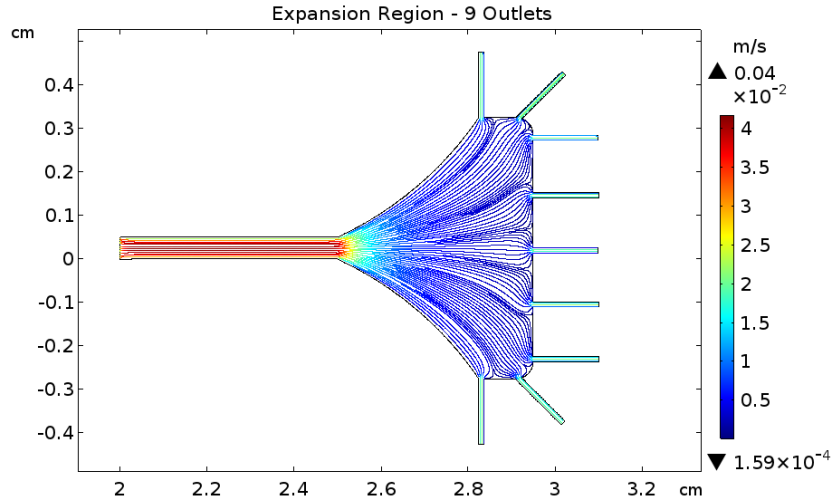


Fig. 43: COMSOL simulation of flow field and fluid streamlines in the expansion region with more outlets

Thus far we have demonstrated the ability to distinguish between Newtonian droplets, given the channel aspect ratio of above  $\zeta = 0.55$ , signifying the effect of channel height and droplet size in sorting droplets. Next, we investigate the effect of viscoelasticity of 2% PEO, on droplet trajectories, and compare the result with the 94% glycerol/ water solution shown in Fig. 42 C. The same droplet size ratio,  $\zeta = 0.58$ , was used for droplets of 2% PEO.

According to the viscosity measurement graph shown in Fig. 39, viscosity of 2% PEO and 94% glycerol/ water solution is similar in the expansion region. This implies that, the deviation observed in trajectories between 2% PEO and 94% Glycerol mixture droplets (Fig. 42 C) is related to the viscoelastic properties of PEO droplets, i.e. Deborah number. We believe the force balance mechanism is influenced by the presence of viscoelasticity in PEO droplets. The

relaxation time, in which both  $Wi$  and  $De$  numbers are based on, can be interpreted as the resistance to a sudden change. Here, PEO droplet resist the deformation once the sudden change in flow condition occurs in the expansion region. We can think of the relaxation time as a delay in adopting to the change. This delay perhaps is directly related to the degree of viscoelasticity (larger polymer concentration experience larger resistance to the deformation).

The higher concentration of PEO solution, exhibits larger relaxation time,  $\lambda$ , as well as an increase in the overall viscosity of the solution. From the result presented in **Error! Reference source not found.**, the direction of lateral migration force is away from the channel centerline, and towards region with higher shear rate.

Fig. 44 indicates an interesting observation. It shows the importance of viscoelastic properties in migration of droplets, compare to the viscosity ratio. There is a large viscosity difference between 2% and 3% PEO solutions and based on the result presented in Fig. 42, we should have expected to see a large difference in the trajectories between these two solutions, if they were not viscoelastic, or at least one of them was not. However, we see a similar behavior for both solutions which indicates that viscoelastic properties dominating the viscosity ratio effects.

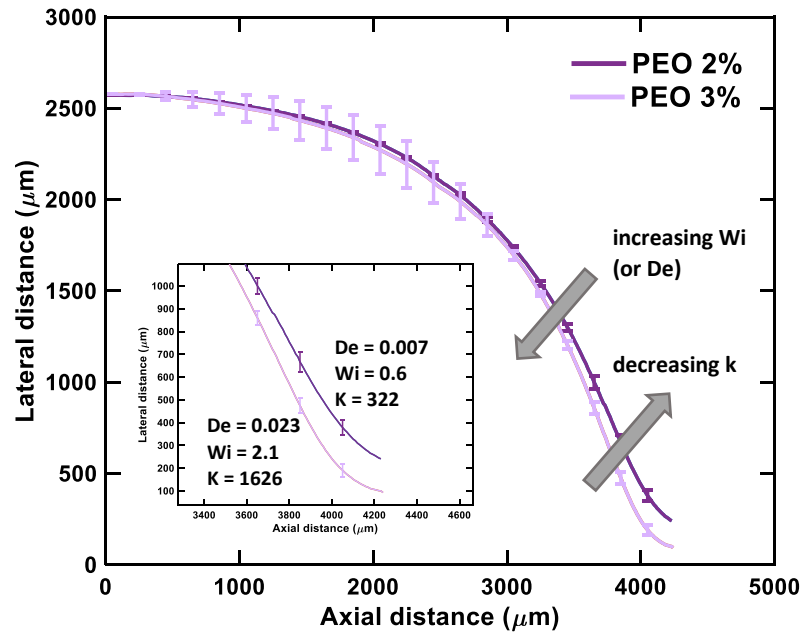


Fig. 44: competition between viscosity and viscoelasticity

In this chapter, we explored the effect of viscoelasticity of the polymer solutions on droplet migration and demonstrated that viscoelasticity could be used as a marker to distinguish between Newtonian and non-Newtonian droplets. Most of biological reactions either produce, or simply deal with viscoelastic fluids, and viscoelasticity can be used as a biomarker for separation of droplets of interest within a heterogeneous population. Furthermore, the deviation of the trajectories of viscoelastic droplets, from the trajectory of a known viscous droplet, can be used to measure the viscoelasticity of the solutions where the conventional equipment cannot be used. In the next chapter, we will discuss a how a change in the channel geometry and flow rate can further improve the separation efficiency.



## 7. References

- [1] L. Mazutis, J. Gilbert, W. L. Ung, D. A. Weitz, A. D. Griffiths, and J. A. Heyman, "Single-cell analysis and sorting using droplet-based microfluidics," *Nat. Protoc.*, vol. 8, no. 5, pp. 870–891, 2013.
- [2] J. Clausell-Tormos et al., "Droplet-Based Microfluidic Platforms for the Encapsulation and Screening of Mammalian Cells and Multicellular Organisms," *Chem. Biol.*, vol. 15, no. 5, pp. 427–437, 2008.
- [3] W. Lee, L. M. Walker, and S. L. Anna, "Role of geometry and fluid properties in droplet and thread formation processes in planar flow focusing," *Phys. Fluids*, vol. 21, no. 3, 2009.
- [4] P. Zhu and L. Wang, "Passive and active droplet generation with microfluidics: a review," *Lab Chip*, vol. 17, no. 1, pp. 34–75, 2017.
- [5] A. C. Hatch, A. Patel, N. R. Beer, and A. P. Lee, "Passive droplet sorting using viscoelastic flow focusing," *Lab Chip*, vol. 13, no. 7, p. 1308, 2013.
- [6] and A. S. Segre, G., "Behavior of macroscopic rigid spheres in Poiseuille flow," *J. Fluid Mech*, vol. 14, no. 1958, pp. 136–157, 1962.
- [7] H. Amini, W. Lee, and D. Di Carlo, "Inertial microfluidic physics," *Lab Chip*, vol. 14, no. 15, p. 2739, 2014.
- [8] C. K. W. Tam and W. A. Hyman, "Transverse motion of an elastic sphere in a shear field," *J. Fluid Mech.*, vol. 59, no. 1, pp. 177–185, 1973.
- [9] S. C. Hur, N. K. Henderson-MacLennan, E. R. B. McCabe, and D. Di Carlo, "Deformability-based cell classification and enrichment using inertial microfluidics," *Lab Chip*, vol. 11, no. 5, p. 912, 2011.
- [10] R. M. Erb, D. Obrist, and P. W. Chen, "Predicting sizes of droplets made by microfluidic flow-induced dripping †," no. 10, pp. 8757–8761, 2011.
- [11] C. A. Stan, L. Guglielmini, A. K. Ellerbee, D. Caviezel, H. A. Stone, and G. M. Whitesides, "Sheathless hydrodynamic positioning of buoyant drops and bubbles inside microchannels," *Phys. Rev. E - Stat. Nonlinear, Soft Matter Phys.*, vol. 84, no. 3, p. 4840, 2011.
- [12] P. C. H. Chan and L. G. Leal, "The motion of a deformable drop in a second-order fluid," *J. Fluid Mech.*, vol. 92, no. 1, pp. 131–170, 1979.
- [13] Dow, "Density of Glycerine-Water Solutions," Edge, p. 99800.
- [14] N. Cheng, "Formula for Viscosity of Glycerol-Water Mixture," pp. 3285–3288, 2008.

- [15] Y. Son, "Determination of shear viscosity and shear rate from pressure drop and flow rate relationship in a rectangular channel," *Polymer (Guildf)*, vol. 48, no. 2, pp. 632–637, 2007.
- [16] K. W. Ebagninin, A. Benchabane, and K. Bekkour, "Rheological characterization of poly(ethylene oxide) solutions of different molecular weights," *J. Colloid Interface Sci.*, vol. 336, no. 1, pp. 360–367, 2009.
- [17] J. D. Berry, M. J. Neeson, R. R. Dagastine, D. Y. C. Chan, and R. F. Tabor, "Measurement of surface and interfacial tension using pendant drop tensiometry," *J. Colloid Interface Sci.*, vol. 454, pp. 226–237, 2015.
- [18] J. Husny and J. J. Cooper-White, "The effect of elasticity on drop creation in T-shaped microchannels," *J. Nonnewton. Fluid Mech.*, vol. 137, no. 1–3, pp. 121–136, 2006.
- [19] B. H. A. Stone and B. J. B. L. G. Leal, "An Experimental Study of Transient Effects in the Breakup of Viscous Drops.PDF," pp. 131–158, 1986.
- [20] S. L. Anna, N. Bontoux, and H. A. Stone, "Formation of dispersions using 'flow focusing' in microchannels," *Appl. Phys. Lett.*, vol. 82, no. 3, pp. 364–366, 2003.
- [21] S. Mortazavi and G. Tryggvason, "A numerical study of the motion of drops in Poiseuille flow. Part 1. Lateral migration of one drop," *J. Fluid Mech.*, vol. 411, pp. 325–350, 2000.
- [22] R. Poole, "The Deborah and Weissenberg numbers," *Rheol. Bull.*, vol. 53, no. 2, pp. 32–39, 2012.
- [23] L. Zhu and F. Gallaire, "A pancake droplet translating in a Hele-Shaw cell: Lubrication film and flow field," *J. Fluid Mech.*, vol. 798, pp. 955–969, 2016.
- [24] Y. Ling, J. M. Fullana, S. Popinet, and C. Josserand, "Droplet migration in a Hele-Shaw cell: Effect of the lubrication film on the droplet dynamics," *Phys. Fluids*, vol. 28, no. 6, 2016.
- [25] E. J. Hinch, "Lecture 7 : Stress Relaxation," pp. 65–82.
- [26] Z. Nie et al., "Emulsification in a microfluidic flow-focusing device: Effect of the viscosities of the liquids," *Microfluid. Nanofluidics*, vol. 5, no. 5, pp. 585–594, 2008.
- [27] F. Del Giudice, S. J. Haward, and A. Q. Shen, "Relaxation time of dilute polymer solutions: A microfluidic approach," *J. Rheol. (N. Y. N. Y)*, vol. 61, no. 2, pp. 327–337, 2017.
- [28] E. N. Lightfoot, W. S. W. Ho, K. K. Sirkar, and A. L. Zydney, "Membrane handbook," *AIChE J.*, vol. 41, no. 3, pp. 503–504, 1995.

## Chapter 7 – Enhanced Separation based on Viscoelasticity in Confined Geometries

### 1. Introduction

The platform presented earlier has demonstrated the ability to passively isolate droplets based on size, viscosity ratio and viscoelasticity in a high throughput manner. Droplet size was comparable to the channel height ( $a < H$ ), in which droplets migrated without considerable restrictions from channel walls. We demonstrated that as the nondimensionalized droplet size increased,  $\zeta$ , more distinct droplet trajectories were obtained, suggesting a larger separation based on viscosity ratio and viscoelastic properties of droplets (Fig. 42). However, this platform may not be able to isolate droplets effectively, unless multiple outlets are incorporated in the design of the expansion region as shown in Fig. 43. Many factors, including droplet size, flow conditions and the channel geometry affect the separation. An effective method that enables a high throughput isolation of viscoelastic droplets can benefit a diverse range of applications where non-Newtonian solutions are produced from bio-chemical reactions.

When the droplet diameter is larger than the channel height, droplets are squeezed between channel walls and exhibit a pancake-like shape. The migration mechanism of droplets confined in a Hele-Shaw cell is a complex problem as the droplet aspect ratio (droplet size to channel height,  $\zeta = \frac{a}{H}$ ) has a significant impact on droplet dynamics. There are very few studies that investigated the droplet dynamics in confined channels [1][2], and to the best of our knowledge there is no study available on the dynamics of viscoelastic droplets in such configurations.

Here, we present a microfluidics platform that enabled us to study the migration mechanism of droplets in confined geometries, where the motion of droplets may be more restricted by the channel confinement. We showed that by tuning the ratio of flow rates, we were

able to explore the impact that the flow time scale, relative to the relaxation time, might have on deformation of viscoelastic droplets. Despite the differences in the initial migration of droplets, where the droplet deformation was impacted by varying the flow time scale, for a wide range of droplet size and flow conditions, viscoelastic and viscous droplets took distinct trajectories, resulted in an enhancement in the separation of viscoelastic droplets in confined channels (Fig. 45). We observed that viscoelastic droplets migrated towards channel center with less apparent restrictions from the channel geometry, in contrast to the limited motion of viscous droplets which they were forced to stay in proximity to the wall. Counterintuitively, channel confinement had less significant impact on the motion of viscoelastic droplets. A schematic of the device used for separation of droplets based on viscoelastic properties (i.e. relaxation time) is presented in Fig. 45.

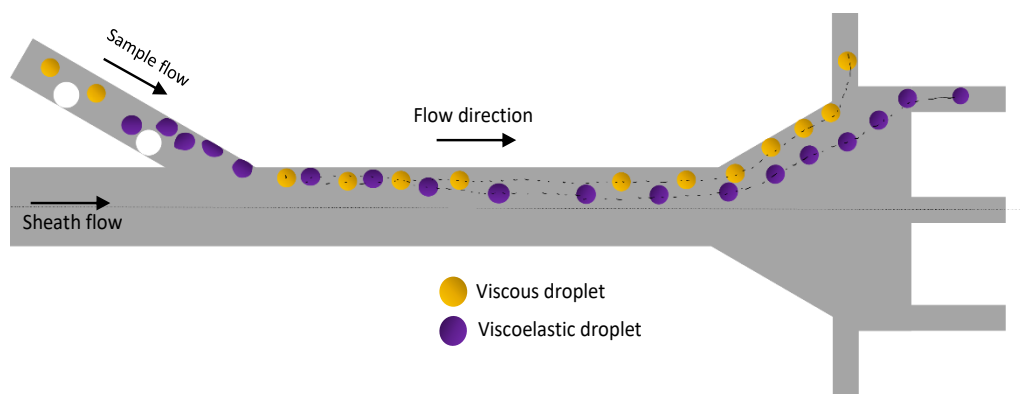


*Fig. 45: Schematic of our separation platform - distinct trajectories between viscous and viscoelastic droplets*

In this work, we study the effect of deformation and relaxation time of non-Newtonian droplets in confined channels and investigate the parameters impacting the dynamics of viscoelastic droplets in confined geometry. By manipulating the droplet shape and tuning the flow condition, we were able to demonstrate a simple and robust microfluidics platform for an extremely effective separation of viscoelastic droplets.

## 2. Theoretical background

Aqueous droplets can deform, and their deformed shape depends on the magnitude and the duration of the applied deformation source. However, the rate in which they return to their undeformed shape can be determined by their relaxation time, which is a property of viscoelastic droplets.

As it is shown in Fig. 46, two viscoelastic objects undergoing same deformation with different durations. The one that is exposed to the applied force for a shorter time, recovers to most of its original shape, whereas, the other object with longer applied force, recovers to less of its original shape. Therefore, the recovery time of the same viscoelastic material is a function of time as well. We should note that, when comparing two different viscoelastic materials which undergo the same force, Deborah ( $De$ ) number can be used to non-dimensionalize the relaxation time.

Once the source that caused the deformation of a droplet is lifted, the droplet recovers to its original shape within its relaxation time. In a confined channel where the droplets are larger than the channel height, the time for the droplets to retract back to their original shape is delayed.

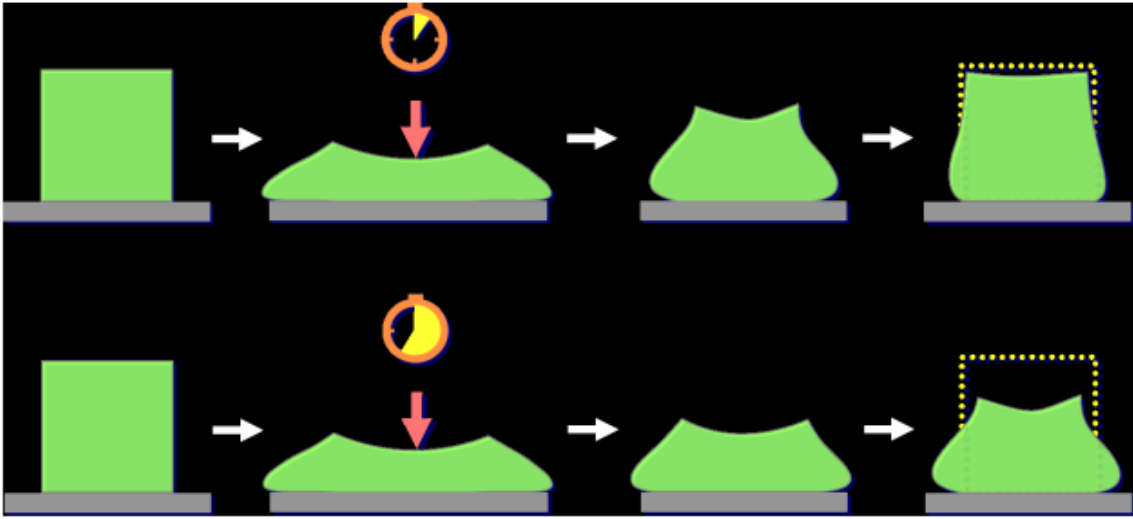


*Fig. 46: Applied force on viscoelastic material [5]*

When a non-Newtonian material is deformed, an instantaneous viscous stress builds up which scales as  $\mu_0\dot{\gamma}$ . Now suppose the material has a memory time, known as the relaxation time  $\lambda$ , then the deformation at a constant shear rate  $\dot{\gamma}$ , would be  $\dot{\gamma}\lambda$ . As in the elastic solids, the elastic stress associated with this deformation scales as  $G\dot{\gamma}\lambda$ , where  $G$  is the elastic modulus. After the relaxation time of the material has elapsed, the stress would reach a constant value of  $(\mu_0 + G\lambda)\dot{\gamma}$ . The term in the parenthesis can be thought of as an enhanced viscosity. In other words, non-Newtonian material has a characteristic memory, referred to as the relaxation time. When the applied force is removed from the material, the material relaxes over its characteristic relaxation time. This phenomenon is known as stress relaxation [3].

Relaxation time of a polymer can determine the required time to recover to its undisturbed shape after the source of deformation is removed. It was demonstrated in Chapter 6, that the relaxation time played a crucial role in separation of viscoelastic droplets. Here, we investigate the effect of relaxation time in viscoelastic separation of droplets when the channel confinement retards the shape recovery of the droplets.

As it was described in Chapter 4, relaxation time of polymers was calculated by applying the power law to the viscosity vs. shear rate measurements. The relaxation time of 2% PEO bulk solution is measured to be around 0.012 second (Table 11). We assume that the droplet containing 2% PEO solution is also having the same relaxation time. The result presented in Chapter 6 indicated that the effect of droplet viscoelasticity on droplet separation became more apparent in the expansion region where the droplets were surrounded by low Reynolds flow. We believe that the properties of viscoelastic droplets (i.e. relaxation time) resulted in slight deformation of viscoelastic droplets relative to viscous droplets, and once the inertial contribution was alleviated in the expansion region, relaxation time of viscoelastic droplets in the recovery mode, resulted in a distinguishable droplet trajectory. We attributed this behavior to the time scale of the recovery of the polymeric droplets to their undeformed shape (i.e. relaxation time) and concluded that this contributed to the distinct droplet trajectory in the expansion region.

We observed that when droplets were about twice as large as the height of the channel ( $\zeta > 2$ ), the channel confinement added a considerable resistance to the recovery time of the droplets. We examined this for viscoelastic droplets underwent a constriction area between two pillars. Within our observation time of  $\sim 1.1$  seconds, the viscoelastic droplets did not return to their original shape even after 0.7 second after the deformation sources was lifted. The time lapse our experiment on 2% PEO viscoelastic droplets is shown in Fig. 47.

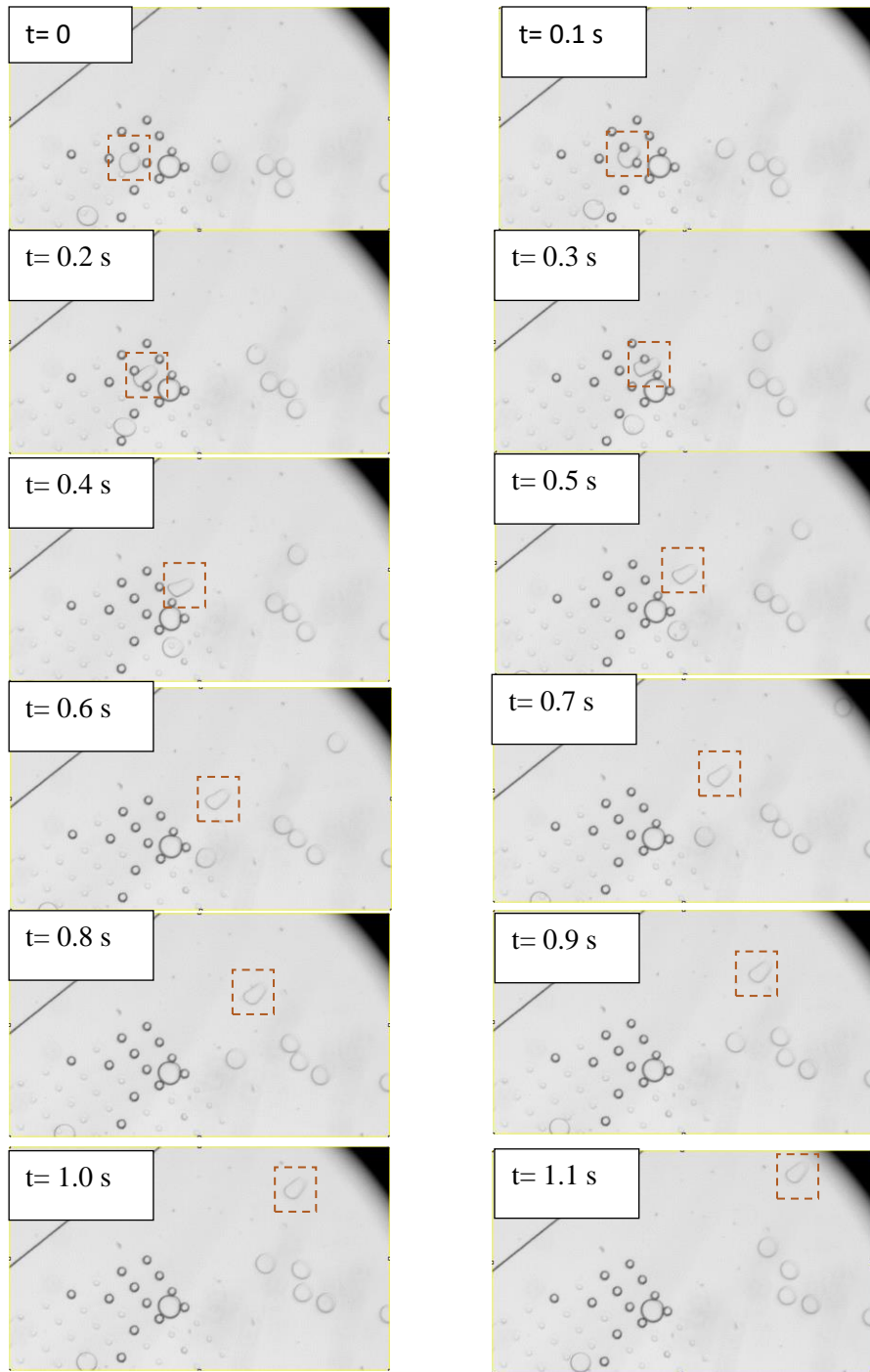


*Fig. 47: Time lapse of deformation and recovery of viscoelastic droplets*

An interesting observation occurred for the PEO droplets when they encountered forces from the pillars in the low aspect ratio channel ( $\Phi = 0.1$ ,  $\zeta > 2$ ). Droplets deformed into irregular shapes, as can be seen in Fig. 48. The constrictions resulted in a deformation of the droplet



along two dimensions; one from the height of the channel and the other one from transverse directions. We did not observe any apparent deformation for viscous droplets.

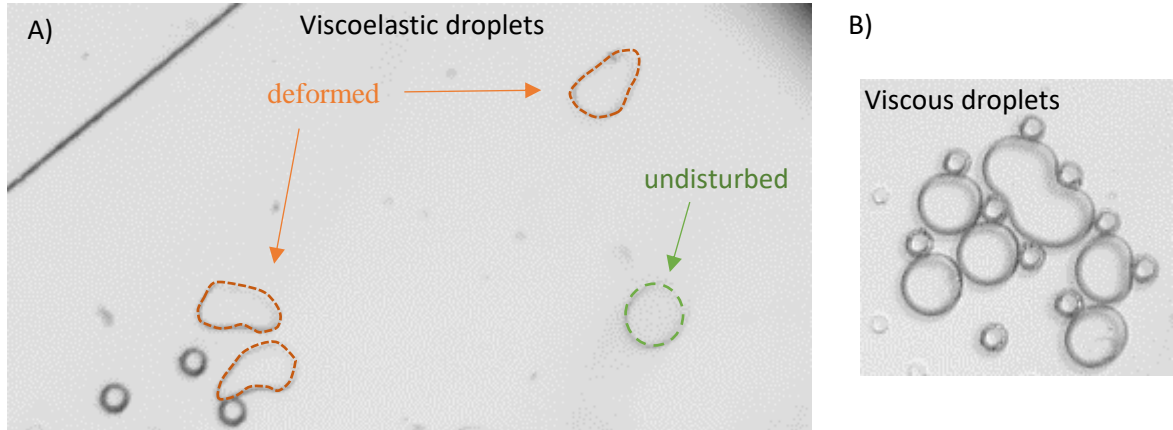


Fig. 48: A) Irregular shapes of viscoelastic droplets after deformation and B) stiff glycerol droplets

We observed a small deformation for 94% glycerol/water droplets compare to 2% PEO droplets once in high aspect ratio channel ( $\Phi = 0.3$ ) passing through an array of constrictions. The time for both droplets to recover from deformation was very fast; almost immediately for the viscous droplets and within 0.02 seconds (relaxation time) for PEO droplets (Fig. 49).

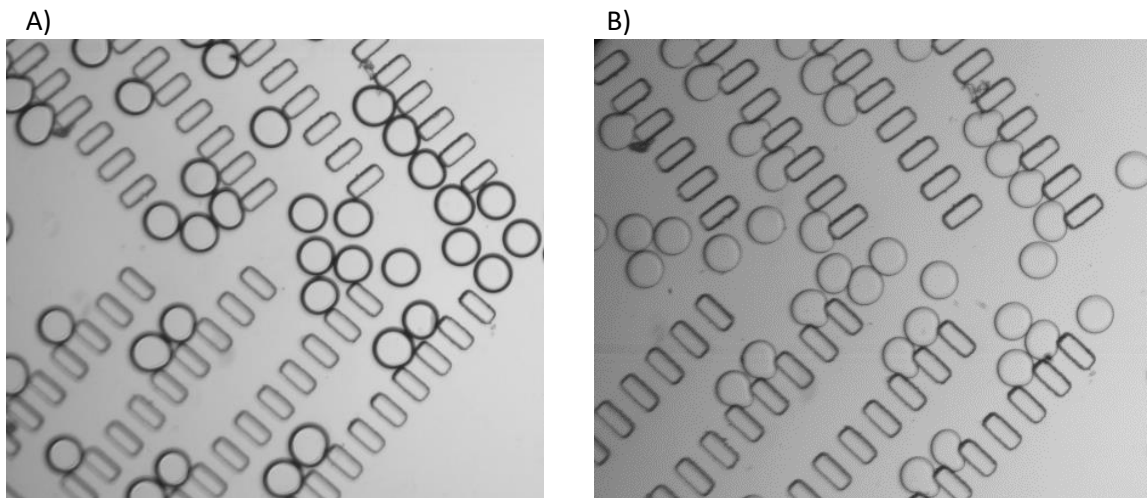


Fig. 49: deformation of droplet in high aspect ratio ( $\Phi = 0.3$ ) channel, A) viscous, and B) viscoelastic droplets

This interesting observation suggested that we can manipulate the shape of viscoelastic droplets in confined geometry and maintain the deformed shape of the droplet for a period of time, which could be larger than the relaxation time of the polymer.

### 3. Droplet deformability

As it was discussed earlier, droplet size, viscosity ratio and viscoelasticity of droplets impact the migration, and consequently effect droplet separation. However, deformability and shape of droplets could have a significant contribution to the migration mechanism which should not be underestimated. Droplet deformation induces a lift force that results in the migration of droplet towards channel center, even in the absence of inertia [4]. Moreover, non-spherical droplets experience additional lift force in which impacts the migration of droplets in microchannels. Here, we study the effect of droplet deformability and shape on droplet migration.

In order to study the droplet deformation, we designed a microfluidic device that pre-deforms the droplets right before they enter a separation channel. Droplets are being deformed via a constriction (e.g. pillar) located in one side of the upstream channel that locally restricts the channel by 50%. This channel constriction enables the local deformation of droplets. The schematic of the device is shown in Fig. 50.

The device used in this experiment has the height of 50  $\mu\text{m}$ , with an aspect ratio,  $\phi = 0.1$ . The droplets are generated in the upstream droplet generated and are larger than the channel height, therefore, they form into discoid shapes, where the actual size of the droplets can be approximated by the method described by [5]. The droplet migration in confined channels is no longer three dimensional. To the best of our knowledge, due to these constraints, there has not been any experimental study investigating the migration of droplets with large size aspect ratio ( $\zeta > 1$ ) in low aspect ratio channels ( $\phi \ll 1$ ).

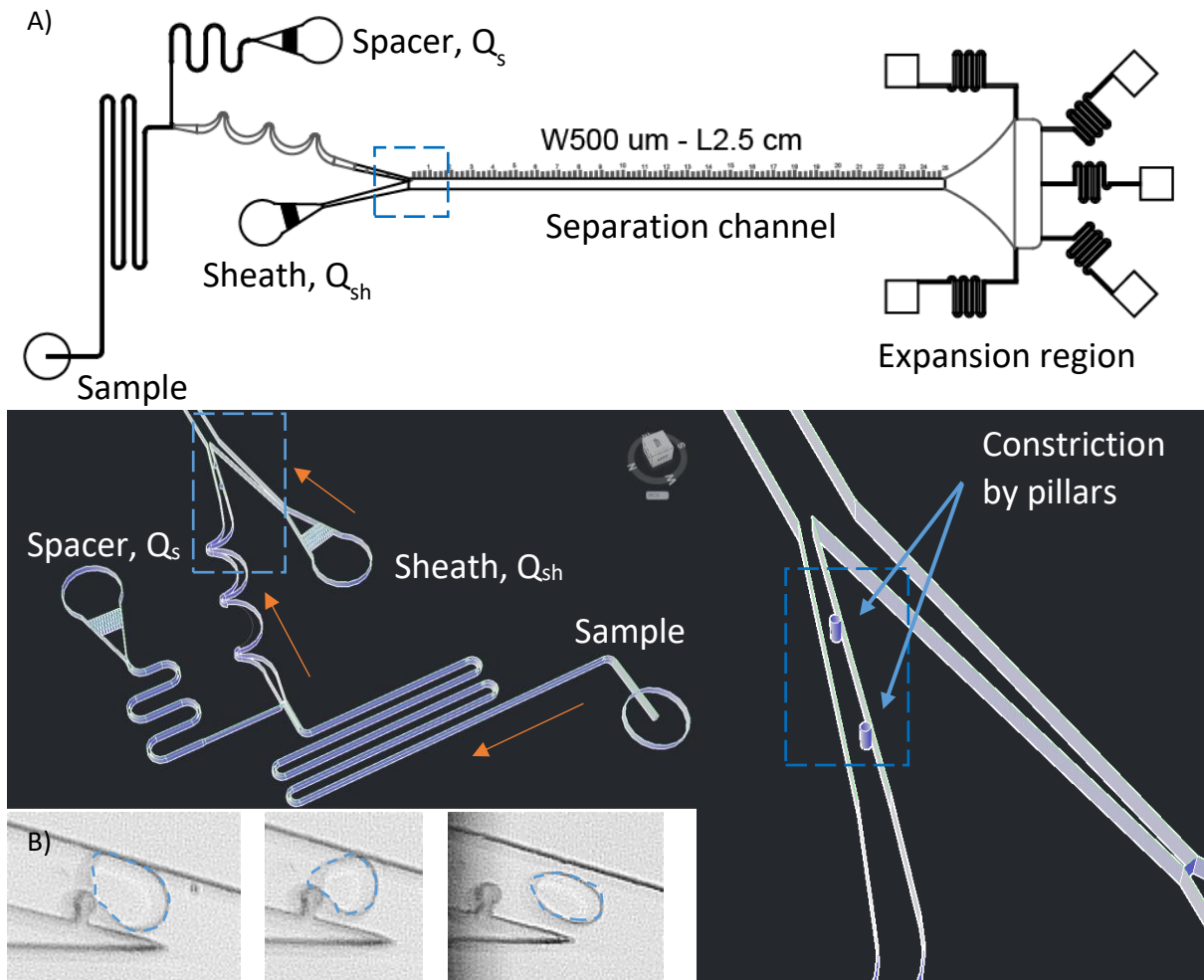


Fig. 50: Device schematic, A) close-up of the constriction B) size-dependence of droplet deformability

The degree of droplet deformation depends on the droplet size and the relaxation time. Larger droplets tend to be more deformable and maintaining their deformed shape for a longer period. The current design enables manipulation of droplet's shape by two means: a) droplet deforation caused by a physical obstruction in the upstream channel, as discussed before, and b) droplets deformation caused by flow from the sheath flow stream – the degree of deformation is a function of flow rate. The magnitude of the applied force by the sheath flow is varying due to the change in the shape of the channel where the droplet stream intersects with the sheath flow stream. Combination of both deformation by pillar and the deformation caused by the sheath

flow result in an overall deformation of the droplet. If we determine that the time scale of deformation is shorter than the relaxation time of the droplet, we can maintain the shape of the droplet after deformation.

#### 4. Migration mechanism in low aspect ratio channel ( $\phi = 0.1$ )

The underlying mechanism responsible for low mobility of the viscous droplet is not fully understood. We believe that the shape and the deformability of the viscoelastic droplets are the main contributors to the initial migration of viscoelastic droplets, which consequently resulted in an enhancement in droplet separation. We demonstrate in this section that droplet shape and deformability combined with the channel confinement, and the flow conditions, greatly impact the initial migration of droplets. In confined channels (channel aspect ratio,  $\phi = H/W = 0.1$ ), the droplet aspect ratio ( $\zeta = a/H$ ) is greater than unity and should be considered as an important parameter in migration.

In low aspect ratio channels, migration mechanism might be altered due to the channel confinement. We hypothesized that when the droplets are in a confined channel where the channel walls may restrict their movement, elastic properties of viscoelastic droplets aids in droplets adopting the shape of the channel, displaying more deformation, and therefore experiencing less restriction compare to the viscous droplets. We noticed that the stiffer and less deformable viscous droplets stayed closer to the wall and thus traveling at a lower velocity. With an increase in the channel flow rate the wall effect component of the lift force overcomes the viscous forces from the channel confinement, and the droplets were lifted away from the wall. As the droplets away from the channel wall, the velocity gradient component of the lift force, combined with the low droplet mobility, opposes their migration further and droplets push back towards the channel wall. There are some fluctuations in the trajectory of droplets downstream of the channel, however, the mean trajectory of the droplets is close to the wall.

Once the inertial lift force is weakened due to the reduction in the local Reynolds number in the expansion region, the viscous droplets are entirely positioned at the wall. However, this is not the case for viscoelastic droplets; the initial migration of viscoelastic droplets resulted in the droplets to be located more towards the center of the channel and the direction of the viscoelastic lift force keeps the droplets closer to the channel centerline rather than away from the wall. Thus, once the droplets enter the expansion region, their trajectory is distinguishable from the viscous droplets that are located at the wall. We can argue that the reason for viscous droplets to stay close to the wall is the geometry constraints which prevents the droplets from having a shape change required for the lateral migration of deformable droplets, even in the absence of an inertia. The inertial forces must overcome the viscous forces cause by the channel confinement.

#### 4.1. Flow time scale - short

We studied the migration of droplets of 2% PEO (viscoelastic) and 93% Glycerol (viscous) in the new device consisting of pillar constriction, as shown in Fig. 50. The following criteria were used,  $\phi = 50/500 = 0.1$ ,  $\zeta = 130 / 500 = 0.25$ , and  $Q_r = 9 / 45 = 0.25$ . Once the droplets make contact with the pillar, they deform. However, we observed that viscous droplets recover to their undisturbed shape almost instantaneously. However, PEO droplets were deformed to an elongated ellipsoidal shape, in contrast to the spherical shape of the viscous droplets. The orientation of the PEO droplets was also parallel to the direction of the flow. The combination of the shape and the orientation of the PEO droplets resulted in a significantly faster motion of these droplets compare to the viscous droplets. The large axial velocity of PEO droplets (Fig. 51A) resulted in a fast transformation of droplets into the main channel and their migration towards the channel center, once they entered the separation channel.

Trajectory of both PEO and glycerol droplets is shown in Fig. 51. In contrast to zero initial lateral migration of viscous droplets, a significantly large migration at the beginning of the channel was observed for viscoelastic droplets. The highlighted area in Fig. 51 corresponds to the initial migration region. The motion of viscous droplet appears to be limited to proximity of the wall for the entire length of the channel.

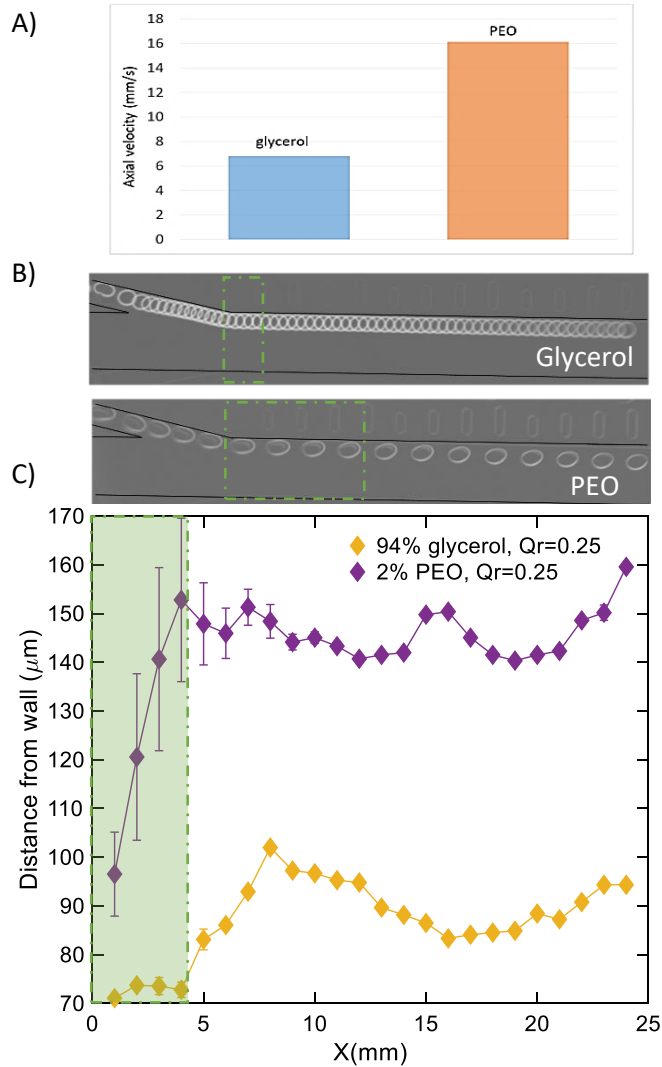


Fig. 51: migration of droplets in the separation channel, A) axial velocity of PEO and glycerol droplets, B) time lapse of high speed video of droplet migration C) droplet's distance from the wall for the entire length of the channel – the Initial migration region is highlighted

The migration of droplets continued till the end of the straight channel after the initial migration mode. At the end of the straight channel, viscoelastic droplets were approximately 80

$\mu\text{m}$  apart from viscous droplets. The separation of droplet was enhanced significantly in the expansion region (Fig. 52A), such that the droplets became 1 mm apart in the lateral direction, after travelling 2 mm in the flow direction (Fig. 52B).

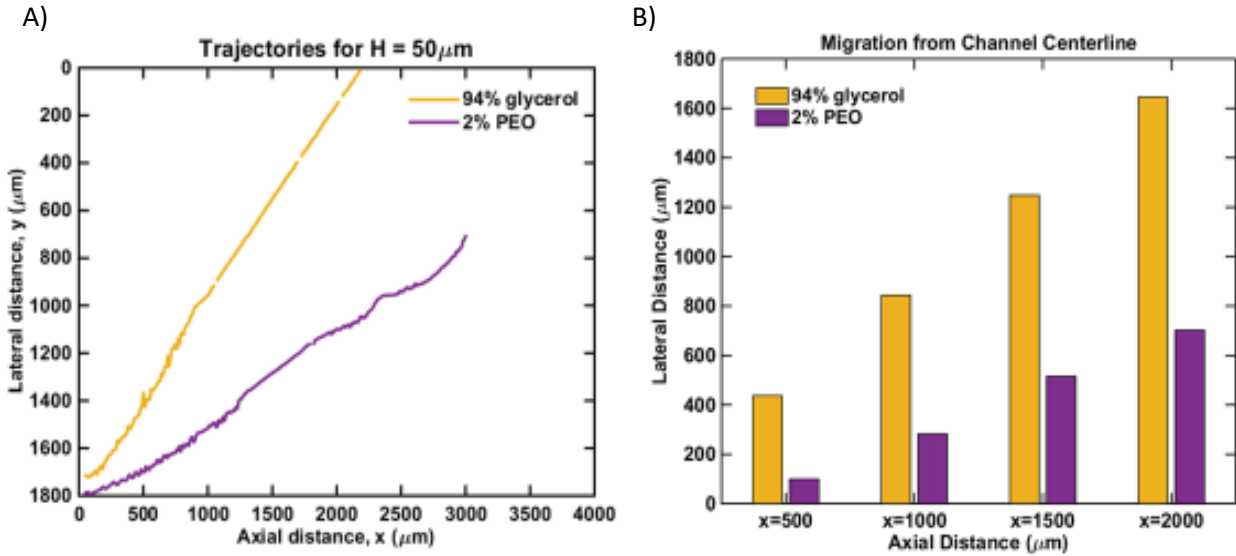


Fig. 52: A) trajectories for glycerol droplets vs. PEO in the expansion region, B) enhancement of lateral migration separation in the expansion region

This distinguishable trajectory resulted in the droplets to be collected in different outs of the device. We demonstrated a significant enhancement in droplet separation based on viscoelasticity. In order to find out the reason for the migration differences between viscous and viscoelastic droplets, we studied the shape change and the orientation of droplets in the initial migration stage.

We developed a semi-automatic algorithm to calculate the circularity of the droplets. Circularity was obtained based on the area (A) and the perimeter (P) of the deformed droplet:

$$f_{circ} = \frac{4\pi A}{p^2}$$

Circularity of PEO and glycerol droplets as a function of time are compared in Fig. 53. It's evident that the PEO droplets had a larger average velocity, as shown in Fig. 51A, since there are fewer data points for the same distance downstream of the channel. The first point in the graph corresponds to location in the channel where the pillar squeezes the droplets which resulted in the lowest circularity. The overall circularity of PEO droplets are lower than the glycerol droplets throughout, which implies that the PEO droplets were slightly more deformed. Glycerol droplets exhibited a uniform circularity throughout the channel, however, the circularity of the PEO droplets gradually increased. Circularity of a circle is 1 and any deviations from it indicates a deformation in droplet shape.

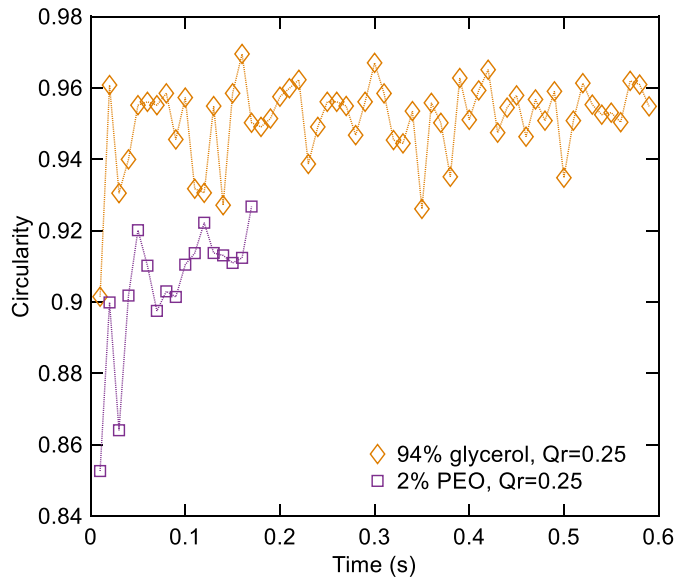


Fig. 53: circularity of PEO and glycerol droplets as a function of time



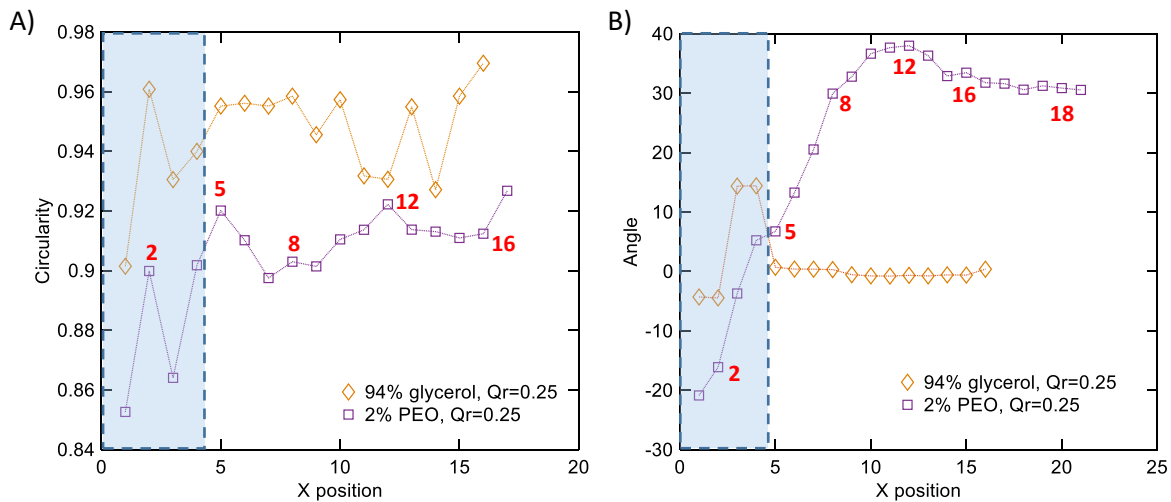


Fig. 54: circularity and orientation of PEO and glycerol droplets at the same position along the channel, A) circularity, B) orientation with respect to the flow direction – the numbers in red corresponding to the actual droplet shape in Fig. 55.

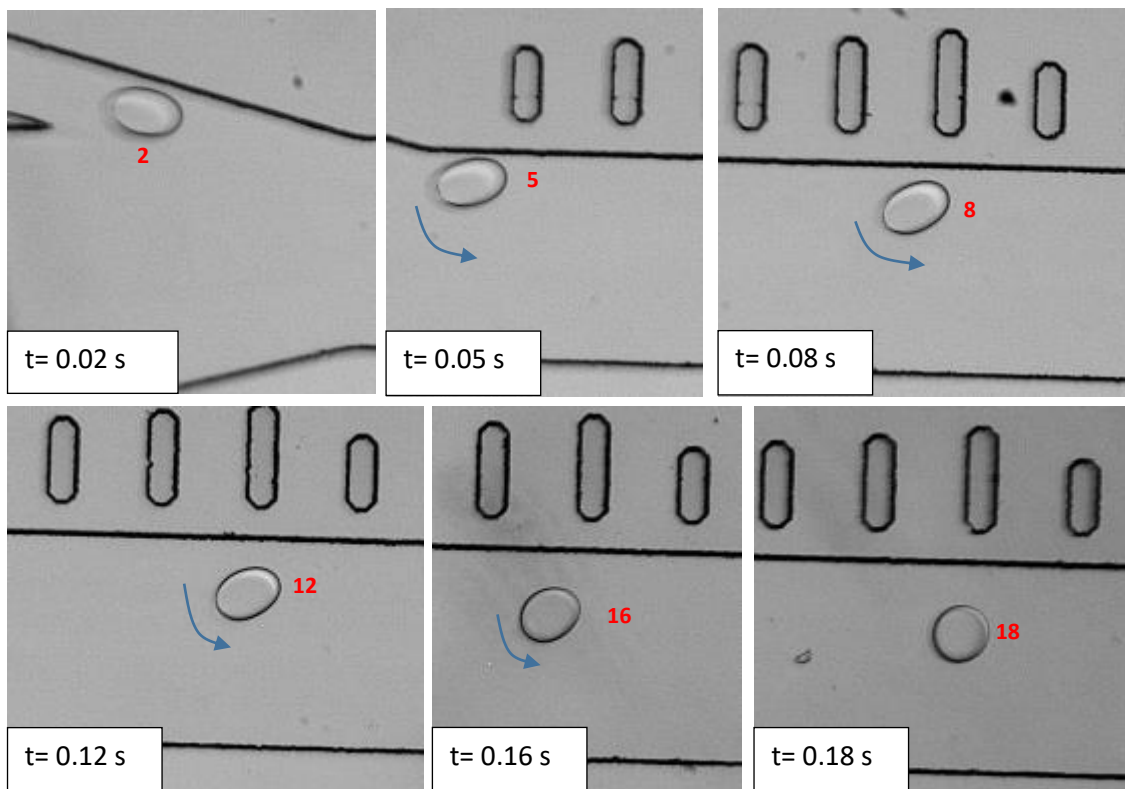


Fig. 55: time elapse of rotation of viscoelastic droplets in the main channel - the numbers in red corresponding to the calculated circularity and orientation of droplet shape in Fig. 54.

In this experiment, large axial velocity of the PEO droplets in the upstream channel, where the droplet deformation occurred, enabled viscoelastic droplets to deform. We believe

that this deformation was due to the combined effect of a large shear surrounding the fast-moving droplet and the local preservation of the droplet shape by pillars. The viscoelastic droplets maintained their deformed shape, and due to the very short time the droplets spent before they enter the main channel, the sheath flow was not able to have a significant impact on the droplet deformation. The average droplet circularity stayed relatively constant during this region (Fig. 54A). The viscoelastic droplets exhibited resistance to the large shear imposed by the sheath flow, hence, rather than deforming, they rotated in the main channel while kept their shape. Fig. 54B, illustrates a large change in droplet orientation while the circularity remained relatively constant. However, once the droplets are in the main channel, due to the large velocity gradient across the droplets, droplets would eventually recover to their undisturbed shape within their relaxation time (Fig. 55). A decrease in the angle of PEO droplets and an increase in the circularity are indications of droplet's recovery to their undisturbed shape which is associated with the relaxation time of the droplet Fig. 54, A, B).

The large scale microscopic motions are usually associated with the elastic character of the polymeric liquids. The relaxation time is the time associated with large scale motion (or changes) in the structure of the polymer, we denote this time scale by  $\lambda$  or the relaxation time. The microscopic timescale should be compared with the macroscopic flow time scales.

Even though we have not established a calibration curve to quantify the effect of channel confinement in the relaxation time of the viscoelastic droplet, from the Fig. 47 we would expect that the confined relaxation time ( $\lambda_{\text{conf}}$ ) was at least an order of magnitude larger than the measured relaxation time ( $\lambda$ ).

We defined two flow time scales, 1) the time it takes for the droplets to travel between the pillar and the main channel, we call this time scale of the sheath flow  $t_{\text{sh}}$ , and, 2) the time scale for the droplet to recover to its undeformed shape in the main channel, so called, recovery time,  $t_c$ . In this experiment, we calculated these timescales from high speed videos obtained at

100 fps and converted to unit of time (sec). Therefore, we evaluated  $t_{sh} = 0.04$  sec, and  $t_c = 0.18$  sec.

The droplet relaxation time is defined as the time it takes for the droplet to recover to its undeformed shape. Since, we obtained the time for the droplet recovery in the main channel in Fig. 55, we can estimate the relaxation time in our confined channel to be around,  $\lambda_{conf} = 0.18$  sec. With this relaxation time, we can adjust the De number by replacing  $\lambda$  with  $\lambda_{conf}$ . This is in agreement with our time-dependent droplet deformation study discussed in Fig. 47, where we proposed that the relaxation time in confined channel was an order of magnitude larger than the measured relaxation time for unconfined case. We should note that the estimated  $\lambda_{conf}$  is perhaps a function of droplet size, viscosity ratio, and viscoelastic properties, in addition to the degree of channel confinement. Deborah number can be described as a “time scale of the process ( $t_p$ )” or “fluid residence time” in a given regime within a complex flow field. We can report the ratio of the relaxation time to the time scale of the observation as Deborah number for the sheath flow and the main channel:

$$De_{sh} = \frac{0.18}{0.04} = 4.5$$

$$De_c = \frac{0.18}{0.18} = 1.0$$

According to Deborah number, the fluid resistance time for the droplet is large enough that the droplet’s deformation was not significantly affected by the sheath flow and the droplet maintain its shape and circularity once exposed to the sheath flow during  $t_{sh}$  (Fig. 54 A, B).

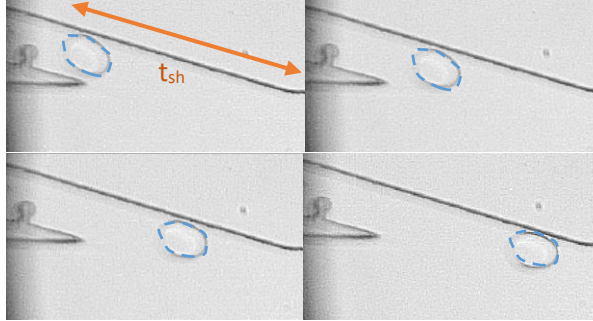


*Fig. 56: minimal sheath flow impact on deformation of PEO droplets due to a very short time scale of sheath flow*

To sum up this study, we explored the effect of a very short flow time scale relative to the relaxation time of the droplet. The deformed droplets did not have sufficient time ( $t_p < \lambda_{cont}$ ) to recover to their undeformed shape until after  $t_c = 0.18$  sec in the main channel. This was enough to promote a significant initial migration of viscoelastic droplets, mainly due to the ellipsoidal shape, their orientation, and the axial velocity.

This study suggested that by tuning the flow rate ratio of the device, we can change the time scale of the flow, and consequently control the shape and deformation of droplets. The flow rate ratio in this experiment was  $Q_r = 0.25$  which resulted in  $De_{sh} = 4.5$ . We demonstrated a sufficiently enhanced separation of viscoelastic droplets from viscous droplets as we were able to collect droplets in different channel outlets, outlet#1 for viscous and outlet#2 for viscoelastic droplets (Fig. 57).

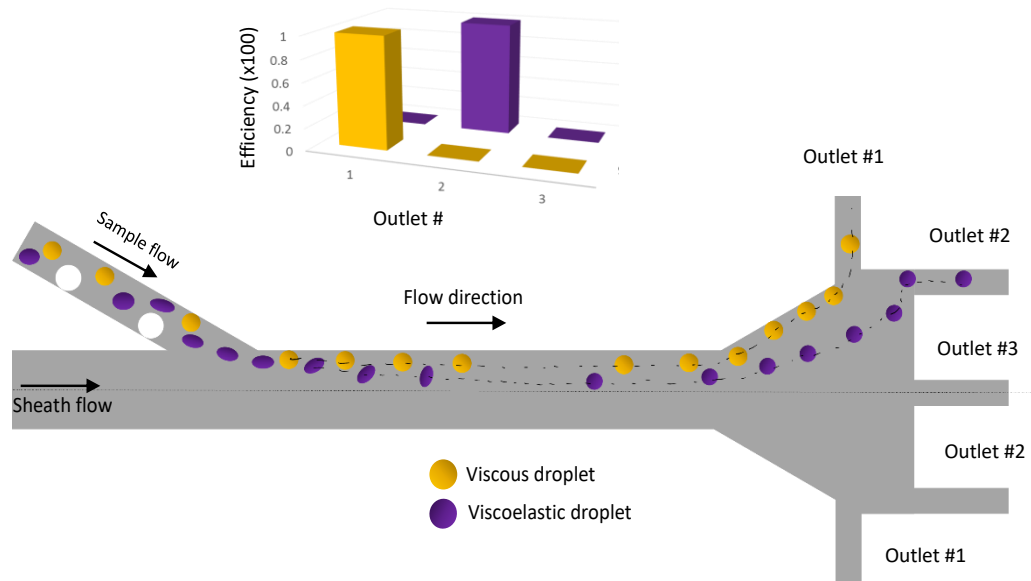


Fig. 57: high efficiency separation of viscoelastic droplets

## 4.2. Flow time scale – long

### 4.2.1. Study the effect of flow rate ratio

#### 4.2.1.1. Droplet shape

In this section, we explored the effect of different flow rate ratios  $Q_r$ , by adjusting the flow rate of the spacer flow ( $Q_s = 0.5$  and  $2 \mu\text{L}/\text{min}$ ) and the sheath flow ( $Q_{sh} = 35, 45, 55,$  and  $65 \mu\text{L}/\text{min}$ ). The flow rate ratio in this study was ranging from  $Q_r = 0.008 - 0.015$ , which was about two orders of magnitude smaller than the previous experiment. This allowed us to study the effect of flow rate ratio on the droplet deformation and migration mechanism when the flow time scale is relatively long. We examined the migration of PEO and glycerol droplets for a broad range of droplet sizes ( $D = 120 - 180 \mu\text{m}$ ).

When the flow rate ratio was relatively low, the effect of pillar and the sheath flow on the droplet deformation became more apparent. The flow time scale is chosen to be comparable to the relaxation time of the droplet, in contrast to the previous study where the flow time scale was a lot shorter. At first, droplets were deformed by the pillar, then the sheath flow introduced additional deformation to the droplets. Two steps deformation process with the associated circularities is shown in Fig. 58, for PEO droplets, as a function of droplet size for the flow rate ratio  $Q_r = 0.05$ , and  $Q_{sh} = 65 \mu\text{L}/\text{min}$ .

The data points with “filled” symbol in Fig. 58 representing the duration in which droplet was in contact with the pillar. The constriction by the pillar resulted in a reduction in droplet circularity, more than in the previous study. Sheath flow imposed another deformation to the droplets caused a change in droplet shape. Highlighted area in Fig. 58 demonstrated the change in circularity as the droplets undergoing deformation.

A larger deformation was obtained from the pillar, rather than the sheath flow, and the shape change increased with droplet size Fig. 58. Depending on the droplet size, we identified two types of droplets with an average diameter of  $d = 130 \mu\text{m}$ , according to their position upstream of the pillar. Either they were close to the wall, or slightly off the wall. The droplets that were located closer to the pillar were impacted slightly larger by the presence of the construction. However, due to the small size of these droplets, the impact of the pillar was minimal. The solid lines in Fig. 58, represents the data point for the circularity of droplets in the main channel. For the most part, droplets recover to their undeformed shape right before they enter the main channel. The reason for this behavior is related to the long-time scale of the deformation compare to the relaxation time, in which results in droplets behaving more as “fluid-like” rather than “solid-elastic-like”.

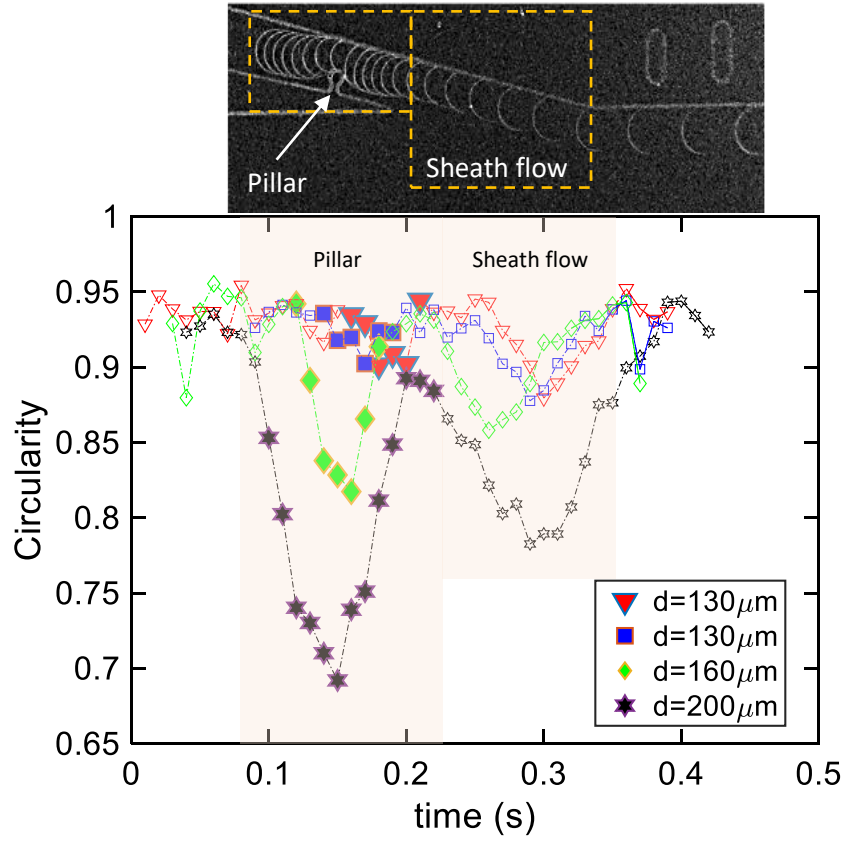


Fig. 58: size dependence circularity of PEO,  $Q_s = 0.5$ ,  $Q_{sh} = 65 \mu\text{L}/\text{min}$ , filled symbols represent where the droplet makes contact with the pillar, solid line represent where the droplet enters the main channel

The orientation of droplets relative to the flow direction is described in Fig. 59.

We used a semi-automated Python code to find the circularity and the orientation of the droplets in regard to the flow direction. We curve fitted the deformed shape of the droplet and found the angle of the major axis compare to the flow direction. Since the flow time scale is large relative to the relaxation time, droplets more or less behave like liquids. Droplet always orient themselves towards the flow direction (small angles fluctuating around zero degrees in Fig. 59), despite deformation by the pillar and the sheath flow. The sheath flow easily deformed the droplets and pushed them against the channel wall. Once they entered the main channel, they have already been recovered to their undisturbed shape. To confirm our hypothesis, we calculated the ratio of the relaxation time to the flow time scale, known as Deborah number.

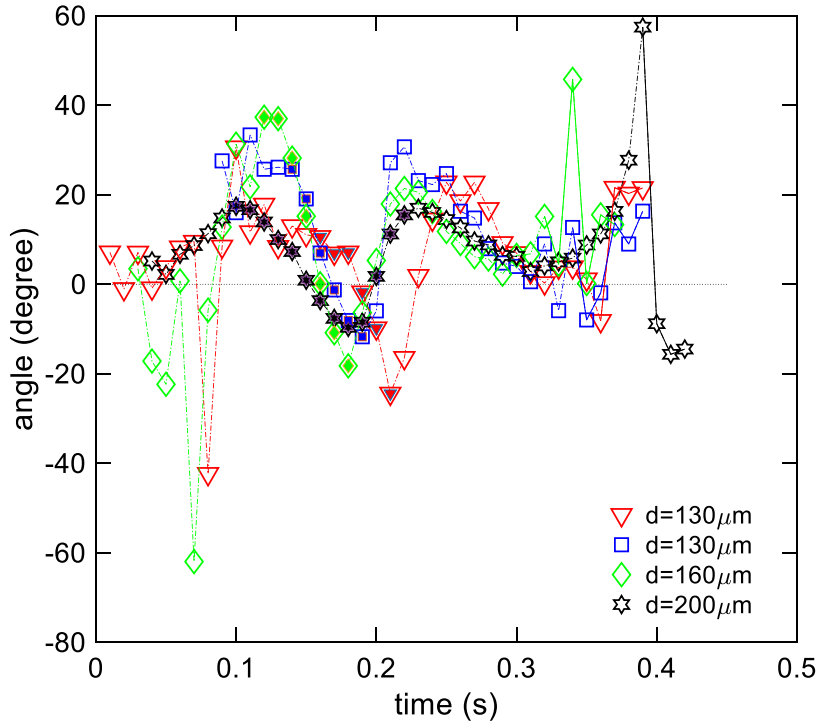


Fig. 59: change in droplet orientation due to the deformation from pillar and the sheath flow

Similar to the previous discussion regarding flow time scales, we calculated three different time scales, in which two were similar to the previous study, denoted as  $t_{sh}$  and  $t_c$ . An additional flow time scale can be defined as the time it takes for the droplet to pass the constriction pillar. We denote this as,  $t_{pp}$ . The calculated data shows that all the time scales were smaller than the relaxation time of the droplet. This could justify our hypothesis that the droplets were deformed by the pillar and the sheath flow, however, the time required for the stress to build up was not sufficient. Therefore, the material did not reach the relaxation time, and, as a result, the elastic characteristics of the viscoelastic material (the memory of the applied stress) was not fully satisfied. In other words, the droplets were deformed under an applied shear rate ( $\dot{\gamma}\lambda$ ), as it was shown in Fig. 58, however, the deformation lacked the elastic stresses associated with the second term in  $(\mu_0 + G\lambda) \dot{\gamma}$ .



The corresponding Deborah numbers for this sets of experiment are shown in Table 14. Relatively small Deborah number indicates a “fluid-like” behavior of the polymeric droplets, in contrast to  $De_{sh} = 4.5$ , when the flow time scale was sufficiently short.

Table 14: flow time scale and Deborah number for different viscoelastic droplets –  $Q_{sh} = 65 \mu\text{L}/\text{min}$

Time scale (s) / Deborah number	Dia = 160 $\mu\text{m}$	Dia = 130 $\mu\text{m}$	Dia = 130 $\mu\text{m}$	Dia = 200 $\mu\text{m}$
$T_{pp} / De$	0.07 / 0.17	0.06 / 0.2	0.06 / 0.2	0.13 / 0.092
$T_{sh} / De$	0.14 / 0.08	0.15 / 0.08	0.15 / 0.08	0.17 / 0.07
$T_c / De$	0.06 / 0.2	0.06 / 0.2	0.04 / 0.3	0.04 / 0.3

We compared the deformability of viscous (glycerol) and viscoelastic (PEO) droplets with increasing sheath flow, as shown in Fig. 60 . As expected the lowest sheath flow resulted in the smallest deformation of the droplets. Again, we saw that the droplets almost instantaneously recovered to their undeformed shape after the source of deformation (either pillar or the sheath flow) was removed, proving the fluid-like behavior of polymers in this case. An important observation was that the sheath flow did not deform the glycerol droplets except for the slight shape change at the largest sheath flow. Glycerol droplets were so stiff and resisted any deformation as it can be seen in Fig. 60.

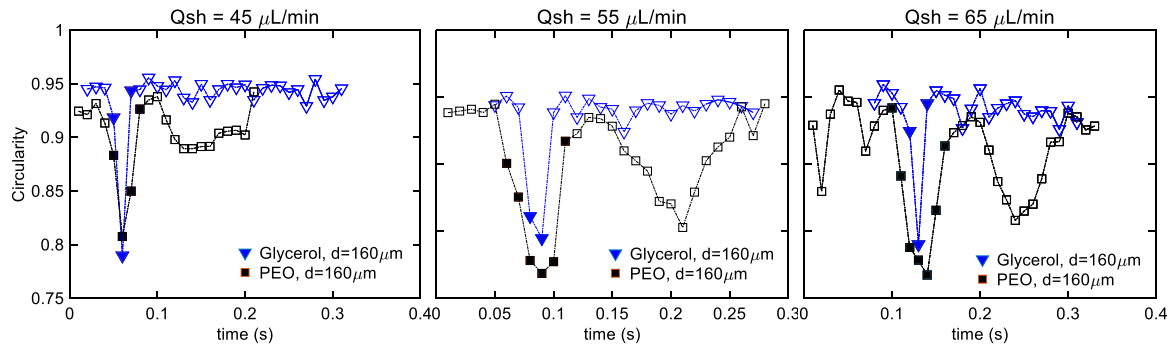


Fig. 60: circularity of PEO, with increasing sheath flow from  $Q_{sh} = 45 - 65 \mu\text{L}/\text{min}$ , filled symbols represent where the droplet makes contact with the pillar, solid lines represent where the droplet enters the main channel

#### 4.2.1.2. Droplet migration

Thus far, we have demonstrated that by tuning the flow rate ratio (the time scale of the flow), we were able to observe a completely different behavior of the polymer droplets. Now, the question is how this behavior will impact the droplet migration, for stiff glycerol droplets that resist deformation, and for the fluid-like polymer droplets of PEO. Next, we investigated the effect of flow rate ratio in migration of droplets.

The result presented in Fig. 61 A, B, and C, show the “position map” of viscous droplets in the confined channel for the case where the flow time scale is large. As it was demonstrated in Fig. 60, glycerol droplets are stiff and resist any deformation from the upstream pillar and the sheath flow, therefore, we would expect the similar behavior as the case where the flow time scale was low. By increasing the sheath flow, initial migration rate of droplets increases, resulting in a larger droplet distance from the wall. This was predicted as viscous droplets behave like solid and they experience a larger lift force with an increase in the channel Reynold number. Similar to the discussion we had for the previous case, the stiff droplets undergo an opposing lift forces from the wall and the velocity shear gradient, however, the viscous forces from the channel confinement restricts their migration towards the channel center. This is shown

as a peak (a maximum distance from the wall), where the initial migration region (highlighted in Fig. 61) ends. The viscous droplets tend to stay close to the proximity of wall throughout the length of the channel ( $\sim 120 \mu\text{m}$  away from the wall) after the initial adjustment to their position. Increasing the channel Reynolds number resulted in a slightly larger distance from channel wall. In contrast to viscous droplets, viscoelastic droplets migrate towards the channel center, in which similar to the viscous droplets, an increase in the channel Reynolds number, positioned them closer to the channel center ( $\sim 140 \mu\text{m}$  away from the wall).

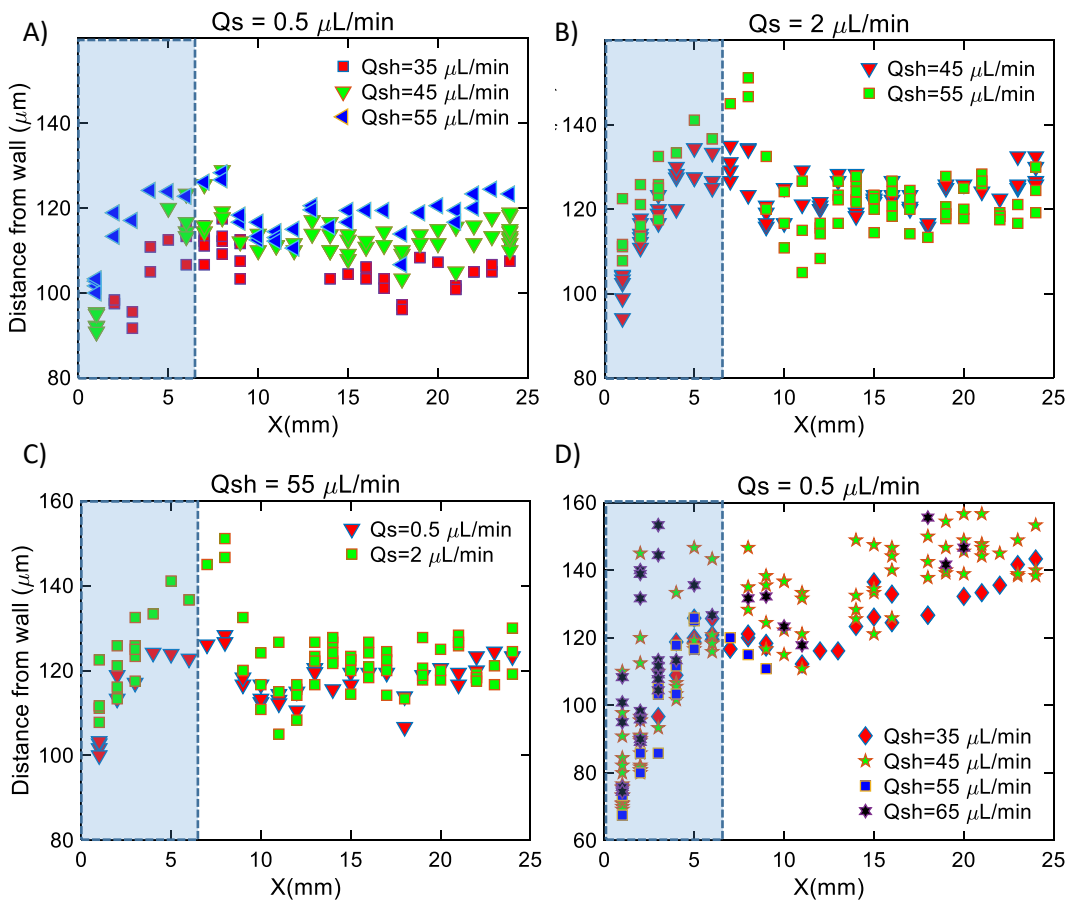
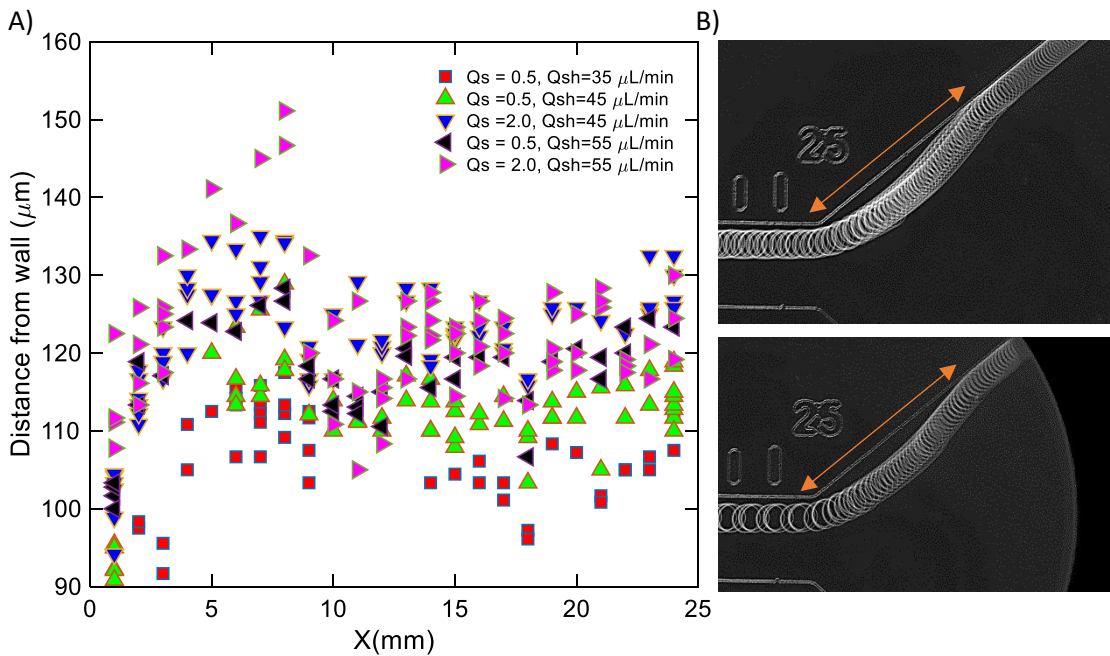


Fig. 61: flow rate dependent position-map of droplet sizes ranging from  $150\text{-}180 \mu\text{m}$ , A) increasing sheath flow ( $Q_s = 0.5 \mu\text{L}/\text{min}$ ), B) increasing sheath flow ( $Q_s = 2 \mu\text{L}/\text{min}$ ), C) increasing spacer flow ( $Q_{sh} = 55 \mu\text{L}/\text{min}$ ), D) PEO, increasing sheath flow ( $Q_s = 0.5 \mu\text{L}/\text{min}$ ) - highlighted area represents the initial migration region

Similarly, position map for viscoelastic droplet of PEO was obtained as a function of sheath flow for various droplet sizes. In this case, we can reasonably argue that an increase in

the sheath flow results in a decrease in the time scale of the flow. The results in Fig. 60, shows that as the sheath flow rate decreases, the deformation time of droplets by the pillar decreases as well; the number of “filled symbols” in Fig. 60, which represent the deformation time, would decrease with a decrease in sheath flow. This consequently, results in a shorter flow time scale. The similar argument is valid for the time scale of the sheath flow. However, a decrease in time scale of flow (decrease in deformation time) would not impact the migration mechanism, because the time is still large compare to the relaxation time.



*Fig. 62: trajectory of glycerol (viscous) droplets, A) flow rate dependent position-map, B) trajectory in the expansion region*

Position map for all the viscous droplets, regardless of flow rate ratio, are shown in Fig. 62 A. This includes wide range of droplets sizes and flow rates. Despite differences in the final equilibrium position, all viscous droplets ended up at the same position next to the wall in the expansion region (Fig. 62 B).

We observed a more spread out distribution of droplet positions, for the same size viscoelastic droplets, in the position map shown in Fig. 61D. We can attribute the wide

distribution range to the process in which the relaxation is occurring inside and outside of the chain. Polymer solutions can possess a spectrum of relaxation times, due to the interactions of polymer chains with the other chains. Therefore, the contribution to the relaxation process can come from different interactions. The effect might not be as strong for dilute polymers. If we can assume that all polymer chains relax uniformly and simultaneously, relaxation can occur with the longest time possible, because the relaxation of the entire chain is shorter than the longest relaxation time of the sub chains [6] [7]. Due to the wide range of possible relaxation times, each viscoelastic droplet might behave slightly different. This could explain the large standard deviation in Fig. 51 for the previous study, during the relaxation process of viscoelastic droplets. This phenomenon, however, did not affect the result of our experiment, because, viscoelastic droplets behaved completely different from the viscous droplets; slight variations within viscoelastic droplets did not impact the overall behavior.

We confirmed this by comparing the position map for viscous and viscoelastic droplets in Fig. 63. We identified two main regions in the position map: Initial migration and Final separation. In the “final separation” region, a clear distinction between viscous and viscoelastic droplets was observed. In the “initial migration” region, however, we observed a completely opposite behavior of migration of droplets compare to the result obtained for the previous study (large flow time scale). During the initial migration, viscous droplets demonstrated a larger initial migration rate, compare to viscoelastic droplets. We believe that this is because of the small Deborah number of the viscoelastic droplets, where droplets exhibit fluid-like behavior. In the initial migration stage, viscous droplets experience a larger lift force, due to their stiffness, compare to the deformable viscoelastic droplets. However, after the initial migration stage was over, the motion of the stiff droplets was limited due to channel confinement, in contrast to a wider range of lateral migration of deformable PEO droplets.

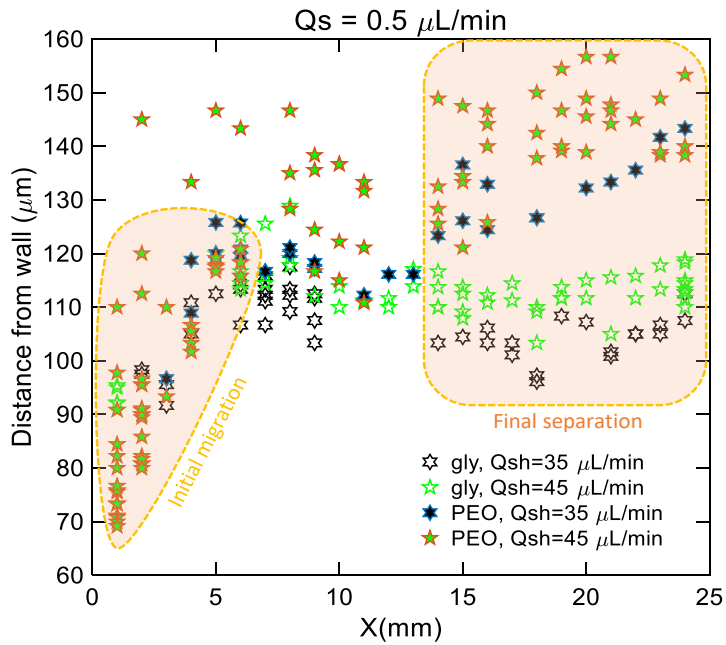


*Fig. 63: distinguishable separation between viscous and viscoelastic droplets in “final separation” region*

We demonstrated that the presence of pillar was required for enhanced initial migration of viscoelastic droplets. Fig. 64 shows the initial migration trajectory of the device without pillar is compared with when we have pillar. Since viscous droplets of glycerol were resistant to deformation, the presence of pillar to pre-deformed the did not seem to a significant impact on their migration.

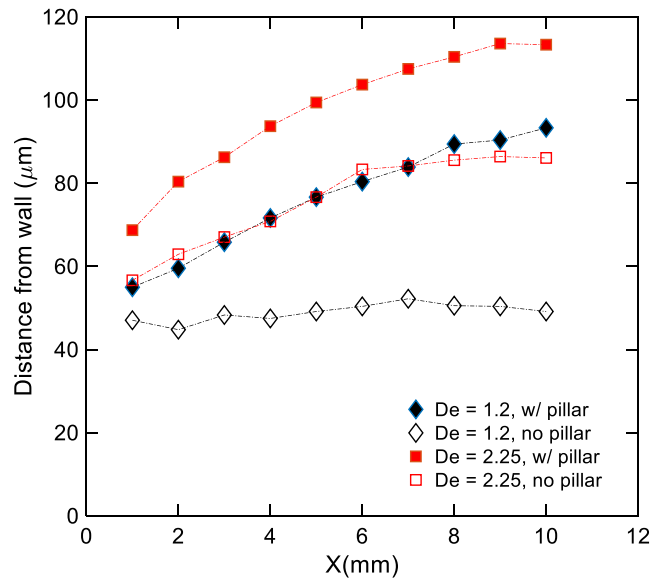


Fig. 64: Presence of pillar shows significant enhancement in initial droplet migration

## 5. Conclusions

We demonstrated the ability to change the shape of viscoelastic droplets, with the aid of fluid flow and a physical constriction upstream of the separation microchannel. By adjusting the flow rate ratio in our platform, we were able to explore the impact of different flow timescales compare to the relaxation time on migration. This would not be possible if the channel confinement was not present, because, the recovery time is retarded in confined geometries, allowing us to tune to a shorter flow timescale than the relaxation time.

When, the timescale is shorter than the relaxation time, a pre-deformed droplet sustains its shape within the relaxation time. This resulted in a significant initial migration of viscoelastic droplets (Fig. 65). However, when the timescale of flow is longer than relaxation time, viscoelastic droplets actively being deformed, as they possess fluid-like behavior. This results in a delay in initial migration of viscoelastic droplets, because of smaller initial lift force compare to viscous droplets. In both cases, viscous droplets exhibited similar behavior. Due to their

stiffness, they were not prone to deformation, and, because of channel confinement, their motion was limited to the proximity of wall. Despite the differences in the initial migration due to different flow timescales, we successfully demonstrated an ability to efficiently isolate viscoelastic droplets, in a high-throughput microchannel with a large degree of confinement.

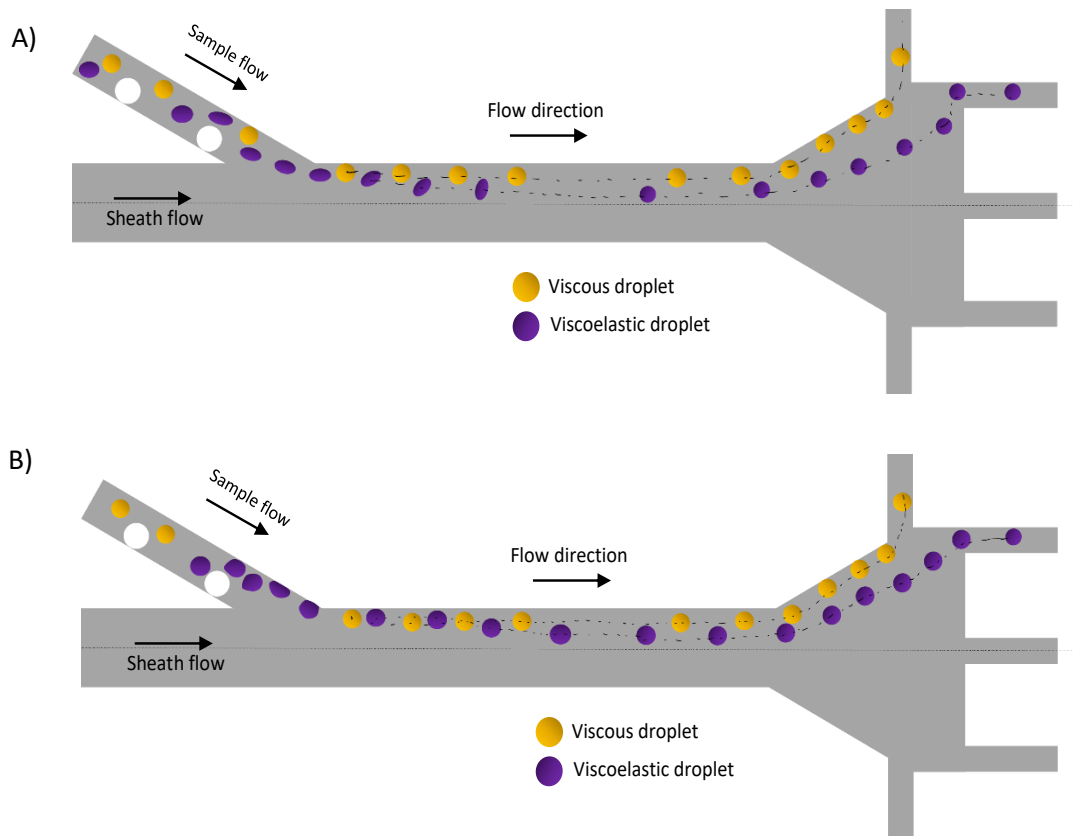


Fig. 65: schematic of droplet migration for different timescales relative to relaxation time, A) shorter flow time scale, B) longer flow time scale

## 6. Applications

We developed a microfluidics platform that can be used to isolate viscoelastic droplets. The special design of our platform allowed us to alter the properties of viscoelastic droplets, such that, when the flow timescale was smaller than the relaxation time, a pre-deformed droplet recovered to its undeformed shape within relaxation time. In this case, due to the deformed



shape of the droplet, a significantly large initial migration allowed for a distinct trajectory and consequently an efficient separation of viscoelastic droplets. When the flow timescale was large compare to the relaxation time, the deformability of viscoelastic droplets aided in the lateral motion of droplets, whereas, the motion of stiff viscous droplets was limited to wall proximity. Since the viscosity of droplets were chosen to be similar in this experiment, deformability of viscoelastic droplets resulted in their less restrictive motion. In the other words, the stiffness of viscous droplets prevented them from migration in the presence of confinement.

Deformability of viscous droplets increases with a decrease in viscosity (according to the definition of Ca number), and their motion may be less restricted. Therefore, next, we explored the role of viscosity of the droplets in migration. In this experiment, we used a larger sheath flow to be able to cause deformation on droplets. We demonstrated that droplets of low viscosity were also distinguishable from viscoelastic droplets. Despite the less significant migration rate at the beginning, at the separation region in the end of the channel and the expansion region, we observed distinguishable trajectories. The result is shown in Fig. 66.

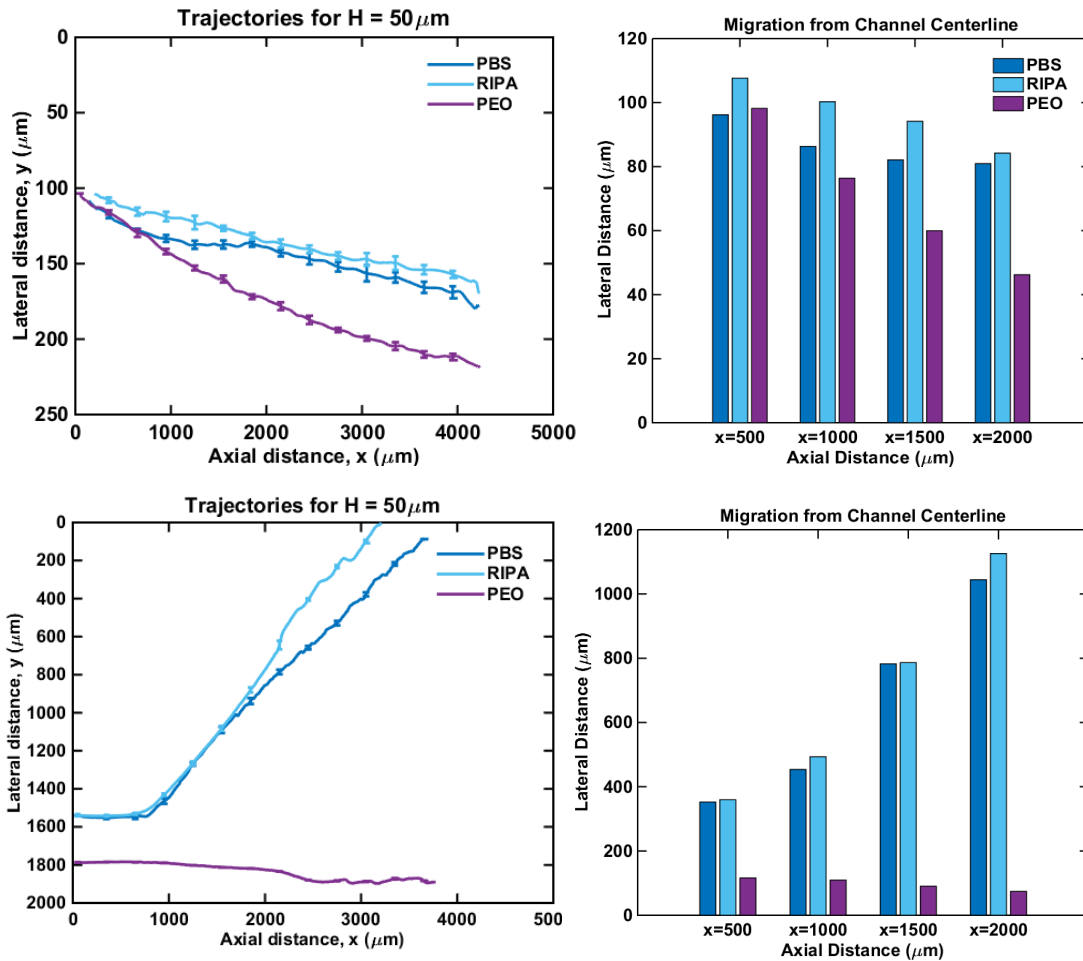


Fig. 66: Trajectories for lower limit droplet (PBS and RIPA) vs. PEO, A) main channel, B) expansion region

We observed that channel confinement resulted in suppression of the deformation of low viscosity/ low interfacial tension droplets (PBS and RIPA), once they were elongated by the presence of sheath flow. Fig. 67, compares the deformation of droplets by sheath flow for PBS and RIPA droplets in channels with height  $150 \mu\text{m}$  ( $\phi = 0.3$ ) and  $50 \mu\text{m}$  ( $\phi = 0.1$ ). Droplets retained their deformed shape for a longer period of time in the channel with higher aspect ratio.

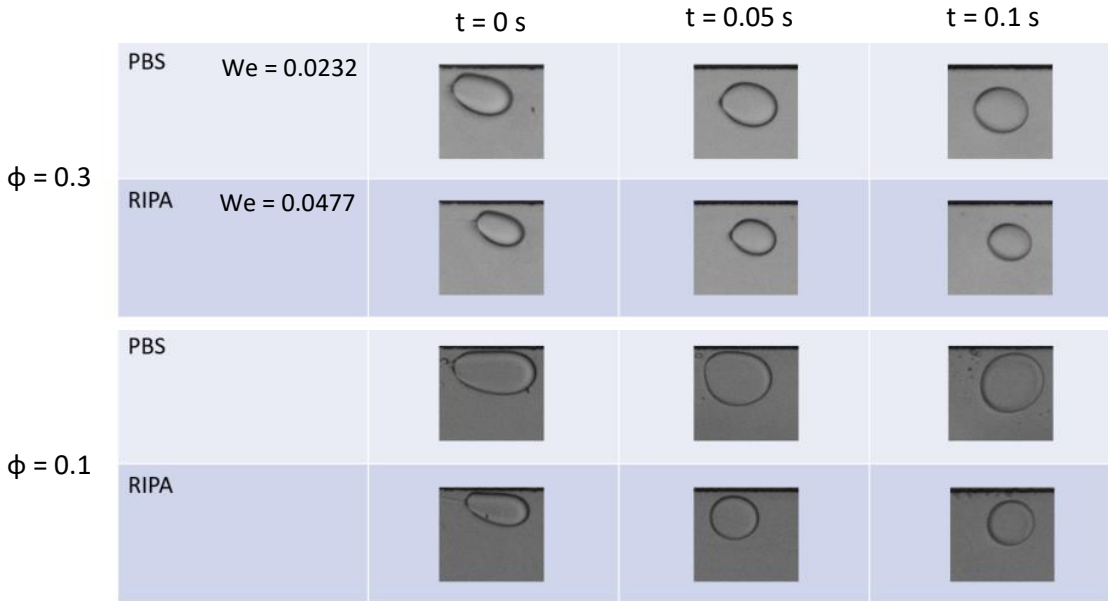


Fig. 67: Deformation of PBS and RIPA droplets

A common application that can benefit from our droplet separation platform is for the cell encapsulation applications.

In conclusion, we have demonstrated the ability to distinguish between “upper-limit” viscous solution (94% glycerol) and “lower-limit” solutions with a low interfacial tension solutions such as PBS (low viscosity) and RIPA Buffer (w/ 1% SDS. The properties of these extreme solution are listed in Table 13. The deformability of these droplets are characterized by Weber number.

Table 15: deformability characterization

	Solution (% Wt)	Density $\rho$ ( $\frac{g}{cm^3}$ ) @ 20°C	Interfacial Tension, $\sigma$ (mN/m)	Weber Number (We)
	Novec 7500	1.61		
	Water/ glycerol mixtures	$x_g = 93.9$	7.3	0.0033
	Water/ PEO	$x_g = 2$	6.53	0.0057
	PBS	$x_g = 100$	1.03	0.0232
	RIPA buffer	$x_g = 100$	< 0.5	0.0477

The lower limits are essential for applications such as encapsulation of single cells towards nucleic acid analysis. We demonstrated the ability to encapsulate single cells in droplets with RIPA lysis buffer (including 1% SDS). The droplets were lysed in droplets and Calcein AM was leaked out in the droplet which was an indication of a successful lysing, Fig. 68.

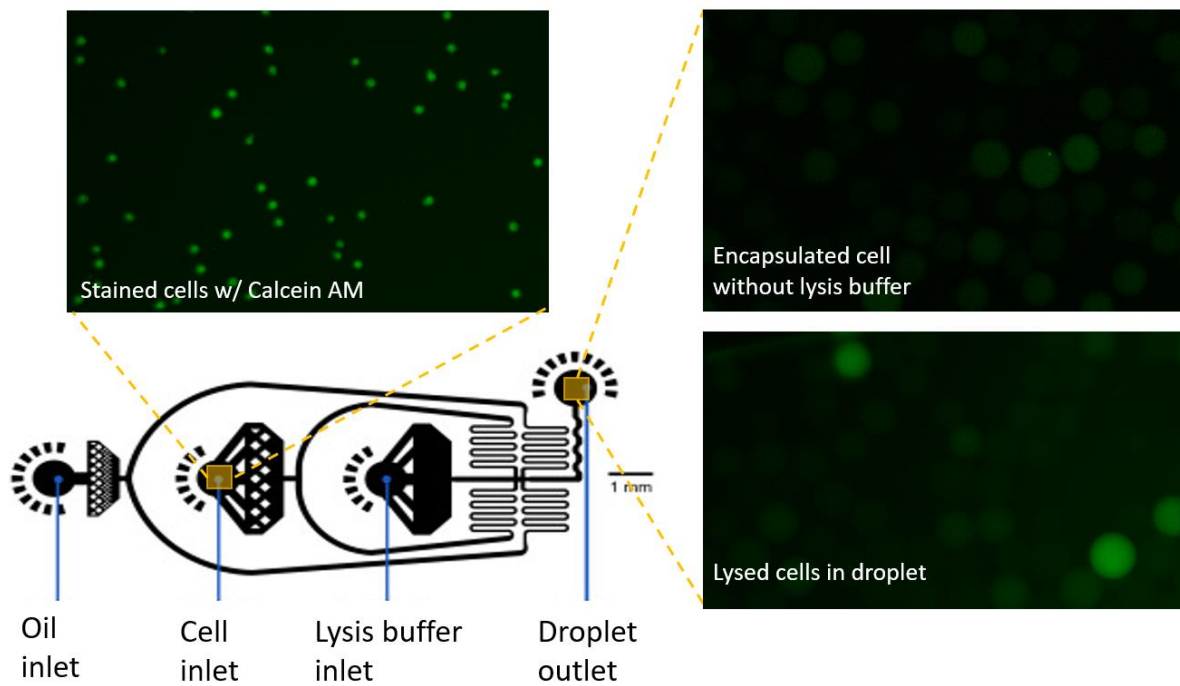


*Fig. 68: Single cell encapsulation and lysis in droplets*

The solutions of cell lysate exhibit non-Newtonian behavior as can be seen in Fig. 69.

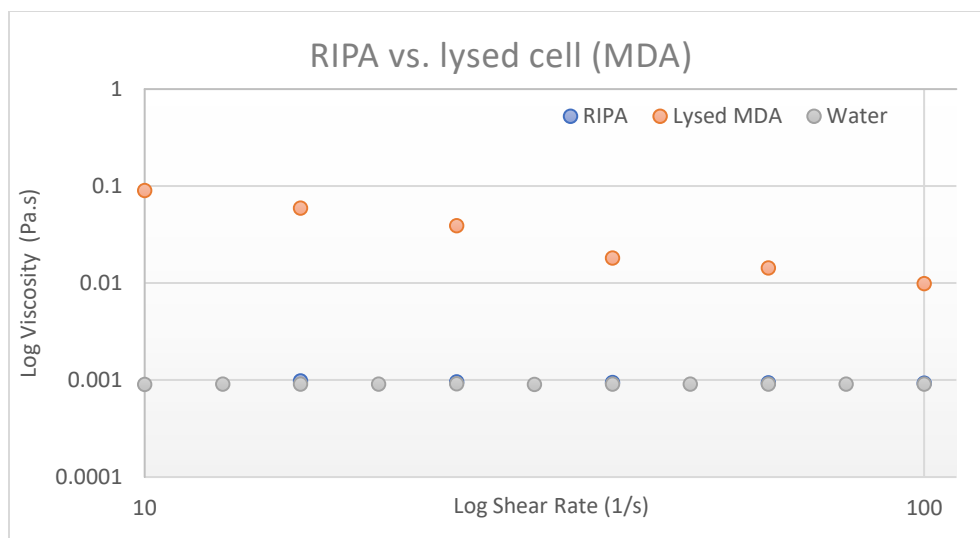


*Fig. 69: Shear thinning behavior of cell lysate solution*

Droplets of 2% PEO and 94% glycerol, exhibit much less deformability compare to RIPA and PBS solutions, having an order of magnitude smaller Weber number (Table 15).

Droplets of PBS and RIPA deformed a lot more that glycerol droplets under the same applied force from the sheath flow (Fig. 67), but they all recovered to their original shape rather quickly.

RIPA and PBS exhibit larger Weber numbers which resulted in large deformation, but the lift force was not enough to push them towards the center. Because of the channel confinement, their migration rate was too slow and they stayed closer to the wall.

In conclusion, we have developed a platform for separation of viscoelastic droplets from a wide range of viscous droplets. Distinct trajectories were obtained for various droplets of solutions of Newtonian and non-Newtonian. For many applications, it is necessary to be able to distinguish between viscoelastic droplets and viscous droplets of various viscosity ratio and the droplets of low interfacial tension. There are many applications that can benefit from a simple platform that can passively sort droplets. For example, cell lysate and the solution of amplified DNA exhibit a non-Newtonian behavior over a range of shear rates (Fig. 70 and Fig. 69), which

can be used to separate the droplets of without DNA (or non-amplified) and empty droplets, respectively. We also demonstrated the ability to distinguish between viscoelastic and low interfacial tension droplets.

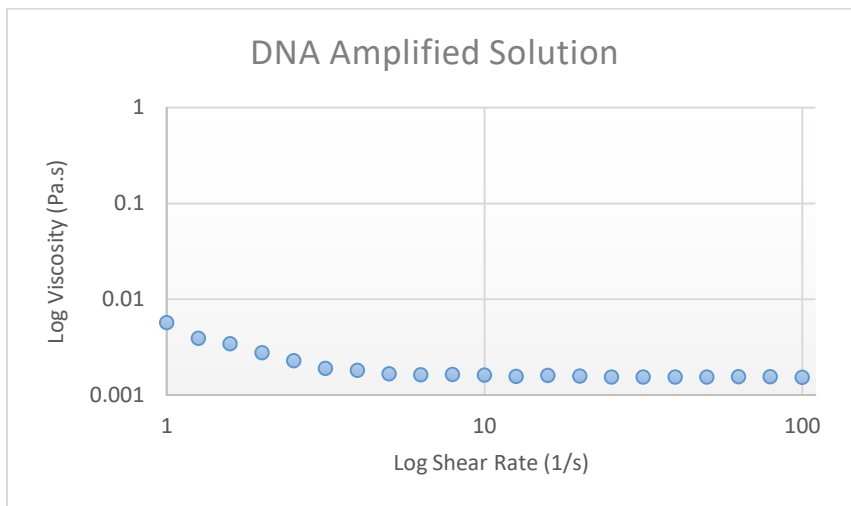


*Fig. 70: Shear thinning behavior of amplified DNA solution*

## 7. References

- [1] L. Zhu and F. Gallaire, "A pancake droplet translating in a Hele-Shaw cell: Lubrication film and flow field," *J. Fluid Mech.*, vol. 798, pp. 955–969, 2016.
- [2] Y. Ling, J. M. Fullana, S. Popinet, and C. Josserand, "Droplet migration in a Hele-Shaw cell: Effect of the lubrication film on the droplet dynamics," *Phys. Fluids*, vol. 28, no. 6, 2016.
- [3] E. J. Hinch, "Lecture 7 : Stress Relaxation," pp. 65–82.
- [4] H. Amini, W. Lee, and D. Di Carlo, "Inertial microfluidic physics," *Lab Chip*, vol. 14, no. 15, p. 2739, 2014.
- [5] Z. Nie et al., "Emulsification in a microfluidic flow-focusing device: Effect of the viscosities of the liquids," *Microfluid. Nanofluidics*, vol. 5, no. 5, pp. 585–594, 2008.
- [6] F. Del Giudice, S. J. Haward, and A. Q. Shen, "Relaxation time of dilute polymer solutions: A microfluidic approach," *J. Rheol. (N. Y. N. Y.)*, vol. 61, no. 2, pp. 327–337, 2017.
- [7] E. N. Lightfoot, W. S. W. Ho, K. K. Sirkar, and A. L. Zydney, "Membrane handbook," *AIChE J.*, vol. 41, no. 3, pp. 503–504, 1995.